Emergent Fields, Flat Bands and Phase Competition: A Study in Magnetic Pyrochlore Systems

by

Aritro Mukherjee

A thesis
presented to the University of Waterloo
in fulfillment of the
thesis requirement for the degree of
Master of Science
in Physics

Waterloo, Ontario, Canada, 2020

Author's Declaration

This thesis consists of material all of which I authored or co-authored: see Statement of Contributions included in the thesis. This is a true copy of the thesis, including any required final revisions, as accepted by my examiners.

I understand that my thesis may be made electronically available to the public.

Statement of contributions

Aritro Mukherjee was the sole author of Chapters 1, 2 and 5, which were written under the supervision of Dr. Michel Gingras and were not written for publication. The thesis consists of two projects (Chapters 3 and 4) written for publication.

Aritro Mukherjee is the sole author of Chapter 4 and all the research done therein. Chapter 4 was written under the supervision of Dr. Michel Gingras and the research was conducted at the University of Waterloo. The manuscript is currently being drafted by Aritro Mukherjee and Dr. Michel Gingras with expected contribution from Dr. Harald Jeschke at Okayama University for DFT calculations not discussed in this thesis.

Details of exceptions to sole authorship of material in Chapter 3 are as follows:

Research presented in Chapter 3

The first project on polarized neutron scattering was written under the supervision of Dr. Michel Gingras and the research was conducted at the University of Waterloo. The idea of the α-chains, was exposed by Jeremy Goh Swee Kang and Wen Jin. The NSF channel magnetic neutron scattering result (in the large-N approximation) of $\frac{4}{3\lambda}$ was independently obtained by the Aritro Mukherjee and Jeremy Goh Swee Kang. Expressions of magnetic neutron scattering in terms of emergent fluxes were first obtained by Kristian Chung and the Aritro Mukherjee reproduced these results for polarized neutron scattering. Connection between the flat bands and flat NSF was hypothesised independently by Jeremy and Aritro Mukherjee (via high temperature expansions of the spin-spin correlation functions, not shown in the thesis). The result provided in this thesis of why the NSF is flat and the line of reasoning with the special eigenvector and the flat eigenbands was first constructed by the Aritro Mukherjee and formalized with the help of Kristian Chung. Analysis on extended spin ice, deviations from flat NSF, the effect of further-neighbour interactions and the study of linecuts along the high symmetry directions were all carried out by the Aritro Mukherjee.

Kristian Chung drafted the manuscript and each author provided intellectual input on manuscript drafts.

Polarized neutron scattering experiments were undertaken and reported in a 2009 Science paper by Fennel *et.al.* (licensed content title: Magnetic Coulomb Phase in the Spin Ice $Ho_2Ti_2O_7$). Their results are displayed in this thesis after due permission from the licensed content publisher: "The American Association for the Advancement of Science" for licensed content publication in "Science" with License number: 4872570850019.

Abstract

We investigate spins models on the pyrochlore and the breathing pyrochlore lattice. Specifically, we study polarized neutron scattering in classical spin ice modelled via Ising spins with anti-ferromagnetic interactions. We find that the non-spin flip channel (NSF) of polarized neutron scattering is flat (**q**-independent) because the neutron polarization projects the flat eigenvalues of the adjacency matrix as the (magnetic) neutron scattering intensity in the $[hhl]$ plane, within the large-N approximation. The NSF intensity is shown to be inversely proportional to the stiffness of the emergent theory describing the system at low temperatures. We show that polarized neutron scattering probes the correlations of the emergent fluxes along and perpendicular to the neutron polarization direction. We further study the model in the presence of further-neighbour interactions and provide a prescription to obtain the Lagrange multiplier in the large-N approximation, when the NSF is not flat in such cases.

In further chapters, we investigate Heisenberg spins on a breathing pyrochlore lattice in the presence of second nearest-neighbour interaction J_2. We note the competition between J_2 and J_b (exchange interaction in the larger tetrahedron), which results in a variety of ordered phases. We obtain phase diagrams (at the mean field level) for the case of constant large ferromagnetic and anti-ferromagnetic J_a (exchange coupling in smaller tetrahedron) while J_b and J_2 are varied. We find a plethora of competing phases and explore the breathing regimes of the phase diagrams. Finally, we find a hitherto unreported phase with ordering wavevector $\frac{2\pi}{a}(qq0)$ and a state with sub-extensive line degeneracies along $\frac{2\pi}{a}(hhh)$ directions in the eigenspectra.

Acknowledgements

I humbly thank my Guru, whose contribution is ineffable. I thank all my teachers, nature and causation which has made this thesis possible. Primary has been the role of my respected supervisor, Michel Gingras. He has shown me how to be critical of myself and shown me a living example of passionate perfectionism. Now I know it can be done.

I thank James Martin, Anton Burkov, Dmitry Pushin, François David, Dan Wohns, Gang Xu, Chong Wang for offering excellent courses. I thank David Hawthorn for always providing cheerful advice regarding graduate formalities and discussions on Bragg scattering in X-rays. I also thank all the graduate administrative staff for always being supportive.

I thank Wen Jin, Kristian Chung, Darren Pereira, Naman Gupta, Daniel Lozano-Gómez, Gyan Gourab, James Chow, Bo Liu, Cyrus Cerkauskas, for 'useful' discussions on physics, biology, philosophy and other topics.

I also ardently thank my family who have been more than supportive in my unorthodox ventures.

Table of Contents

List of Tables x

List of Figures xi

List of Abbreviations xiii

1 Introduction 1

2 Methods 8

2.1 Neutron Scattering 8

2.2 Mean-Field Theory 20

2.3 Large-N 29

3 Polarized Neutron Scattering in Classical Spin Ice 38

3.1 Materials, motivation and models 38

3.2 Preliminary Results 44

3.2.1 Emergent Fields, Fluxes and Monopoles 44

3.2.2 Flat bands in the Eigen-spectrum 46

3.2.3 Geometrical Insight into Polarized Neutron Scattering 51

3.3 Key Results 59

3.3.1 Flat Bands to flat NSF . . . 59
3.3.2 Measuring the emergent field . . . 61
3.3.3 Extended spin ice and effect of further-neighbour interactions. . . . 63
3.3.4 Summary . . . 67

4 Heisenberg Spins on a Breathing Pyrochlore Lattice **74**
4.1 Introduction and Materials . . . 74
4.2 Model Hamiltonians . . . 78
4.2.1 Review of $\mathbf{J_a}$ - $\mathbf{J_b}$ Phase Diagram . . . 81
4.2.2 Why study the effect of further-neighbour interactions? . . . 90
4.3 Competition between J_2 and J_b . . . 92
4.3.1 Motivation . . . 92
4.3.2 Methods . . . 94
4.3.3 Implementation . . . 97
4.4 Mean Field Phase Diagram $\mathbf{J_b}$ vs $\mathbf{J_2}$ . . . 101
4.4.1 PD$_\mathbf{1}$: $\mathbf{J_a} = \mathbf{+1}$ (AFM) and $\mathbf{J_b}$ vs $\mathbf{J_2}$ . . . 104
4.4.2 PD$_\mathbf{2}$: $\mathbf{J_a} = \mathbf{-1}$ (FM) and $\mathbf{J_b}$ vs $\mathbf{J_2}$ . . . 111
4.4.3 (**hhh**) degenerate state . . . 116
4.4.4 Summary . . . 118

5 Discussions, Conclusions and Future Directions **126**

References **131**

APPENDICES **145**

A Lattices and Conventions **146**

A.1 Pyrochlore lattice 146

A.2 First Brillouin zone of the FCC lattice 148

A.3 Breathing Pyrochlore lattice 149

A.4 Further-Neighbour Interactions and Adjacency Matrices 152

B Minimization Implementation Discussions **155**

List of Tables

4.1 Breathing materials and nearest-neighbour coupling. 77
4.2 Parametric Equations for the (hhh) degenerate state. 117
4.3 Summary of the Phase Diagrams. 121

A.1 Summary of lattice conventions for the pyrochlore lattice. 148
A.2 Summary of lattice conventions for the breathing pyrochlore lattice. 150

List of Figures

1.1 Geometrically frustrated spins on the triangular and pyrochlore lattice . . 3

1.2 Typical susceptibility inverse (χ^{-1}) vs temperature (T). 6

2.1 Elastic and inelastic neutron scattering. 10

2.2 Neutron scattering geometry. 13

2.3 Polarized neutron scattering. 18

2.4 Spin-spin correlations of Heisenberg spins on a pyrochlore lattice. 28

2.5 λ vs T for AFM Ising pyrochlore. 37

3.1 Two tetrahedra in the pyrochlore lattice and ice-rules. 40

3.2 Polarized neutron scattering in $Ho_2Ti_2O_7$. 42

3.3 Eigenbands of the nearest neighour Ising model on a pyrochlore lattice. . . 49

3.4 Geometry of polarized neutron scattering. 54

3.5 Geometry of the α-chains. 58

3.6 Further-neighbour couplings in the pyrochlore lattice 63

3.7 Polarized neutron scattering of spin ice. 70

3.8 Polarized neutron scattering of extended spin ice. 71

3.9 Polarized neutron scattering near the spin slush regime. 72

3.10 Polarized neutron scattering of Ising spins on a pyrochlore lattice with further-neighbour interactions. 73

4.1 Breathing pyrochlore lattice. . . . 75
4.2 Phase diagram for J_a and J_b. . . . 80
4.3 Coulomb phase eigenvalues and the flat bands. . . . 82
4.4 Spin susceptibilities $S(\mathbf{Q})$ in the Coulomb phase. . . . 82
4.5 Eigenvalues of the ferromagnetic phase. . . . 85
4.6 Spin susceptibilities in the ferromagnetic phase. . . . 85
4.7 Effective moments in AFM-FCC. . . . 86
4.8 Eigenvalues for the effective AFM-FCC phase. . . . 87
4.9 Spin susceptibilities of the effective AFM-FCC phase. . . . 87
4.10 Breathing pyrochlore with further-neighbour interactions. . . . 89
4.11 Breathing pyrochlore with J_a, J_b and J_2. . . . 92
4.12 Phase diagram 1. . . . 103
4.13 Eigenvalues in the presence of additional AFM J_2. . . . 104
4.14 Eigenvalues in the presence of additional FM J_2. . . . 106
4.15 Eigenvalues showing transitions between various phases. . . . 108
4.16 Phase diagram 2. . . . 110
4.17 Phases stablized with large FM J_a while J_2 and J_b compete. . . . 112
4.18 (hhh) degenerate state. . . . 119
4.19 Structure factors for $\mathbf{k} = 0$ and PS phase. . . . 122
4.20 Structure factors for $(\frac{1}{2}\frac{1}{2}\frac{1}{2})$ and Kawamura phase. . . . 123
4.21 Structure factors showing DT and unreported $(qq0)$ phase. . . . 124
4.22 Structure factors showing MMS and (hhh) degenerate state. . . . 125

A.1 Section of the pyrochlore lattice showing sublattice conventions and the α-chains. . . . 147
A.2 FBZ of the FCC lattice. . . . 149
A.3 Rotation of the breathing pyrochlore lattice. . . . 151
A.4 Kagomé layers perpendicular to the $\langle 111 \rangle$ direction in the pyrochlore lattice. 151

List of abbreviations

AFM - Anti-ferromagnetic

FM - Ferromagnetic

FBZ/BZ - First Brillouin Zone/Brillouin Zone

FCC - Face Centred Cubic Lattice

PNS - Polarized Neutron Scattering

SF - Spin Flip Channel

NSF - Non-Spin Flip Channel

SI - Spin Ice

ESI - Extended Spin Ice

MFT/MF - Mean Field Theory

CP - Coulomb Phase

PFFRG - Pseudo-Fermion Functional Renormalization Group

AFM-FCC - Effective Anti-ferromagnetic FCC phase

PS - Planar Spiral Phase

DT - Double Twist Phase

MMS - Multiply Modulated Spiral Phase

Chapter 1

Introduction

The usual historical stance of physics and natural sciences in general has been to isolate each part of a particular system, then keenly investigate it and extend the understanding to explain the properties of the whole. The underlying assumption being, the whole is a sum of its parts [1]. This line of inquiry has led humanity to ever more subtler dissection of nature and its constituents, in the search for an elusive fundamental pattern. In this fashion, one reduces matter to molecules to atoms to nuclei and electrons to leptons, quarks and bosons. What lies beyond is not yet known.

In this thesis, we will follow a holistic attitude as exemplified by P.W. Anderson's statement of 'More is Different' [1] . The key understanding (in contrast to the reductionist attitude) being that collective behaviour of the underlying constituents results in novel phenomena unseen amongst the isolated parts. We will dwell on a particular length/energy scale of our choice and try to understand the collective behaviour and not just the individual

behaviour, of a particular many body system. We aim to be close to experiment and material realization while trying to utilize intuitive mathematical models. These models must be complex enough to capture the qualitative physics of our chosen system, easy enough to solve in real time using contemporary computers and must be directly linkable to experimental results. In this way, we hope to discover novel ways in which matter organizes itself, as well as promote materials where such novel physics might be probed.

The fundamental question one may ask is: Given the information about various constituents of a system, how do the 'emergent' properties of the system arise out of interacting internal degrees of freedom? As a case study, we choose the problem of interacting spins on a lattice to model magnetic phenomena in matter. The energy scale chosen is in the meV range, characterized by the energy of the neutrons and energy scale of typical magnetic phenomena being probed in this thesis (see Sec. 2.1). A simple yet effective mathematical model to study such a system of interacting degrees of freedom is the Heisenberg/Ising family of spin models given by:

$$\mathcal{H} = \sum_{<i,j>} J_{ij} \mathbf{S}_i \cdot \mathbf{S}_j. \tag{1.1}$$

Here, $\mathbf{S}_i$ is a classical Heisenberg or an Ising (no vector product for this case and denoted by σ in later chapters) spin at site i and the sum is over connected neighbours (i and j) in $\langle i, j \rangle$. J_{ij} is the adjacency matrix (see Appendix A.4) containing the information of which spins are interacting. We shall use variants of this model in this thesis to study magnetic systems and how the spins behave at different temperatures. Frustration is a key concept, which is the ambiguity of a clear choice of how a spin should orient in the presence of

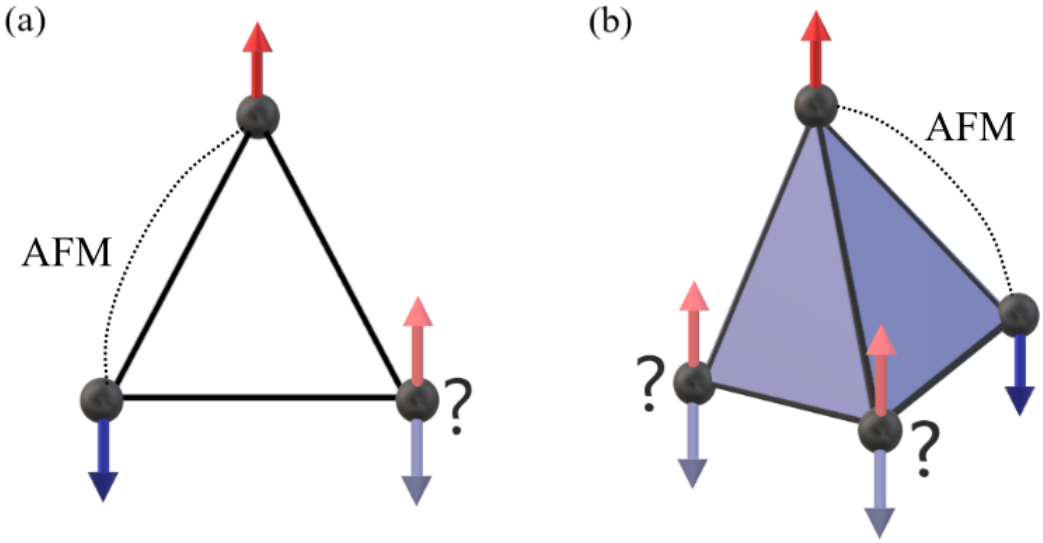

Figure 1.1: Figures illustrate frustrated spins with anti-ferromagnetic (AFM) nearest-neighbour coupling, on (a) triangular and (b) tetrahedral units. The energy is minimized when neighbouring spins anti-align. The '?' show the sites on which spins cannot minimize the energy by orienting either way and are 'frustrated.'

competing interactions, which are trying to align it in different directions. At low enough temperatures of the order of the exchange energy J, typical unfrustrated systems order in a certain way and are described by local order parameters. This ordering is found by minimizing the Helmholtz free energy. However, interestingly, in frustrated systems the spins order at a temperature much lower than the characteristic energy scale given by the exchange interaction [2, 3]. Key examples of geometric frustration are compounds with magnetic moments interacting anti-ferromagnetically and residing on lattices with triangular motifs (such as the triangular lattice, the kagomé lattice, the pyrochlore lattice, etc. See Fig. 1.1). Since all interactions cannot be satisfied simultaneously due to geometry and the strength of the interactions, interesting magnetic states with suppressed long range order but finite short range spin-correlations may arise [3, 4].

This raises the interesting question of whether spins can remain fluctuating down to $T = 0$ and never order (in a 'spin liquid' state) for frustrated systems. This is still an ongoing avenue of research and there are various proposals and much debate [4, 5, 6, 7, 8]. In the paramagnetic phase, the spins are uncorrelated whilst fluctuating randomly. Any material will be paramagnetic at high temperatures. At low temperatures, the 'spin liquid' is fluctuating and disordered in some sense, but also highly correlated. This state, where the spins are fluctuating (like a paramagnet) but also correlated has been called a 'cooperative paramagnet' [6, 9, 10]. Essentially, both the terms: 'cooperative paramagnet' and 'classical spin liquid' indicate the same phenomena of fluctuating but correlated spins when temperature T is in the range, $T_c < T < J$. Here, J (exchange coupling) is the overall energy scale of the problem and T_c is the temperature of the transition at low temperatures.

At this point, the observable, linear susceptibility χ plays an enlightening role. It is a measure of how the magnetization m (total sum of spins $\sum_i S_i^z$) of a material responds to an (small) external field intensity h^z i.e. $\chi = (\frac{\partial m}{\partial h})_T$ (T held constant). χ is tensorial for general systems but is a scalar for isotropic systems (such as the Heisenberg model). At high temperature, one can show that χ is related to the correlation between magnetizations which on evaluation yield a spin-spin correlation function [11, 12]. Up to a multiplicative constant, χ takes the form:

$$\chi(T) \propto \frac{1}{T} \sum_{i,j} \langle S_i^z S_j^z \rangle. \tag{1.2}$$

Correlation functions are important observable quantities and we shall be discussing them in detail, especially for the case of neutron scattering in later chapters (see Chap. 2). At

high temperatures, χ follows the Curie-Weiss law given by:

$$\chi(T) \propto \frac{1}{T - \Theta_{\mathrm{CW}}}. \tag{1.3}$$

Here, Θ_{CW} is the Curie-Weiss temperature and at high temperatures is given by the sum of the exchange interactions, with all neighbours of a given site i.e. $\Theta_{\mathrm{CW}} \propto \sum_i J_{ij}$ where J_{ij} is the interaction between site i and j. Θ_{CW} thus provides a way to approximately infer the strength and signs of the couplings. In general, negative Θ_{CW} indicates anti-ferromagnetism and positive Θ_{CW} indicates ferromagnetic couplings. The presence of further-neighbour interactions may complicate this naive analysis. The transition temperature T_c (called T_N for anti-ferromagnetic couplings) is found when χ develops a divergence (for FM) or a sharp peak (for AFM) at a certain temperature. In unfrustrated systems, this transition temperature, $T_c \approx |\Theta_{\mathrm{CW}}|$ while for frustrated systems, $T_N \ll \Theta_{\mathrm{CW}}$ (see Fig. 1.2). The frustrated system at temperature T, for $T_N < T \ll |\Theta_{\mathrm{CW}}|$ is thus fluctuating and shows no ordering (no sharp peak but a broad peak in χ vs T [2]) and is in the 'cooperative paramagnetic' regime. As shown in Fig. 1.2, χ^{-1} is follows the Curie-Weiss Law (above T_c) and its x-intercept is used to determine Θ_{CW}. Summarizing, while an unfrustrated system orders at T_c (or T_N) $\approx \Theta_{\mathrm{CW}}$, a frustrated system (typically) orders at a much lower temperature $T_N \ll |\Theta_{\mathrm{CW}}|$. In two dimensions, the anti-ferromagnetic nearest neighbour Ising model on a triangular lattice is a well known example of geometrical frustration. In three dimensions, the pyrochlore lattice (see Appendix A), which is composed of tetrahedral motifs serves as a canonical example of geometrical frustration (see Fig. 1.1). For discussions on spin liquids in the context of frustrated magnets, see Refs. [3, 4, 5, 7, 8, 13, 14, 15, 16]. In this

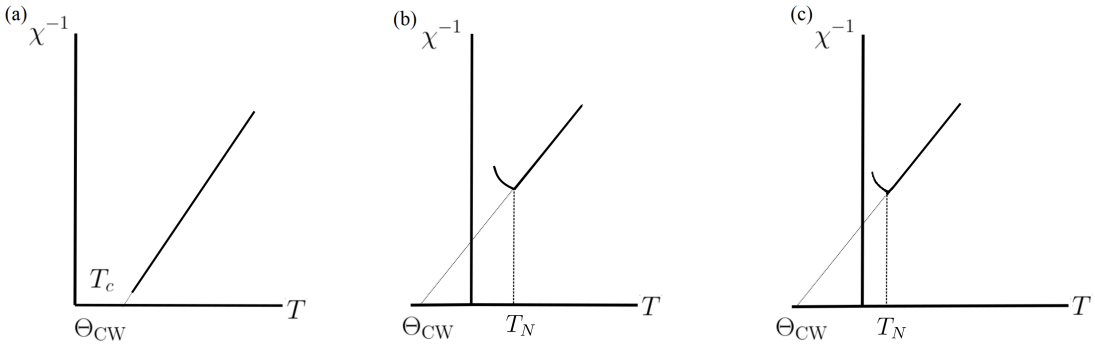

Figure 1.2: Figures show typical susceptibility inverse (χ^{-1}) vs temperature (T) plots. (a) and (b) illustrate the case for unfrustrated systems and (c) illustrates the case of anti-ferromagnetic frustrated system. (a) is ferromagnetic and $\Theta_{\rm CW} \approx T_c$, where T_c is the transition (critical) temperature and $\Theta_{\rm CW}$ is the Curie-Weiss temperature. (b) illustrates the scenario for unfrustrated anti-ferromagnetic systems where $\Theta_{\rm CW} \approx T_N$, where T_N is the Néel temperature. The $\Theta_{\rm CW}$ for ferromagnetic (positive) and anti-ferromagnetic (negative) case differ by a sign (further-neighbour interactions of different signs will change this naive view). (c) illustrates the case for frustrated systems, where $\Theta_{\rm CW} \gg T_N$. The frustrated system thus, orders only at temperatures T_N much lower than $\Theta_{\rm CW}$.

thesis, we study the case of anti-ferromagnetic Ising pseudospins on a pyrochlore lattice, wherein, at low temperatures, a Coulomb phase is stablized [17, 18, 19, 20]. In Chap. 2, we review neutron scattering and obtain expressions for the spin-spin correlation functions using mean field theory and the large-N approximation. In Chap. 3, we investigate polarized neutron scattering in spin ice [20]. We find that polarized neutron scattering may be useful in directly measuring the stiffness of the emergent coarse-grained fields (collection of spins treated as an emergent field of fluxes and charges). In Chap. 4, we study the case of Heisenberg spins on a breathing pyrochlore lattice [21, 22, 23] (see Appendix A.3) and obtain phase diagrams in the presence of further-neighbour coupling J_2 (see Appendix A.4). We find a variety of ordered phases one of which was hitherto unreported. Another

of these phases is composed of AFM interacting emergent magnetic moments[1]. Finally, in Chap. 5, we conclude and list further avenues one may wish to explore.

[1]This is the effective AFM-FCC phase described in Chap. 4. This phase occurs for Heisenberg spins on a breathing pyrochlore. The emergent magnetic moments are clusters of spins on a tetrahedron which interact ferromagnetically and align to form effective moments. The effective moments in turn reside on a FCC lattice and interact with each other via AFM coupling, hence the name.

Chapter 2

Methods

In this chapter, we derive and present some of the equations utilized in the following chapters. This includes a brief introduction to magnetic neutron scattering, where the primary quantity of interest is the spin-spin correlation function. Then, we describe how this quantity may be obtained from mean-field theory and large-N analysis. In this thesis, there is no distinction between contravariant (r^i) and covariant (r_i) indices and indices may be subscript or superscript when convenient.

2.1 Neutron Scattering

We begin with neutron scattering, an important experimental technique to probe the structure and dynamics of condensed matter systems [24]. The discovery of the neutron by Chadwick in 1932 ushered in the nuclear age for humanity and led to ever more increasing knowledge of the nuclear length scale as well as deeper fundamental connections between

various subfields of physics [25]. We shall introduce the key equations here and refer the interested reader to the Refs. [12, 24, 26, 27, 28, 29, 30] for more detailed discussions. Further information about neutron sources: reactor and spallation sources, may be found in Ref. [31].

Basics of Neutron Scattering

The neutron is a neutral particle with a magnetic moment and mass of 1.67×10^{-27}kg. It interacts with the nuclei (via strong interaction[1]), the nuclear magnetic moments and with the unpaired electrons in the sample, producing only a small disturbance in the system [24]. The contributions are called nuclear and magnetic contributions to the neutron scattering intensity, respectively [28, 29]. Moreover, the interaction of the neutrons with light atoms (e.g. Hydrogen, Oxygen, Carbon) allows clearer distinction of isotopes as compared to X-rays [24]. The de Broglie wavelength of the neutron is given by $\frac{h}{mv}$ where h is the Planck constant, m is the mass and v is the velocity of the impinging neutron. In an experiment, the thermal distribution of velocities of the neutrons in a neutron beam follow the Maxwell-Boltzmann distribution [28]. The corresponding de Broglie wavelength for slow thermal neutrons is in the angstrom length scale with energies ranging from 0.1 meV to 100 meV matching closely with the energy scale of elementary excitations in condensed matter, further details of which may be found in Refs. [24, 28]. Our aim in the neutron scattering problem, is to determine the probability of a neutron with initial wavevector (momentum if $\hbar \equiv 1$) $\mathbf{k}$, impinging on a sample and exiting with final wavevector $\mathbf{k}'$. The

[1]This is modelled via a Fermi pseudo-potential not discussed in this thesis.

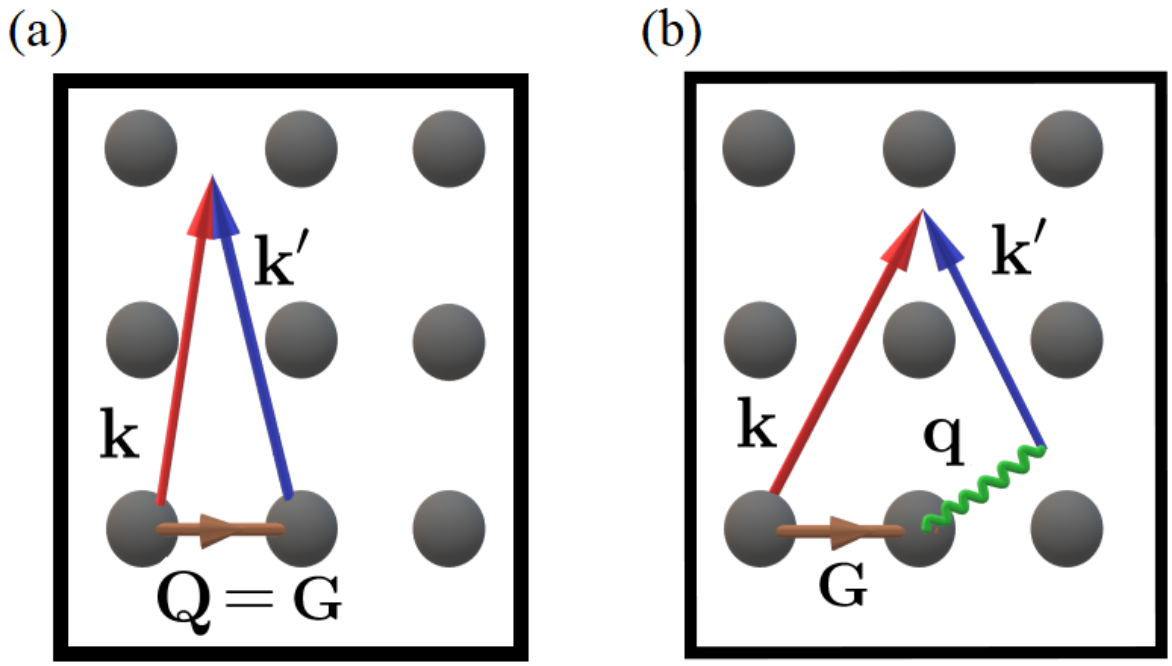

Figure 2.1: Figues shows momentum transfer $\mathbf{Q}$ in a neutron scattering event off a crystal in reciprocal space. The spheres here are reciprocal lattice sites. $\mathbf{k}$ is the initial and $\mathbf{k}'$ is the final momenta of the neutron ($\hbar = 1$). Panel (a) shows the case of elastic neutron scattering where $\mathbf{Q}$ is an exact reciprocal vector $\mathbf{G}$. Since after the scattering event $\mathbf{Q}$ is known, one may obtain structural information (magnetic and nuclear) of the sample using elastic neutron scattering. Panel (b) shows the case when the momentum transfer $\mathbf{Q}$ is not equal to a reciprocal vector $\mathbf{G}$, in which case $\mathbf{Q}$ can be decomposed into $\mathbf{G}$ and an excitation with wavevector $\mathbf{q}$ i.e. $\mathbf{Q} = \mathbf{q} + \mathbf{G}$. Inelastic neutron scattering, is thus a great tool to probe elementary excitations of comparable energy scales (to the neutron) such as spin waves [24], crystal field transition frequencies [16] and phonons [29].

momentum transfer and energy transfer are given by:

$$\mathbf{Q} \equiv \mathbf{k} - \mathbf{k}' = \mathbf{G} + \mathbf{q}, \tag{2.1}$$

$$\hbar\omega = \frac{\hbar^2}{2m}(k^2 - k'^2). \tag{2.2}$$

Here, $\mathbf{G}$ is a reciprocal lattice site vector, $\mathbf{q}$ is the wavevector of an elementary excitation in the sample (see Fig. 2.1) and ω is the frequency of the excitation. If $\mathbf{q} \neq 0$, we have inelastic neutron scattering with non-zero energy transfer [24]. However, if $\mathbf{q} = 0$ and $\mathbf{Q}$ is an exact reciprocal lattice vector, we obtain elastic scattering which is of interest to us in this thesis.

Key quantities of interest are cross-sections [24, 27, 29, 32] (see Fig. 2.2) which include the double differential cross-section given by:

$$\frac{d^2\sigma}{d\Omega dE} = \frac{C}{\eta\phi N}\frac{1}{\Delta\Omega\Delta E}. \tag{2.3}$$

Here σ is the cross-section, Ω the solid angle, dE the differential energy of the neutron, ϕ is the neutron flux (per unit area and time), η provides a measure of efficiency of the detector, N denotes the number of identical neutrons in the beam. C is the neutron count per unit time obtained in infinitesimal energy ΔE and solid angle $\Delta\Omega$. If the experiment does not analyze the energies of the neutron and just counts neutrons scattered in solid angle $\Delta\Omega$, we find the energy integrated differential cross-section given by:

$$\frac{d\sigma}{d\Omega} = \frac{C}{\eta\phi N}\frac{1}{\Delta\Omega}. \tag{2.4}$$

Similarly, integrating out the solid angle, we obtain the total cross section, counting all exiting neutrons in all directions, giving:

$$\sigma_{\text{Total}} = \frac{C}{\eta\phi N}. \tag{2.5}$$

The cross sections above are related via:

$$\frac{d\sigma}{d\Omega} = \int_0^\infty dE(\frac{d^2\sigma}{d\Omega dE}), \tag{2.6}$$

$$\sigma_{\text{Total}} = \int d\Omega \frac{d\sigma}{d\Omega}, \tag{2.7}$$

where the second integral is taken along all directions.

Consider a neutron scattering event with initial and final neutron momenta $\mathbf{k}$, $\mathbf{k}'$. The initial and final spin state of the neutron is σ and σ'. Let the initial state of the sample be $|\lambda\rangle$ and the final state be $|\lambda'\rangle$ (see Fig. 2.2). Using the Born Approximation (refraction, extinction and multiple scattering events of the neutron beam are ignored) and Fermi's Golden Rule [12, 26, 27, 28, 29, 32], one obtains the double differential cross-section given by:

$$\frac{d^2\sigma}{d\Omega dE} = (\frac{m}{2\pi\hbar^2})^2 \frac{k'}{k} \sum_{\lambda,\lambda',\sigma,\sigma'} p_\lambda p_\sigma |\langle \mathbf{k}', \sigma', \lambda' | \tilde{\mathcal{U}} | \mathbf{k}, \sigma, \lambda \rangle|^2 \times \delta(\hbar\omega + E_\lambda - E_{\lambda'}). \tag{2.8}$$

Here p_λ represents the thermal probability of the states of the initial scatterer $|\lambda\rangle$. p_σ is the polarization probability of the neutron with initial state $|\sigma\rangle$. k, k' are the magnitudes of the initial and final neutron momenta and the delta function enforces energy conservation

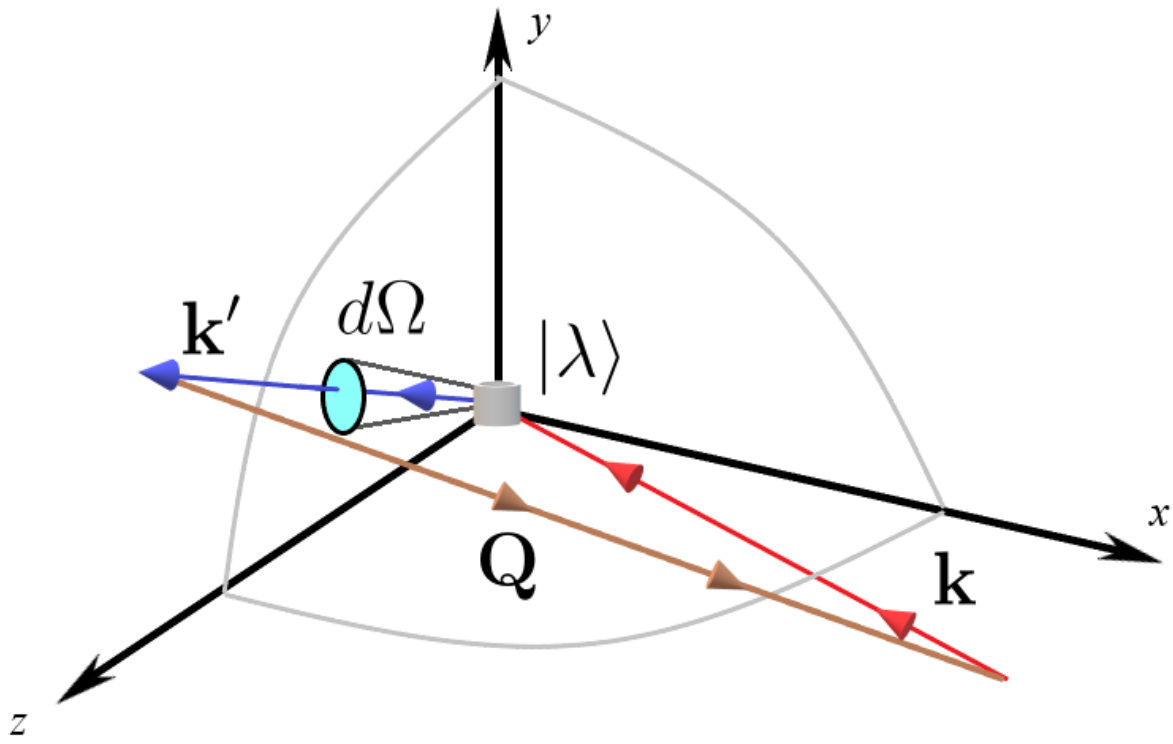

Figure 2.2: In this illustration, we show an impinging neutron with momentum $\mathbf{k}$ ($\hbar = 1$), interacting with the sample in an initial state $|\lambda\rangle$. After the scattering event, the neutron exits with momentum $\mathbf{k}'$ through an infinitesimal solid angle $d\Omega$. The resulting difference in momentum transfer, $\mathbf{Q}$, lies in the plane of scattering and is given by $\mathbf{Q} = \mathbf{k} - \mathbf{k}'$.

between initial and final states. $\tilde{\mathcal{U}}$ is the interaction operator of the neutron with the sample and has both nuclear and magnetic terms [24, 29]. Modelling the nuclear contribution by a Fermi pseudo-potential (assuming nuclei at fixed positions) and the initial and final state of the neutron as plane waves, yields a double differential cross-section proportional to the scattering length and a (time dependent) two-point correlator between Fourier transformed locations of the nuclei in the sample [24, 29]. The cross-section further has two contributions namely an incoherent nuclear contribution coming from correlation between the same nucleus at different times leading to no interference effects, while the coherent nuclear contribution comes from both correlations between the same nuclei at different times as well as different nuclei at different times, which leads to interference effects [29]. The interested reader may refer to Refs. [24, 26, 27, 28, 29, 30] for further details.

Magnetic Neutron Scattering

We are interested in magnetic neutron scattering, where the neutron interaction operator $\tilde{\mathcal{U}}$ is composed of the neutron magnetic moment operator $\tilde{\mu}$ and the local magnetic field of the sample $\mathbf{H}$. The neutron moment operator, $\tilde{\mu} = \gamma \mu_{\mathrm{N}} \tilde{\sigma}$, where $\gamma = -1.91$, is the gyromagnetic ratio, $\mu_{\mathrm{N}} = 5.05 \times 10^{-27}$ J/T (here J and T are Joule and Tesla, respectively) is the nuclear magneton and $\tilde{\sigma}$ is the Pauli spin operator for the neutron (no factor of 1/2 in the definition). The interaction operator is given by [24, 28, 29]:

$$\tilde{\mathcal{U}} = -\tilde{\mu} \cdot \mathbf{H}, \tag{2.9}$$

where $\mathbf{H}$, the local in-sample magnetic field has two contributions coming from the spin of the electron and the magnetic field generated by the orbital motion of the electron [28]:

$$\mathbf{H} = \nabla \times (\frac{\tilde{\mu}_e \times \mathbf{R}}{|\mathbf{R}|^3}) - \frac{e}{c}(\frac{\mathbf{v}_e \times \mathbf{R}}{|\mathbf{R}|^3}). \tag{2.10}$$

Here, e is the electron charge, c is the velocity of light, $\mathbf{v}_e$ is the orbital velocity of the electron and $\mathbf{R}$ is the location of the point where the magnetic field $\mathbf{H}$ is computed. $\tilde{\mu}_e$ in the above equation is the magnetic dipole moment operator of the electron and is given by:

$$\tilde{\mu}_e = -g_e \mu_{\mathrm{B}} \tilde{\mathbf{S}}, \tag{2.11}$$

where $\tilde{\mathbf{S}}$ is the spin operator of the electron (includes a factor of 1/2 in comparison with Pauli spin operator for the neutron) and μ_{B} is the Bohr magneton. g_e is the dimensionless electron spin g-factor given approximately by 2.0023. Substituting Eq. (2.10) in Eq. (2.8), we obtain the working formula for magnetic neutron scattering [24]:

$$\frac{d^2\sigma}{d\Omega dE} = \mathcal{G}(\mathbf{Q}) \sum_{\alpha,\beta} (\delta_{\alpha\beta} - \frac{Q_\alpha Q_\beta}{|\mathbf{Q}|^2}) S^{\alpha\beta}(\mathbf{Q}, \omega), \tag{2.12}$$

where the function $\mathcal{G}(\mathbf{Q})$ is given by:

$$\mathcal{G}(\mathbf{Q}) = (\gamma r_0)^2 \mathcal{F}^2(\mathbf{Q}) e^{-2W(\mathbf{Q})}, \tag{2.13}$$

and $S^{\alpha\beta}(\mathbf{Q},\omega)$, which is the essential quantity of interest, is given by:

$$S^{\alpha\beta}(\mathbf{Q},\omega) = \sum_{j,j'} e^{i\mathbf{Q}\cdot(\mathbf{R}_j - \mathbf{R}_{j'})} \sum_{\lambda,\lambda'} p_\lambda \langle\lambda|S_j^\alpha|\lambda'\rangle\langle\lambda'|S_{j'}^\beta|\lambda\rangle \times \delta(\hbar\omega + E_\lambda - E_{\lambda'}). \tag{2.14}$$

In the above equations, the function $\mathcal{G}(\mathbf{Q})$ is composed of the square of the classical electron radius, $r_0^2 \approx 10^{-24}$ cm^2 which sets the overall magnitude of the magnetic contribution and is of the same order as that of nuclear cross-section [24, 29]. $\mathcal{F}(\mathbf{Q})$ is the dimensionless magnetic form factor given by the Fourier transform of the unpaired electron cloud density around an ion. It increases with decreasing magnitude of $\mathbf{Q}$ [24]. $e^{-2W(\mathbf{Q})}$ is the Debye-Waller factor[2] which accounts for the dynamical and static displacements of the nuclei in the sample [30, 33, 34]. The sum in Eq. (2.12) is over spin components i.e. $\alpha, \beta \in [x, y, z]$. The neutron polarization factor $(\delta_{\alpha\beta} - \frac{Q_\alpha Q_\beta}{|\mathbf{Q}|^2})$, ensures that the neutron only interacts with magnetic moments in the plane perpendicular to momentum transfer $\mathbf{Q}$. The magnetic scattering function $S^{\alpha\beta}(\mathbf{Q},\omega)$ in Eq. (2.14), is composed of a Fourier transform of the locations of the moments $\mathbf{R}_i$ and $\mathbf{R}_j$, thermal averages of the spin components S_i^α and an energy conserving delta function. The algebraic procedure to derive Eq. (2.12) is quite involved and we refer the reader to the Refs. [24, 29] for explicit details.

Using the integral representation of the δ function and integrating out ω we obtain the expression of elastic total magnetic neutron scattering used in this thesis [12, 24, 26, 29]:

$$\frac{d\sigma(\mathbf{Q})}{d\Omega} = C \sum_{j,j'} \langle \mathbf{S}_{j\perp} \cdot \mathbf{S}_{j'\perp} \rangle e^{i\mathbf{Q}\cdot(\mathbf{R}_j - \mathbf{R}_{j'})}, \tag{2.15}$$

[2]It follows from the Fourier transform of the two point correlators of the displacements of the same nuclei at infinitely long times. It accounts for the lessening of intensity (attenuation) of the neutron beam due to atomic lattice vibrations in the sample.

where $\mathcal{F}(\mathbf{Q})$ and other constants (μ_B, γ, etc) have been absorbed in the constant, C. Here, the correlator is between projections of spins perpendicular to neutron momentum transfer $\mathbf{Q}$ and given by:

$$\langle \mathbf{S}_{j\perp} \cdot \mathbf{S}_{j'\perp} \rangle = \sum_{\alpha,\beta} (\delta_{\alpha\beta} - \frac{Q_\alpha Q_\beta}{|\mathbf{Q}|^2}) \langle S_j^\alpha S_{j'}^\beta \rangle. \tag{2.16}$$

Thus, we see that magnetic neutron scattering probes the spin-spin correlations in the plane perpendicular to $\mathbf{Q}$. To obtain expressions for the correlation functions $\langle S_j^\alpha S_{j'}^\beta \rangle$, we utilize mean-field theory and large-N analysis detailed in later sections.

Polarized Neutron Scattering

In the previous sections, the initial and final spin state of the neutrons $|\sigma\rangle$ were summed over for the case of unpolarized neutrons. Polarizing the neutron spins along a particular axis (say $\hat{\mathbf{z}}$), one can further resolve the magnetic neutron scattering contributions into the spin flip channel (SF) and the non-spin flip channel (NSF). This allows much more experimental leeway and has been used for distinguishing between incoherent and paramagnetic scattering, less ambigious determination of magnetic structures and differentiating excitations such as phonons and magnons [24, 28, 29].

We motivate just the basic idea that the neutron spin is **flipped** if it interacts with magnetic moments **perpendicular** to the neutron polarization ($\hat{\mathbf{z}}$ here) and the spin is **not flipped** if the magnetic moment in the sample is **parallel** to $\hat{\mathbf{z}}$ (see Fig. 2.3). Consider the Pauli spin operators in the magnetic moment operator of the neutron, $\tilde{\mu} = -\gamma\mu_{\mathrm{N}}\tilde{\sigma}$. Its eigenstates corresponding to $\tilde{\sigma}_z$ is the up and down state: $|+\rangle$ and $|-\rangle$. Because of the orthogonality of neutron spin states and its momentum states, the matrix element in

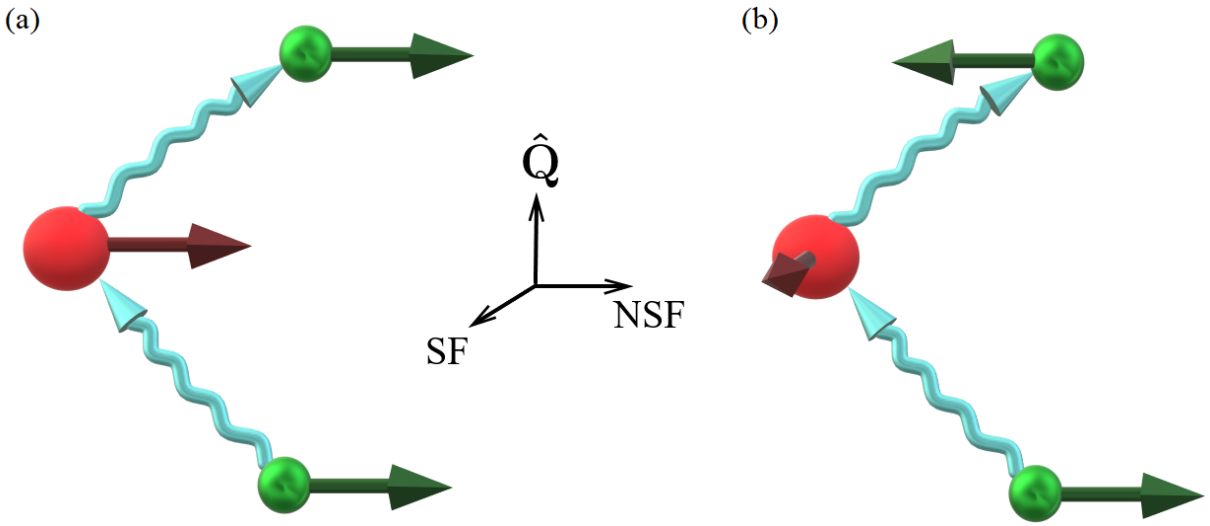

Figure 2.3: Figure shows an impinging neutron (green spheres) with polarization shown via green arrows (initially along NSF). The local magnetic moment (red spheres) direction is illustrated via a brown arrow. In (a), the initial neutron (sphere below) polarization is parallel to the local magnetic moment being probed (both along NSF), the neutron spin remains unchanged after scattering. In (b), the magnetic moment (now along SF) is perpendicular to the neutron polarization (along NSF), the outgoing neutron will undergo a spin-flip process. Inset shows the NSF (along neutron polarization), SF directions and the momentum transfer along $\hat{\mathbf{Q}}$. Thus, all contribution to magnetic neutron scattering perpendicular to $\hat{\mathbf{Q}}$ may be further resolved along two orthogonal axes corresponding to the NSF (along neutron polarization) and the SF channel.

Eq. (2.8) may be written as [24]:

$$\langle \mathbf{k}', \sigma', \lambda' | \tilde{\mathcal{U}} | \mathbf{k}', \sigma, \lambda \rangle = \langle \mathbf{k}', \lambda' | \tilde{\mathcal{U}} | \mathbf{k}', \lambda \rangle \langle \sigma' | \tilde{\mathcal{U}} | \sigma \rangle. \tag{2.17}$$

Considering the second term $\langle \sigma' | \tilde{\mathcal{U}} | \sigma \rangle$ with just the magnetic part[3] of $\tilde{\mathcal{U}} \propto \mathbf{M} \cdot \tilde{\sigma}$ [24], where $\mathbf{M}$ is defined as the probed local magnetic moment of an ion in the system, perpendicular to the momentum transfer $\mathbf{Q}$. Denoting the final and initial neutron spin states σ', σ as either up $|+\rangle$ or down $|-\rangle$, we obtain 4 processes: 2 spin flip processes, $|+\rangle \rightarrow |-\rangle$ and $|-\rangle \rightarrow |+\rangle$ as well as 2 non-spin flip processes, $|+\rangle \rightarrow |+\rangle$ and $|-\rangle \rightarrow |-\rangle$. $\mathbf{M} \cdot \tilde{\sigma}$ has three terms namely $M^x \sigma^x + M^y \sigma^y + M^z \sigma^z$. The first two terms with σ_y and σ_x, flip the spin of the neutron since σ_x, σ_y may be written as creation and annihilation operators of up/down states, while the action of σ_z will return back its eigenstates. This leads to:

$$\langle + | \tilde{\mathcal{U}} | + \rangle \quad \propto \quad M^z, \tag{2.18}$$

$$\langle - | \tilde{\mathcal{U}} | - \rangle \quad \propto \quad M^z, \tag{2.19}$$

$$\langle - | \tilde{\mathcal{U}} | + \rangle \quad \propto \quad (M^x + \mathrm{i} M^y), \tag{2.20}$$

$$\langle + | \tilde{\mathcal{U}} | - \rangle \quad \propto \quad (M^x - \mathrm{i} M^y). \tag{2.21}$$

The above expressions show that if the local magnetic moment probed in the sample is pointing along the neutron polarization axis $\hat{\mathbf{z}}$, the neutron spin will not flip. However, if it is pointing perpendicular to neutron polarization (and also perpendicular to $\mathbf{Q}$) the neutron spin will flip.

[3] We do not treat the nuclear structural and nuclear magnetic contributions here.

Summarizing, we find that the neutron is an exemplary probe of condensed matter systems. A scattering event obtains both nuclear and magnetic information. The magnetic part probes the spin-spin correlations in the sample perpendicular to neutron momentum transfer $\mathbf{Q}$ and one may further resolve the contributions to the SF and NSF channel using polarized neutron scattering. The SF channel has information of spins perpendicular to the neutron polarization while the NSF channel contains information about spins parallel to the neutron polarization. In the next sections, we derive the correlation functions $\langle S_j^\alpha S_{j'}^\beta \rangle$ using the large-N approximation and mean-field theory.

2.2 Mean-Field Theory

In this section, we will derive the expressions for the spin-spin correlation function which is an important ingredient in magnetic neutron scattering (see Sec. 2.1), using the mean-field formalism (MFT). Our analysis closely follows that of the Refs. [35, 36] which should be consulted for further details. We begin with the general Heisenberg Hamiltonian:

$$\mathcal{H} = \frac{1}{2} \sum_{i,j,a,b} \sum_{\mu,\nu} J_{ab}^{\mu\nu}(i,j) S_{ia}^{\mu} S_{jb}^{\nu} - \sum_{i,a,\mu} h_{ia}^{\mu} S_{ia}^{\mu}. \tag{2.22}$$

Here, i, j denote denote sites on the parent Bravais lattice (FCC lattice for the case of the pyrochlore lattice, see Appendix A.2) and a, b label the sublattices. μ, ν are the spin components. S_{ia}^{μ} represents the μ-th component of a classical spin at Bravais lattice site i with sublattice label a. $J_{ab}^{\mu\nu}(i,j)$ is the adjacency matrix element (see Appendix A.4), connecting the spin components (μ,ν) residing on sites (i,a) and (j,b). The factor of $1/2$

accounts for double counting and h_{ia}^{μ} is a magnetic field interacting with the spin on site (i, a). We utilize the formalism of variational MFT, where we assume a simple form of the density matrix [35, 36]. Specifically, the full many-body density matrix is written as a product of the single site density matrices. The variational parameters are then these single site density matrices which are varied to minimize the free energy. The free energy is given by:

$$F = E - TS, \tag{2.23}$$

where T is the temperature, S is the entropy and E is the internal energy. Using the many-body density matrix (ρ) we write down the variational free energy F_v, as given below:

$$F_v = \mathrm{Tr}[\rho\mathcal{H}] + T\,\mathrm{Tr}[\rho\,\ln(\rho)], \tag{2.24}$$

where the Trace (Tr) is taken over the spins. The variational free energy F_v, provides an upper bound to the actual free energy F i.e. $F_v > F$ [36]. The minima of F_v is then our best approximation of the minima of the true (unknown) free energy F. For a system of N un-entangled particles, the MF form of ρ is given by the product of the single particle density matrices ρ_i^a:

$$\rho = \prod_{i,a} \rho_i^a(\mathbf{S}_{ia}), \tag{2.25}$$

where the product is a direct product of individual Hilbert (vector) spaces of each spin $\mathbf{S}_{ia}$. Using Lagrange multipliers (ξ, $\mathbf{A}_{ia}$) to enforce the constraints:

$$\begin{aligned} \mathrm{Tr}[\rho_i^a] &= 1, \qquad (2.26) \\ \mathrm{Tr}[\rho_i^a \mathbf{S}_{ia}] &= \mathbf{m}_{ia}, \qquad (2.27) \end{aligned}$$

we rewrite the variational free energy as (Eq. (2.5a) in Ref. [35]):

$$F_v = \mathrm{Tr}[\rho\mathcal{H}] + \sum_{i,a} T\ (\mathrm{Tr}[\rho_{ia}\ln(\rho_{ia}) - \xi_{ia}\rho_{ia} - \rho_{ia}\mathbf{S}_{ia}\cdot\mathbf{A}_{ia}] + \mathbf{m}_{ia}\cdot\mathbf{A}_{ia} + \xi_{ia})\,. \qquad (2.28)$$

Here $\mathbf{m}_{ia}$ is a vector-order parameter. Differentiating F_v w.r.t. ρ_{ia}, we obtain:

$$(\ln(\rho_{ia}) + 1) - \xi_{ia} - \mathbf{S}_{ia}\cdot\mathbf{A}_{ia} = 0, \qquad (2.29)$$

which yields:

$$\rho_{ia} = C_{ia}\ e^{(\mathbf{S}_{ia}\cdot\mathbf{A}_{ia})}. \qquad (2.30)$$

Here $C_{ia} = e^{(\rho_{ia}-1)}$. Using the normalization condition $\mathrm{Tr}[\rho_i^a] = 1$ and solving a hyper-spherical integral [35], we obtain:

$$C_{ia}^{-1} = \mathrm{Tr}[e^{(\mathbf{S}_{ia}\cdot\mathbf{A}_{ia})}] = \frac{4\pi}{|\mathbf{A}_{ia}|}\sinh(|\mathbf{A}_{ia}|) = \mathcal{Z}_{ia}, \qquad (2.31)$$

where $\mathcal{Z}_{ia}$is the single particle partition function. Thus,

$$\rho_{ia} = \frac{e^{(\mathbf{S}_{ia}\cdot\mathbf{A}_{ia})}}{\mathcal{Z}_{ia}}. \qquad (2.32)$$

Substituting the above equation and Eq. (2.27) in Eq. (2.28), we obtain [35, 36]:

$$F_v = \frac{1}{2}\sum_{i,j,a,b}\sum_{\mu,\nu} J^{\mu\nu}_{ab}(i,j) m^{\mu}_{ia} m^{\nu}_{jb} - \sum_{i,a,\mu} h^{\mu}_{ia} m^{\mu}_{ia} + T\sum_{i,a}(\mathbf{m}_{ia}\cdot\mathbf{A}_{ia} - \ln(\mathcal{Z}_{ia})). \tag{2.33}$$

From the second constraint, we find the relationship between $\mathbf{A}_{ia}$ and $\mathbf{m}_{ia}$ (see Eq. (2.7a) in Ref. [35]):

$$\mathbf{m}_{ia} = \mathbf{A}_{ia}\left(\coth(|\mathbf{A}_{ia}|) - \frac{1}{|\mathbf{A}_{ia}|}\right), \tag{2.34}$$

which on Taylor expanding the hyperbolic cotangent function to first order, yields:

$$\mathbf{A}_{ia} = 3\mathbf{m}_{ia}. \tag{2.35}$$

Expanding the logarithm in Eq. (2.33) and substituting the above equation in Eq. (2.33), the free energy is written in terms of the order parameters $\mathbf{m}_{ia}$ which takes the following form [35, 36]:

$$F_v = \frac{1}{2}\sum_{i,j,a,b}\sum_{\mu,\nu} m^{\mu}_{ia}\left(3\delta_{\mu\nu}\delta_{ij}\delta_{ab}\,T + J^{\mu\nu}_{ab}(i,j)\right) m^{\nu}_{jb} - \sum_{i,a,\mu} h^{\mu}_{ia} m^{\mu}_{ia} - T\,N_{\text{tot}}\,\ln(C). \tag{2.36}$$

Here C is a model dependent constant. N_{tot} is the total number of sites in the lattice. We now Fourier transform the above equation using [36]:

$$m^{\mu}_{ia} = \sum_{\mathbf{q}} m^{a,\mu}_{\mathbf{q}} e^{i\mathbf{q}.\mathbf{R}_{ia}}, \tag{2.37}$$

$$J^{\mu\nu}_{ab}(i,j) = \frac{1}{N_{\text{B}}}\sum_{\mathbf{q}} J^{\mu\nu}_{ab}(\mathbf{q}) e^{i\mathbf{Q}\cdot(\mathbf{R}^a_i - \mathbf{r}^b_j)}, \tag{2.38}$$

where $\mathbf{R}_{ia}$ is the position of the spin in Bravais lattice point i with sublattice label a within the unit cell and $N_{\rm B}$ is the number of Bravais lattice sites. The Fourier transformed variational free energy divided by $N_{\rm B}$, denoted by $\mathcal{F}_v = F_v(\mathbf{q})/N_{\rm B}$, is given by [35, 36]:

$$\mathcal{F}_v = \frac{1}{2}\sum_{a,b,\mu,\nu,}\sum_{\mathbf{q}} m_{\mathbf{q}}^{a\mu}\left(3T\,\delta_{ab}\delta_{\mu\nu} + J_{ab}^{\mu\nu}(\mathbf{q})\right) m_{-\mathbf{q}}^{b\nu} - \sum_{a,b,\mu,\nu,}\sum_{q}\left(m_{\mathbf{q}}^{a\mu}h_{\mathbf{q}}^{a\mu}\delta_{ab}\delta_{\mu\nu}\right) - T\,N_{\rm s}\,\ln(C). \tag{2.39}$$

Here $N_{\rm s} = N_{\rm tot}/N_{\rm B}$ is the number of sublattices in each unit cell. To diagonalize the second order term in the above expression, we transform to the normal modes of the order parameter:

$$m_{\mathbf{q}}^{a\mu} = \sum_{\alpha=1}^{N_{\rm s}}\sum_{x=1}^{3}\phi_{\mathbf{q}}^{\alpha,x}U_{a\mu}^{\alpha x}(\mathbf{q}), \tag{2.40}$$

where α and x label the normal modes and $U(\mathbf{q})_{a\mu}^{\alpha x}$ is the (a,μ) component of the (α,x) eigenvector of the Fourier transformed interaction matrix $J(\mathbf{q})$ given in Eq. (2.38). Thus, $U(\mathbf{q})$ is the unitary matrix which diagonalizes $J(\mathbf{q})$ via a unitary transformation given by $U(\mathbf{q})^\dagger\,J(\mathbf{q})\,U(\mathbf{q}) = \lambda(\mathbf{q})$. Substituting Eq. (2.40) in Eq. (2.39), the free energy up to quadratic order is given by [35, 36]:

$$\mathcal{F}_v = \frac{1}{2}\sum_{\mathbf{q}}\sum_{\alpha,x}\phi_{\mathbf{q}}^{\alpha x}\left(3T + \lambda_x^{\alpha}(\mathbf{q})\right)\phi_{-\mathbf{q}}^{\alpha x} - T\sum_{\mathbf{q}}\phi_{\mathbf{q}}^{\alpha x}\tilde{h}_{\mathbf{q}}^{\alpha x} - T\,N_{\rm s}\,\ln(C), \tag{2.41}$$

where $\lambda_x^{\alpha}(\mathbf{q})$ is the eigenvalue of $J(\mathbf{Q})$ corresponding to the (α,μ) eigenvector. In the second term, $\tilde{h}_{\mathbf{q}}^{\alpha x}$ is given by:

$$\tilde{h}_{\mathbf{q}}^{\alpha x} = \frac{1}{T}\sum_{a,\mu}h_{\mathbf{q}}^{a\mu}U_{a\mu}^{\alpha x}(\mathbf{q}). \tag{2.42}$$

The partition function using the variational free energy is given by the general definition [36]:

$$\mathcal{Z} = \mathrm{Tr}[\, e^{\frac{-\mathcal{F}_v}{T}} \,], \tag{2.43}$$

where the trace is over all the normal modes and given by :

$$\mathrm{Tr} \equiv \prod_{\mathbf{q},\alpha,x} \int_{-\infty}^{\infty} d\phi_{\mathbf{q}}^{\alpha x}. \tag{2.44}$$

Using Eq. (2.41), the partition function then takes the following form [36]:

$$\mathcal{Z} = \prod_{\mathbf{q},\alpha,x} \left(\frac{2\pi}{3 + \frac{\lambda_x^\alpha(\mathbf{q})}{T}} \right)^{\frac{1}{2}} \exp\left[\frac{|\tilde{h}_{\mathbf{q}}^{\alpha x}|^2}{2(3 + \frac{\lambda_x^\alpha(\mathbf{q})}{T})} \right]. \tag{2.45}$$

The correlation functions of the normal modes are now given by double differentiating w.r.t. $\tilde{h}_{\mathbf{q}}^{\alpha x}$, giving:

$$\langle \phi_{\mathbf{q}}^{\alpha x} \phi_{\mathbf{q}'}^{\beta y} \rangle = \frac{\delta_{\alpha\beta}\delta_{xy}\delta_{\mathbf{q}+\mathbf{q}',0}}{3 + \frac{\lambda_x^\alpha(\mathbf{q})}{T}}. \tag{2.46}$$

The spin-spin correlation functions are given in terms of the normal modes by [36]:

$$\langle S_{ia}^\mu S_{jb}^\nu \rangle = \sum_{\mathbf{q},\mathbf{q}'} \sum_{\alpha,\beta} \sum_{x,y} \langle \phi_{\mathbf{q}}^{\alpha x} \phi_{\mathbf{q}}^{\beta y} \rangle U_{a\mu}^{\alpha x}(\mathbf{q}) U_{b\nu}^{\beta y}(\mathbf{q}) \times e^{-i\mathbf{q}\cdot\mathbf{R}_{ia} - i\mathbf{q}'\cdot\mathbf{R}_{jb}}. \tag{2.47}$$

For the purposes of this thesis, we are interested in the Fourier transformed total[4] spin-spin correlations $S(\mathbf{Q})$ (often called spin susceptibility or the spin structure factor colloquially)

[4] Total here refers to summing over all sublattice contributions.

which for isotropic spins is given by:

$$S(\mathbf{Q}) = \frac{1}{N_{\mathrm{B}}} \sum_{\mu,\nu} \sum_{i,j,a,b} \langle S^{\mu}_{ia}\, S^{\nu}_{jb} \rangle\, \delta_{\mu\nu}\, \exp[\mathrm{i}\mathbf{Q} \cdot (\mathbf{R}_{ia} - \mathbf{R}_{jb})]. \tag{2.48}$$

Here $\mathbf{Q} = \mathbf{G} + \mathbf{q}$, where $\mathbf{Q}$ is the analog of momentum transfer and may take any value, $\mathbf{G}$ are the reciprocal lattice vectors and $\mathbf{q}$ is a wavevector in the first Brillouin zone (see Appendix A.2). Substituting Eq. (2.46) and Eq. (2.47) in Eq. (2.48), we obtain the desired result :

$$\frac{1}{N_{\mathrm{B}}}\, S(\mathbf{Q}) = \sum_{a,b,\alpha}^{N_{\mathrm{s}}} \sum_{x,\mu}^{3} \left(\frac{U^{\alpha x}_{a\mu}(\mathbf{q}) U^{\alpha x}_{b\mu}(\mathbf{q})}{3 + \frac{\lambda^{\alpha}_{x}(\mathbf{q})}{T}} \right) e^{\mathrm{i}\mathbf{G}\cdot(\mathbf{r}_a - \mathbf{r}_b)}, \tag{2.49}$$

where $\mathbf{r}_a$ and $\mathbf{r}_b$ are locations of the sublattices a, b in the unit cell. The structure factors (for the nearest-neighbour Heisenberg model on a pyrochlore lattice) computed using mean-field theory are displayed in Fig. 2.4. To compute the structure factor, first, for a given $\mathbf{Q}$, we obtain the reciprocal lattice vector $\mathbf{G}$ and the wavevector in the FBZ, $\mathbf{q}$, using $\mathbf{Q} = \mathbf{G} + \mathbf{q}$. Then, the eigenvectors $U(\mathbf{q})$ and eigenvalues $\lambda(\mathbf{q})$, are computed and the formula given above is utilized. The above equations are valid for $T > T_c$ where the MF critical temperature is given by:

$$T_c = -\frac{\lambda^{\alpha}_{x}(\mathbf{q}_{\mathrm{ord}})}{3}, \tag{2.50}$$

where $\mathbf{q}_{\mathrm{ord}}$ are the wavevectors where the eigenvalues are minimum for all eigenbands (referring to the $3N_{\mathrm{s}}$ eigenvalues in $\mathbf{q}$-space) globally. The negative sign is because the global minimum eigenvalues will be negative. At $T = T_c$, the denominator in Eq. (2.49) goes to zero[5]. At $T = T_c + \Delta$, for arbitarily small number Δ, the intensity of $S(\mathbf{Q})$ at $\mathbf{q}_{\mathrm{ord}}$

[5]Right above criticality, the structure factor shows divergening peaks at the wavevectors, $\mathbf{q}_{\mathrm{ord}}$.

is maximum[6] as shown in panel (d) of Fig. 2.4. To characterize $S(\mathbf{Q})$ for different exchange parameters we utilize reduced temperature τ, which acts as a measure of separation from criticality and is given by:

$$\tau \equiv \frac{T - T_c}{T_c} \tag{2.51}$$

Thus, we have obtained expressions for the total spin-spin correlations $S(\mathbf{Q})$, in this thesis which shall be utilized in later chapters. In the next section, we shall utilize another method, known as the large-N approximation to obtain the spin structure factors. This will enable us to study polarized neutron scattering in later chapters.

[6]The intensity is also controlled by the numerator of Eq. (2.49), called the form factors discussed in Chap. 4

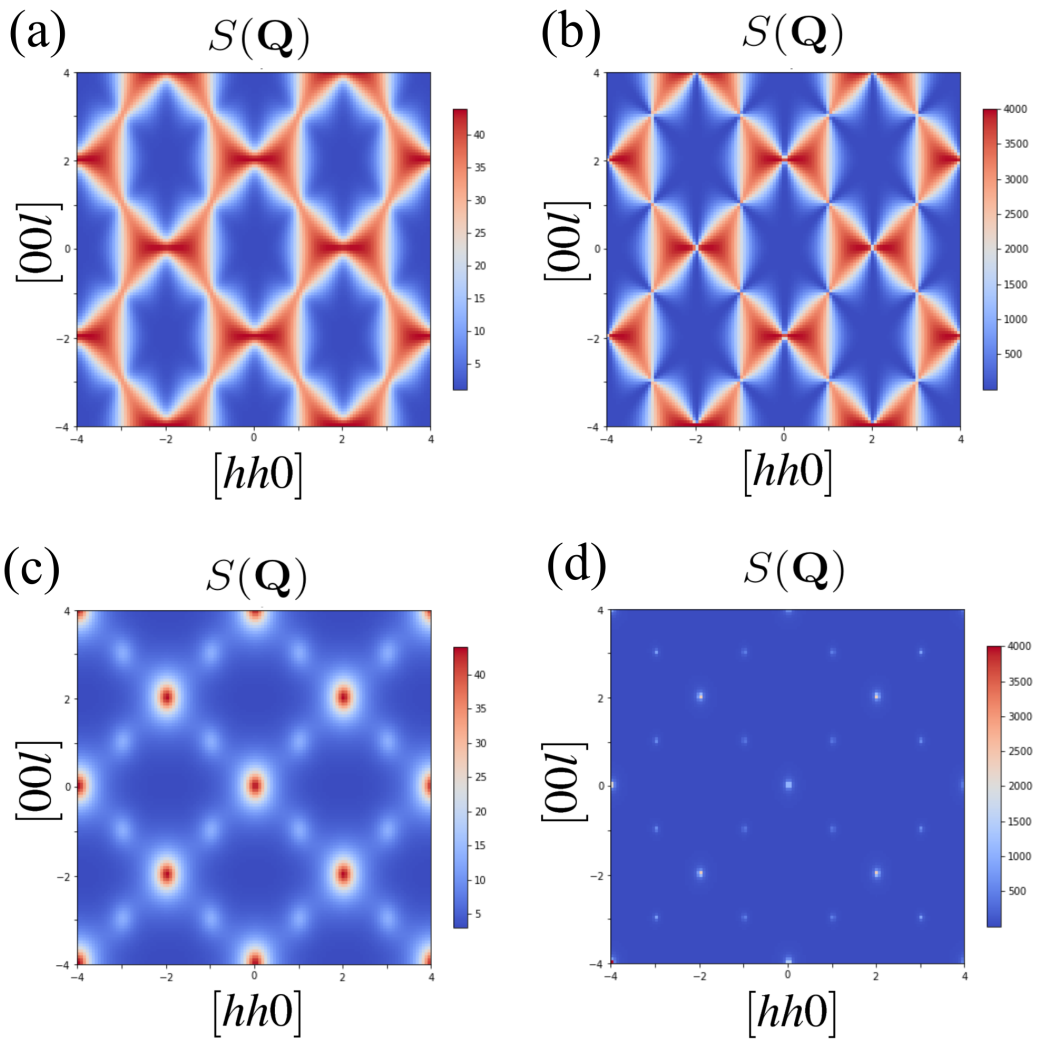

Figure 2.4: Figures show the spin structure factors $S(\mathbf{Q})$ (using MFT) in the $[hhl]$-plane for nearest-neighbour Heisenberg spins on a pyrochlore lattice. The left panels (a) and (c) are at (relatively) high temperatures given by $\tau = 10^{-1}$, while the panels on the right (b) and (d) are at lower temperature characterized by $\tau = 10^{-3}$. The axes are in units of $\frac{2\pi}{a}$. (a), (b) have anti-ferromagnetically ($J/T = 1$) interacting spins while (d), (c) have ferromagnetic coupling($J/T = -1$). The colors denote intensities in arbitary units.

2.3 Large-N

In this section, we discuss the specifics of the Large-N approximation. Variants of this technique are often called by different names such as the spherical model [37, 38, 39] and the Onsager reaction field theory [40, 41]. Another technique called the self consistent Gaussian approximation [11, 42] is essentially equivalent to the large-N approximation described here [11, 43]. A modern reference to large-N expansions in the context of field theories may be found in Ref. [44]. The large-N approximation is quite effective in frustrated magnets and have been utilized to study the bulk pyrochlore [11, 15, 21, 42, 43, 45, 46], pyrochlore thin films [47] as well as the kagomé lattice [14, 48].

The key idea is to soften the spin normalization constraint $|\mathbf{S}|^2 = S^2$, to spins obeying the normalization constraint only on average given by $\langle|\mathbf{S}|^2\rangle = S^2$. We incorporate the softened spin normalization constraint in the partition function using Lagrange multiplier λ, which in the limit of infinite spin components, $N \to \infty$, becomes exactly solvable. Although the results are strictly valid for $N \to \infty$, for spins on a pyrochlore, they are found to agree well with Monte Carlo simulations of the Heisenberg ($N = 3$) [42, 43] as well as the Ising ($N = 1$) model [43]. The $N = 2$ case is more subtle and collapses to the $N = 1$ case due to an order by disorder mechanism [43].

We briefly describe the derivation in this section and refer the interested reader to the Refs. [11, 15, 43] for further details. We shall solely concentrate on the Heisenberg and Ising cases in this thesis (for the pyrochlore lattice) and our goal is to obtain the spin-spin correlation functions, which will be utilized in later chapters. We begin with the general

Hamiltonian with $\mathcal{O}(N)$ spins:

$$\mathcal{H} = \frac{1}{2}\sum_{i,j}\sum_{\mu\nu}^{N} J_{ij}^{\mu\nu} S_i^{\mu} S_j^{\nu}, \tag{2.52}$$

where S_i^{μ} are classical $\mathcal{O}(N)$ spins, i,j refer to the sites (notation changed from previous section) and μ, ν are the spin components. $J_{ij}^{\mu\nu}$ is the adjacency matrix (see Appendix A.4) in real space with matrix element 1 if the sites (and components) are connected and 0 if not. The partition function $\mathcal{Z}$, is defined by:

$$\mathcal{Z} = \sum \exp\left(-\beta\mathcal{H}\right). \tag{2.53}$$

Here β is the inverse temperature and the sum is over all possible states. For N-component spins with magnitude of each component as unity, we have the normalization constraint, $|\mathbf{S}|^2 = N$. We enforce this constraint using a delta function $\delta(|\mathbf{S}|^2 - N)$. The partition function is then rewritten as:

$$\mathcal{Z} = \prod_j \int (\prod_{\mu} dS_j^{\mu}) \left[\delta(|\mathbf{S}_j|^2 - N)\right] \exp(-\beta\mathcal{H}). \tag{2.54}$$

Here the first product is over the lattice sites j and the second product is over spin components μ. The integral takes values from $-\infty$ to $+\infty$ for the scalar fields for each spin component S_j^{μ}. The δ function is re-expressed using its integral form $\delta(x) = \int_{-\infty}^{\infty} d\xi e^{\mathrm{i}\xi x}$

which yields:

$$\mathcal{Z} = \prod_j \int_{-\infty}^{\infty} (\prod_\mu dS_j^\mu d\xi_j) \exp\left[-\frac{1}{2}\sum_j (\mathrm{i}\xi_j(|\mathbf{S}_j|^2 - N)\right] \exp(-\beta\mathcal{H}). \tag{2.55}$$

Redefining $\xi_{ij}^{\mu\nu} = \xi_i \delta^{\mu\nu}\delta_{ij}$, rearranging the exponents and using the fact that for isotropic spins $J_{ij}^{\mu\nu} = J_{ij}\delta^{\mu\nu}$, we obtain:

$$\mathcal{Z} = \int \mathcal{D}\mathbf{S}\, \mathcal{D}\xi \;\; \exp\left[\frac{N}{2}\mathrm{Tr}[\mathrm{i}\xi]\right] \exp\left[-\frac{1}{2}\sum_{ij}\sum_{\mu\nu} S_i^\mu M_{ij}^{\mu\nu} S_j^\nu\right], \tag{2.56}$$

where the short hand for the integral measures (over sites j and components μ) are given by:

$$\mathcal{D}\mathbf{S} \;\; = \;\; \prod_{\mu,j} dS_j^\mu, \tag{2.57}$$

$$\mathcal{D}\xi \;\; = \;\; \prod_j d\xi_j, \tag{2.58}$$

and the matrix $M_{ij}^{\mu\nu}$ in Eq. (2.56), is given by :

$$M_{ij}^{\mu\nu} = \mathrm{i}\xi_i\delta^{\mu\nu}\delta_{ij} + \beta J_{ij}^{\mu\nu} = (\mathrm{i}\xi + \beta J)_{ij}^{\mu\nu}\,. \tag{2.59}$$

The integral over the each spin component is now a Gaussian and the integrals are evaluated to give:

$$\mathcal{Z} = \int \mathcal{D}\xi \;\; \exp\left[\frac{N}{2}\mathrm{Tr}[\mathrm{i}\xi]\right] \left[\frac{(2\pi)^{N_\mathrm{s}}}{\det M}\right]^{N/2}, \tag{2.60}$$

where N_s is the number of sites and N is the number of spin components. Extra factors

of 2π are dropped. Using the standard identity $\ln(\det M) = \mathrm{Tr}(\ln M)$ to write:

$$\frac{1}{\sqrt{\det M}} = \exp\left[-\frac{1}{2}\mathrm{Tr}[\ln M]\right], \tag{2.61}$$

and substituiting Eq. (2.61) in Eq. (2.60) we obtain:

$$\mathcal{Z} = \int \mathcal{D}\xi \ \exp\left[-\frac{N}{2}(-\mathrm{Tr}[\lambda] + \mathrm{Tr}[\ln M])\right]. \tag{2.62}$$

Here $\lambda = \mathrm{i}\xi$[7] and λ_j is equivalent on all sites [11]. We see that for $N \to \infty$, the function inside the exponent diverges. A saddle point integral is computed for $N \to \infty$, near the maximum of the exponent and yields the spin length constraint [11] given by:

$$\langle S_i^\mu S_i^\nu \rangle = \delta_{\mu\nu}(\lambda + \beta J)^{-1}_{ii}, \tag{2.63}$$

where J_{ii} is an adjacency matrix element for the same site. This is true for isotropic spins and we see that the different spin components are uncorrelated. We set the spin normalization for three component spins, $\langle \mathbf{S}_i \cdot \mathbf{S}_i \rangle = 1$. Individual components are then given by $\langle S_j^\mu S_j^\mu \rangle = 1/3$. This, on summing over all sites, yields [11]:

$$\mathrm{Tr}\,[\lambda \mathbb{I} + \beta J]^{-1} = \frac{N_\mathrm{s}}{3}, \tag{2.64}$$

where N_s is the total number of sites. On Fourier transformation, M^{-1} in Eq. (2.59)

[7] In the following analysis, to compute the integral in Eq. (2.62), one has to analytically continue the contour from the real axis, and deform it to run across the saddle point on the imaginary axis, however the details of the contour do not matter, except that it passes over the saddle point parallel to the real axis.

becomes block diagonal and we obtain a normalization condition in Fourier space given by [11]:

$$\sum_{\mathbf{q}\in\mathrm{FBZ}}\sum_{a}\left[\lambda\mathbb{I}+\beta J(\mathbf{q})\right]^{-1}_{aa}=\frac{N_{\mathrm{s}}}{3}, \tag{2.65}$$

where $J(\mathbf{q})$ is the Fourier transformed interaction matrix (see Appendix A.4). The sum over $\mathbf{q}$ has to be taken over the first Brillouin zone (FBZ) (see Appendix A.2) and a are the sublattice labels. For the case of the pyrochlore, $N_{\mathrm{s}}=N_{\mathrm{FCC}}\,N_{\mathrm{subs}}=4N_{\mathrm{FCC}}$ where N_{FCC} is the number of Bravais lattice points which in this case is a face centered cubic (FCC) lattice (see Ref. [49] and Appendix A). N_{subs} are the number of sublattices in an unit cell which is 4 for the case of the pyrochlore lattice. We shall utilize the above equation Eq. (2.65), to self consistently solve for λ, which is dependent on temperature. From the partition function, Eq. (2.62) we obtain the spin-spin correlations $\langle S_i^\mu S_j^\nu\rangle$ by differentiating $\ln(\mathcal{Z})$ w.r.t. to J_{ij} [11, 15, 43, 47] which yields:

$$\langle S_i^\mu S_j^\nu\rangle=\delta_{\mu\nu}(\lambda\mathbb{I}+\beta J)^{-1}_{ij}. \tag{2.66}$$

In Fourier space, this translates to the key equation used in this thesis (valid for isotropic spins), defined below [11, 21, 42, 43]:

$$\langle S_a^\mu(-\mathbf{q})S_b^\nu(\mathbf{q})\rangle=(\lambda\mathbb{I}+\beta J(\mathbf{q}))^{-1}_{ab}\delta_{\mu\nu}. \tag{2.67}$$

The spin structure factor $S(\mathbf{q})$, introduced in the previous section (see Eq. (2.48)) is then obtained as [21]:

$$S(\mathbf{q})=\sum_{\mu,\nu}\sum_{a,b}\left(\lambda\mathbb{I}+\beta J(\mathbf{q})\right)^{-1}_{ab}\,\delta_{\mu\nu}. \tag{2.68}$$

We remind the reader that here $\mathbf{q}$ refers to any wavevector (in and beyond the FBZ). Plots of the spin structure factors (using large-N) in reciprocal space are provided in Chapter 4 (Fig. 4.4, Fig. 4.6, Fig. 4.9).

In this section, we used the large-N approximation to compute the spin-spin correlation functions which shall be used in the later sections. We saw that to make sense of the theory, the Lagrange multiplier λ has to be computed self-consistently using Eq. (2.65). We give a brief account of how this is implemented and then move on to the next chapters where this formalism is utilized.

Implementation

To solve for the spin length constrain given by:

$$\sum_{\mathbf{q}\in\mathrm{FBZ}} \sum_{a} [\lambda \mathbb{I} + \beta J(\mathbf{q})]^{-1}_{aa} = \frac{N_\mathrm{s}}{3}, \tag{2.69}$$

we transform it to the diagonal basis where the above equation reads as:

$$\sum_{\mathbf{q}\in\mathrm{FBZ}} \sum_{a} \frac{1}{\lambda + \beta E^{aa}(\mathbf{q})} = \frac{N_\mathrm{s}}{3}. \tag{2.70}$$

Here $E^{aa}(\mathbf{q})$ are the diagonal entries i.e. the eigenvalues (labeled by a) of $J(\mathbf{q})$, which are in general $\mathbf{q}$-dependent.

For the purpose of this thesis, we solved the above constraint equation numerically using Python and Numpy [50]. This was done by simultaneously trying to resolve two conditions (called C_1 and C_2 here respectively) which were obtained by rearranging Eq. (2.65) which

are given by:

$$C_1 \quad : \quad \sum_{\mathbf{q}\in \mathrm{FBZ}} \sum_{a} \frac{1}{\lambda_{\mathrm{i}} + \beta E^{aa}(\mathbf{q})} - \frac{N_{\mathrm{s}}}{3} = \delta_{\mathrm{i}}, \tag{2.71}$$

$$C_2 \quad : \quad \frac{3}{N_{\mathrm{s}}} \sum_{\mathbf{q}\in \mathrm{FBZ}} \sum_{a} \frac{1}{1 + \frac{\beta E^{aa}(\mathbf{q})}{\lambda_{\mathrm{i}}}} = \lambda_{\mathrm{i+1}}. \tag{2.72}$$

Here i labels the iterations performed to resolve the above two conditions C_1 and C_2. To compute the above sums one has to sample $\mathbf{q}$-points over the FBZ (see Appendix A.2 and Fig. A.2). Then for each $\mathbf{q}$, the sum over the eigenindex a is computed. The implementation scheme to find λ is briefed below:

1. Consider an initial guess, λ_{i}.
2. Compute C_1. If $\delta_1 < 10^{-5}$, stop. Output λ_{i} as the final result.
3. In C_1, if $\delta_1 > 10^{-5}$, use λ_{i} in C_2 to find new guess point $\lambda_{\mathrm{i+1}}$.
4. Use $\lambda_{\mathrm{i+1}}$ in C_1 to find $\delta_{\mathrm{i+1}}$
5. If $\delta_{\mathrm{i+1}} < \delta_{\mathrm{i}}$, continue the process, if not then add or subtract (depending on the sign of $\delta_{\mathrm{i+1}}$, subtract if $\delta_{\mathrm{i+1}} < 0$) $\Delta\lambda = \pm 10^{-3}$ to $\lambda_{\mathrm{i+1}}$ and use as new guess point $\lambda_{\mathrm{i+2}}$.
6. Reiterate till $\delta < 10^{-5}$ and $|\lambda_{\mathrm{i+1}} - \lambda_{\mathrm{i}}| < 10^{-4}$ and make sure that $\lambda_{\mathrm{i}} > 0$.
7. Return final λ

This procedure essentially allows us to progressively get closer to the true unknown λ by iterating alternatively between $\lambda + \eta$ and $\lambda - \eta$, as η, an arbitary number, gets smaller.

Below a certain temperature, an instability develops and λ either diverges and solutions to Eq. (2.70) cannot be found or converges to zero (see Fig. 2.5).

Thus, in this chapter, we developed the tools required for our subsequent discussions. We obtained expressions for neutron scattering, where the primary quantity of interest is a spin-spin correlation function. We also obtained expressions for the spin-spin correlations using MFT and large-N approximation. Finally, we obtained formulae for the structure factor, $S(\mathbf{Q})$, which is the ideal scattering obtained (same along both spin flip channel and non-spin flip channel since they are orthogonal) for isotropic interactions and isotropic g-factor [8]. Armed with these tools, we begin our discussions on spin ice, detailed in the next chapter.

[8]The g-factor connects spin components to magnetic dipole moments of an ion. For the case of isotropic g-factor, the magnetic moment of an ion lies along the same direction as its spin.

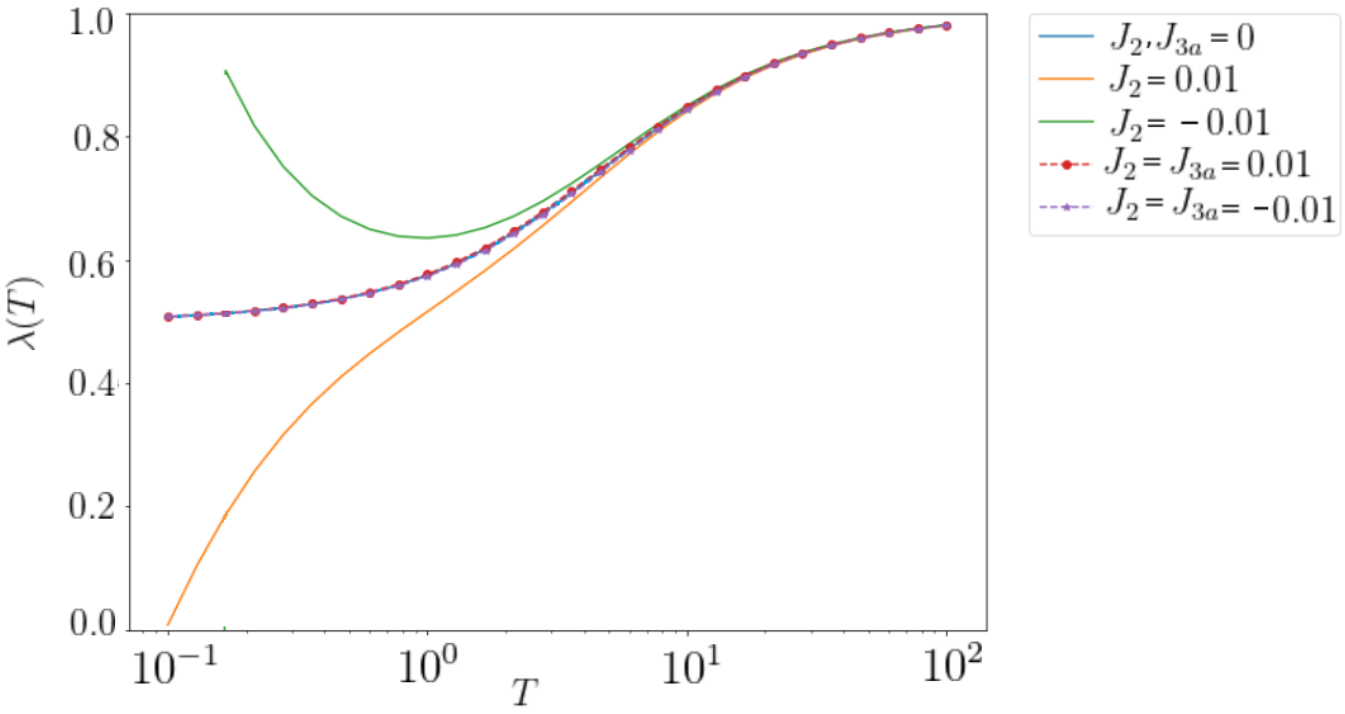

Figure 2.5: Figure showing λ vs T (in log-scale) for AFM Ising pyrochlore (see Chap. 3) with various further-neighbour interactions J_2 and J_{3a} (see Fig. 3.6(a) and Appendix A.4). Note that when there are no further-neighbour interactions $J_2 = J_{3a} = 0$, λ takes a value of 0.5 at low temperatures and 1.0 at high temperatures. For the extended spin ice (see Sec. 3.3.3, $J_2 = J_{3a} \equiv J' \neq 0$, for $-0.5 < J' < 0.25$, λ follows the same trend as that of just the nearest-neighbour case (the red, purple and blue lines coincide). Here we see λ for a negative J_2 diverges while a positive J_2 drops to 0.

Chapter 3

Polarized Neutron Scattering in Classical Spin Ice

3.1 Materials, motivation and models

In this section, we investigate the physics of classical spin ice [51], an extensively studied family of geometrically frustrated magnetic compounds with the chemical formula $R_2M_2O_7$. Here both M^{4+} (non-magnetic transition metal like Ti) and R^{3+} (magnetic rare earth ions like Dy and Ho) reside on an interpenetrating tetrahedral lattice (see Fig. 3.1(a) and Fig. A.1 in Appendix A). Canonical dipolar spin ice compounds are holmium titanate ($Ho_2Ti_2O_7$) [52, 53] and dysprosium titanate ($Dy_2Ti_2O_7$) [51, 54], which have been studied for the last three decades. Crystal electric fields result in a strong single ion-anisotropy (along the easy axis $\langle 111 \rangle$ directions) and a low-lying isolated ground state doublet [20].

Further, as detailed in Ref. [55], non-Ising exchange terms arise from high-rank inter-ionic multipolar interactions which are induced via weak super-exchange (mediated through the anions) and are highly suppressed[1]. Thus, this system may be modelled with a toy model of Ising pseudo-spins constrained to lie along the local ⟨111⟩ directions interacting via ferromagnetic interactions [20]. The Hamiltonian is given by:

$$\mathcal{H} = -J \sum_{\langle i,j \rangle} \mathbf{S}_i \cdot \mathbf{S}_j - D \sum_i (\mathbf{S}_i \cdot \hat{\mathbf{z}}_i)^2. \tag{3.1}$$

Here J is the interaction strength, D is single-ion anisotropy energy scale, i and j label nearest-neighbour sites. At temperatures below D, the effective moments $\mathbf{S}_i$, are constrained such that $\mathbf{S}_i = \sigma_i \hat{\mathbf{z}}_i$, where $\hat{\mathbf{z}}_i$ are along the local ⟨111⟩ axis and σ_i are Ising pseudo-spins and take values of ± 1. Rearranging the Hamiltonian yields:

$$\mathcal{H} = -J \sum_{\langle i,j \rangle} \sigma_i \cdot \sigma_j (\hat{\mathbf{z}}_i \cdot \hat{\mathbf{z}}_i), \tag{3.2}$$

$$= \frac{J}{3} \sum_{\langle i,j \rangle} \sigma_i \cdot \sigma_j, \tag{3.3}$$

where $\hat{\mathbf{z}}_i \cdot \hat{\mathbf{z}}_j = -\frac{1}{3}$ when i and j are on different sublattices. Thus, ferromagnetic interactions in the magnetic moments along ⟨111⟩ directions are modelled via an anti-ferromagnetic Ising model [20, 56]. We interpret $\sigma_i = \pm 1$ as the pseudo-spin either pointing outside the tetrahedra or inwards towards its centre along the easy ⟨111⟩ directions (see Fig. 3.1(b)). The anti-ferromagnetic Ising model on a pyrochlore lattice may be written as

[1] In Ref. [55], this was shown for $Ho_2Ti_2O_7$ and $Dy_2Ti_2O_7$ and the transverse exchange was theoretically found to be two orders of magnitude smaller than the nearest-neighbour Ising coupling.

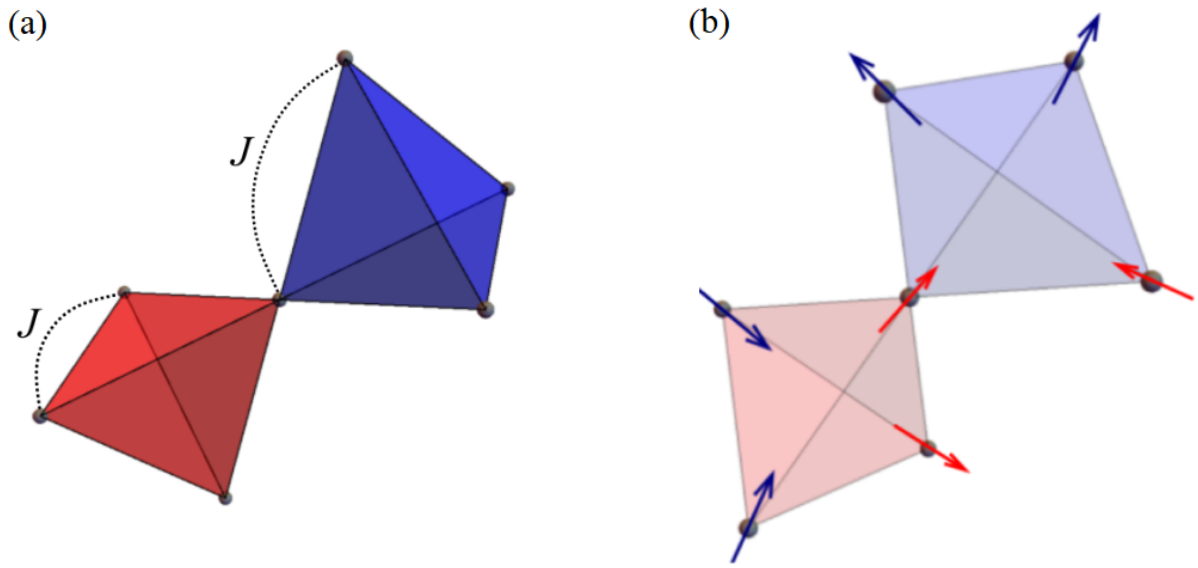

Figure 3.1: Panel (a) shows two tetrahedra in the pyrochlore lattice with nearest neighbour interaction J. (b) shows spins constrained along the local $\langle 111 \rangle$ directions following the 2-in 2-out ice-rules.

a sum over the spins in each tetrahedron (up to an additive constant) [3]:

$$\mathcal{H} = \frac{J}{6} \sum_{\boxtimes} \left(\sum_{i \in \boxtimes} \sigma_i \right)^2 . \tag{3.4}$$

The extra factor of $\frac{1}{2}$ is to account for double counting[2]. The first sum runs over tetrahedra ($\boxtimes$) and the second sum runs over spins in one single tetrahedron, which is minimized if $\sum_{i \in \boxtimes} \sigma_i = 0$, i.e. two of the spins are pointing in and two are pointing out (see Fig. 3.1(b)). The magnetic ground state manifold, composed of spin configurations with the lowest energy, is extensive in this case. There are several possibilities in which the spins may follow the two-in two-out rules and further, flipping the spins on a hexagon (in the kagomé

[2]The multiplicative factor of 1/3 will be dropped in the ensuing analysis.

layer, see Fig. A.4 and Fig. A.3) do not change the energy of the system. This is the source of the massive ground state degeneracy in spin ice and results in observable residual Pauling entropy [54]. Similar physics is observed in various other systems such as in cation ordering of inverse spinel (studied by Anderson [9, 20]) and in water ice where the two-in two-out rules have an exact analog, i.e. the Bernal-Fowler ice-rules which govern the displacements of protons in water ice [57].

The materials mentioned above, $Ho_2Ti_2O_7$ and $Dy_2Ti_2O_7$, are actually dipolar spin ice material with additional dipolar interactions [20] not considered in this work. However, the essential physics still remains valid in this model since the dipolar interactions were shown to project onto the ice-states and display projective equivalence [58]. While for dipolar spin ice, the NSF channel (in a neutron scattering experiment) shows a checkerboard pattern (see Fig. 3.2 **B**), for the nearest-neighbour model we find a **q**-independent (flat) NSF (see Fig. 3.2 **E**).

Theoretically, the physics of spin ice results in the ice-rules and this shows up as characteristic pinch-point [3] features (see Fig. 3.2, Fig. 3.7 and Fig. 3.8) which show the neutron scattering) in the spin-spin correlation function and in neutron scattering. This has been verified multiple times in simulations [15, 42, 45, 58]. Even though unpolarized neutron scattering experiments were done on $Ho_2Ti_2O_7$ before [52, 53, 59], it was only after careful polarized neutron scattering was done [19] that the pinch-points were properly resolved and clearly visible (see Fig. 3.2). However, there is a subtlety in the experiment described in Ref. [19]. Firstly, the experiment was done at $T = 1.7$K and not at $T = 0$K which is

[3]The bow-tie features in the structure factor and neutron scattering are called pinch-points in the literature. These are characteristic features of a system in a Coulomb phase and indicates the ice-rules being followed by the magnetic moments in the magnetic ground state.

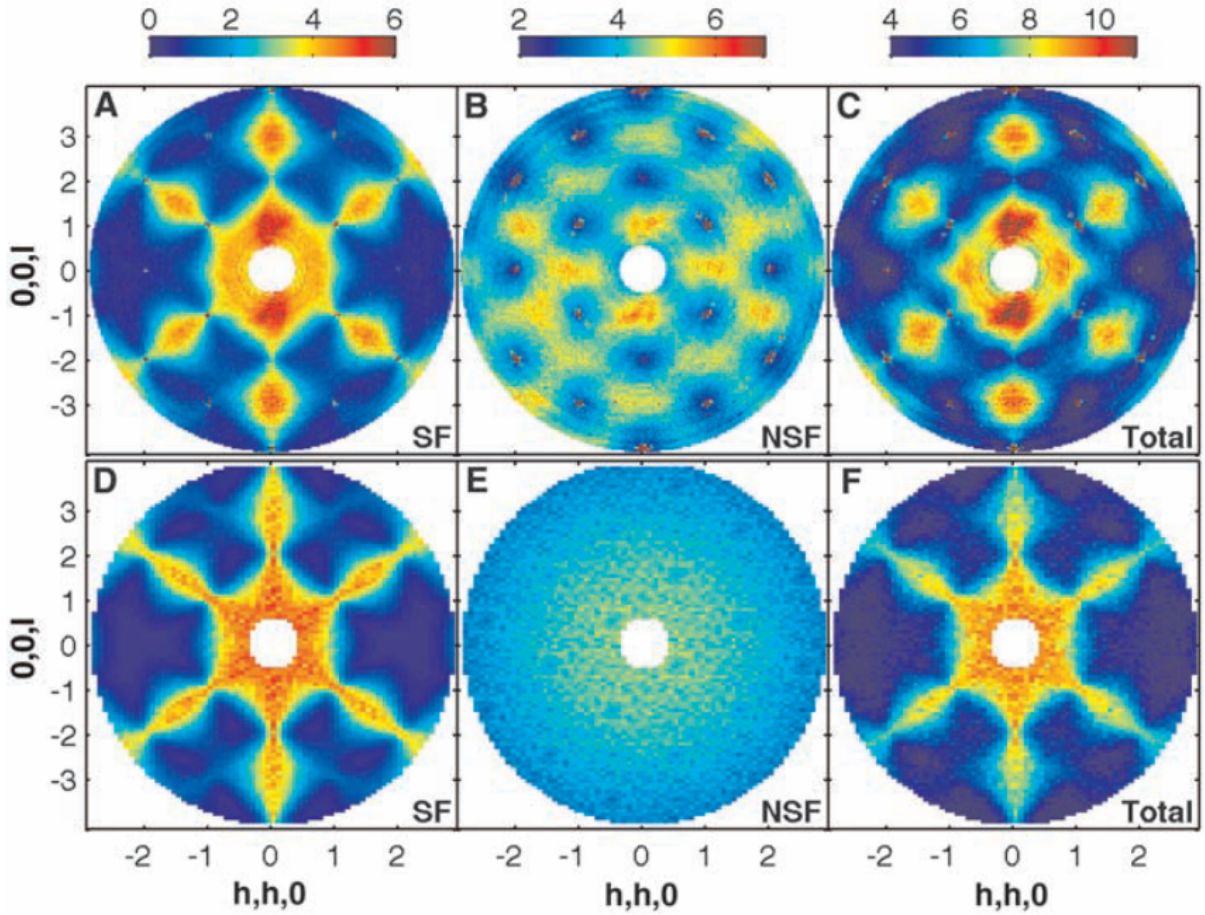

Figure 3.2: Results taken directly from Ref. [19]. Figures show (magnetic) polarized (elastic) neutron scattering results on $Ho_2Ti_2O_7$ in the SF channel (**A**), NSF channel (**B**) and the sum of the two channels, the total neutron scattering (**C**). The experiment was done at $T = 1.7$K Note the bow-tie features (at [111] and [200]) called pinch-points in panel (**A**) and (**C**). Panels **D**, **E**, **F** are Monte Carlo simulations. Panel **E** is the nearest neighbour model showing flat NSF in a Monte Carlo simulation. The gradation towards the origin is due to the inclusion of holmium form factor (see appendices in Ref. [19]). Panel **D** shows the SF channel and characteristic pinch-points at wavevectors [200] and [111] (and other symmetry related wavevectors). Results are taken directly from 2009 Science publication by Fennel *et.al.* [19] (licensed content title: Magnetic Coulomb phase in the spin ice $Ho_2Ti_2O_7$). Their results are displayed in this thesis after due permission from the licensed content publisher: "The American Association for the Advancement of Science" for licensed content publication in "Science" with License number: 4872570850019.

impossible experimentally and this is where the Coulomb phase is theoretically understood to exist. Further, the crossover from the paramagnetic regime to the Coulomb phase is signalled by a broad peak in the specific heat (magnetic part) and this occurs at $T \approx 1.9$K (see Fig. 3 in Ref. [53]) for $Ho_2Ti_2O_7$. Thus, this experiment was done right below crossover and arguably, not in the Coulomb phase. Monte Carlo simulations were also undertaken in the same work for the nearest-neighbour case, which show bow-tie features in the spin flip channel (SF) and a **q**-independent non-spin flip channel (NSF) in the $[hhl]$ plane. While the NSF is clearly **q**-independent in the simulation (gradation towards the origin is from adding the holmium form factor to the simulation), the experiment reveals checkerboard like structures reminiscent of further-neighbour interactions (such as in Fig. 3.10(c)).

Interestingly, Monte Carlo simulations of the nearest-neighbour model [60, 61] and the related spin-1/2 local XXZ model[4] in its classical SI regime [62], show the NSF channel to be completely flat and featureless (in the $[hhl]$ plane), but it is not understood why it is so. We shall attempt to build an intuitive proof of why the NSF channel is flat (in the $[hhl]$ plane) for all temperatures for AFM Ising spins on a pyrochlore lattice. In doing so, we shall also find two other cases with flat bands (extended spin ice [63] and Ising spins on a breathing pyrochlore) and expose the connection between the flat eigenbands and the flat NSF channel in the $[hhl]$ plane. First, we take a short detour through some basic results and then we shall provide the key results in this thesis.

[4]The XXZ model is given by an anisotropic bilinear exchange hamiltonian with inequivalent transverse (along local $\hat{\mathbf{z}}$) and longitudinal (in local $\hat{\mathbf{x}}$-$\hat{\mathbf{y}}$ plane) exchange couplings.

3.2 Preliminary Results

3.2.1 Emergent Fields, Fluxes and Monopoles

The two-in two-out rules (called ice-rules) discussed in the previous sections constrain the magnetic moments such that two moments are pointing in and two are pointing out of the tetrahedron (see Fig. 3.1). This magnetic ground state is highly degenerate and every moment satisfies the local two-in two-out constraints. These local constraints may be mapped to a divergence free condition in the fluxes of an emergent field and the coarse-grained description is analogous to that of electromagnetism with defects of the local constraint acting as effective charges [17]. Thus, the system has been called a Coulomb phase. We derive only a few basic results and refer the interested reader for more complete discussions to Refs. [3, 17, 18, 64, 65].

We remind the reader that in the pyrochlore lattice, the centroid of each tetrahedron is a point on the dual diamond lattice. Hence, the midpoints of the bonds of a diamond lattice define the sites of the pyrochlore lattice. Magnetic moments with easy axis anisotropy lie along the bonds of the diamond lattice [11]. On coarse graining, the spin-configurations are mapped to fluxes $\mathbf{B}$ and charges M on the bonds of the diamond lattice via:

$$M = \frac{1}{2}\sum_{a\in\boxtimes}\sigma_a, \tag{3.5}$$

$$\mathbf{B} = \sqrt{\frac{4}{3}}\sum_{a\in\boxtimes}\sigma_a\hat{\mathbf{z}}_a, \tag{3.6}$$

where the sums are over the tetrahedra, denoted by $\boxtimes$. a are the sites in a tetrahedra i.e.

the 4 sublattices and the pre-factors are chosen for convenience.

If the ice-rules are being upheld, the fluxes are conserved at each diamond vertex with two flux lines entering and two exiting it. This leads to a divergence free constraint [17]:

$$\nabla \cdot \mathbf{B}(\mathbf{r}) = 0, \tag{3.7}$$

where $\mathbf{B}(\mathbf{r})$ is the coarse grained $\mathbf{B}$, at longer length scale than the unit cell but shorter than the dimensions of the system and centred at arbitary coordinates $\mathbf{r}$. The Helmholtz free energy then takes the following form [17, 18, 45]:

$$\mathcal{F} = \frac{T\lambda}{2V} \int d^3\mathbf{r} |B(\mathbf{r})|^2, \tag{3.8}$$

where T is the temperature, V is the volume of the unit cell and λ[5] is the stiffness. This has the same form as that of electromagnetism which is why spin ice at low temperatures is said to exist in a Coulomb phase. Eq. (3.8) and Eq. (3.7) imply dipolar correlations ($\propto \nabla_{\mathbf{r}} \nabla_{\mathbf{r}'} \frac{1}{\mathbf{r}-\mathbf{r}'}$; $\mathbf{r}$, $\mathbf{r}'$ are positions of sites) in real space and pinch-points in the momentum space spin-spin correlation function [18, 45]. These pinch-points may be seen in Fig. 3.2 Fig. 3.7(a), Fig. 3.7(b) and Fig. 3.8 and are signatures of the Coulomb phase.

[5]Here λ is the stiffness, as well as connected to the large-N Lagrange multiplier λ. It is worthwhile to mention at this point that in the literature [11, 21, 42], the adjacency matrix is often added/subtracted to a multiple of the identity matrix for ease of computation [21] of correlation functions and solving self consistently for λ. Also one has to put an onsite term to interpret λ as the stiffness of the Coulomb phase of Heisenberg AFM spins on a pyrochlore [11].

3.2.2 Flat bands in the Eigen-spectrum

We start with the AFM Ising model on the pyrochlore lattice, rewriting the Hamiltonian in Eq. (3.3) as:

$$\mathcal{H} = J\sum_{\langle i,j\rangle}\sigma_i\cdot\sigma_j, \tag{3.9}$$

$$= \frac{1}{2}\sum_{i,j,a,b}J_{ij}^{a,b}\sigma_i^a\sigma_j^b. \tag{3.10}$$

Here, the magnitude of J is set to unity ($J=+1$) and $J_{ij}^{a,b}$ is the adjacency matrix. Here i,j are FCC site labels and a,b are sublattice labels. The adjacency matrix (see Appendix A and Appendix A.4) in the nearest neighbor case, in real space, is given by elements 1 if (i,a) and (j,b) are nearest neighbour or 0 if (i,a) and (j,b) represent the same site or are not connected by a single nearest neighbour bond. The factor of $1/2$ is to account for double counting. Fourier transforming the adjacency matrix makes it diagonal in position space with 4×4 sublattice blocks. The Fourier transform of the spins is effected by:

$$\sigma_j^a = \frac{1}{\sqrt{N_{\text{FCC}}}}\sum_{\mathbf{q}\in\text{FBZ}}\sigma^a(\mathbf{q})e^{i\mathbf{q}\cdot\mathbf{R}_i^a}, \tag{3.11}$$

$$\sigma^a(\mathbf{q}) = \frac{1}{\sqrt{N_{\text{FCC}}}}\sum_{j\in a}\sigma_j^a e^{-i\mathbf{q}\cdot\mathbf{R}_i^a}. \tag{3.12}$$

Here, N_{FCC} is the number of spins in each sublattice which is total number of sites in the pyrochlore divided by 4. $\mathbf{R}_i^a$ denotes the location of the moment given by sublattice a and FCC site i. Substituting the Fourier transform Eq. (3.12) into the Hamiltonian

(Eq. (3.10)), we may rewrite the Hamiltonian in Fourier space given by:

$$\mathcal{H} = \sum_{q} \sum_{a,b} J^{ab}(\mathbf{q}) \sigma_a(-\mathbf{q}) \sigma_b(\mathbf{q}). \tag{3.13}$$

Here a, b are the sublattice labels ($a, b \in [1, 2, 3, 4]$) and the Fourier transformed adjacency matrix is obtained by (see Appendix A.4):

$$J^{ab}(\mathbf{q}) = \sum_{ij} J_{ij}^{ab} e^{i\mathbf{q}\cdot(\mathbf{R}_i^a - \mathbf{R}_j^b)}, \tag{3.14}$$

which is a 4×4 matrix in sublattice space and given by:

$$J(\mathbf{q}) = \begin{pmatrix} 0 & 2\cos\left(\frac{q_x+q_y}{4}\right) & 2\cos\left(\frac{q_x+q_z}{4}\right) & 2\cos\left(\frac{q_y+q_z}{4}\right) \\ 2\cos\left(\frac{q_x+q_y}{4}\right) & 0 & 2\cos\left(\frac{q_y-q_z}{4}\right) & 2\cos\left(\frac{q_x-q_z}{4}\right) \\ 2\cos\left(\frac{q_x+q_z}{4}\right) & 2\cos\left(\frac{q_y-q_z}{4}\right) & 0 & 2\cos\left(\frac{q_x-q_y}{4}\right) \\ 2\cos\left(\frac{q_y+q_z}{4}\right) & 2\cos\left(\frac{q_x-q_z}{4}\right) & 2\cos\left(\frac{q_x-q_y}{4}\right) & 0 \end{pmatrix}.$$

Now, we may compute the eigenvalues of $J^{ab}(\mathbf{q})$ using Wolfram Mathematica to obtain:

$$E_{1,2} = -2, \tag{3.15}$$

$$E_{3,4}(\mathbf{q}) = 2 \pm 2\sqrt{G(\mathbf{q})}. \tag{3.16}$$

Here $E_{1,2}$ are $\mathbf{q}$-independent, minimum and dispersionless while $E_{3,4}(\mathbf{q})$ are dispersive bands. $G(\mathbf{q})$ in general is a function of cosines and sines and in general $\mathbf{q}$-dependent. We provide a working expression for $G(\mathbf{q})$ below (see Eq. (3.21)). Following Ref. [42], to

interpret λ as the stiffness of the emergent fields, we add to $J^{ab}(\mathbf{q})$, a constant times the identity:

$$J^{ab}(\mathbf{q}) \to J^{ab}(\mathbf{q}) + 2J\mathbb{I}_{4\times 4}, \tag{3.17}$$

where J is the strength of nearest-neighbour interactions, which is unity for the purposes of this text. This does not change the physics of the model. The eigenvectors of $J^{ab}(\mathbf{q})$ (now, with the constant shift, $J^{ab}(\mathbf{q})$ is referred to as the interaction matrix) are unchanged and the eigenvalues pick up an additive constant. This is seen easily for a general operator $\tilde{O}$ and its normalized eigenvectors $|\epsilon\rangle$ corresponding to eigenvalues ϵ given by:

$$\langle\epsilon|(\tilde{O} + c\mathbb{I}_{4\times 4})|\epsilon\rangle = \epsilon + c, \tag{3.18}$$

where c is an arbitary constant. Similarly, the transformation Eq. (3.17) shifts the eigenvalues of $J^{ab}(\mathbf{q})$. Specifically, the minimum eigenvalues shift from -2 to 0 and are given by:

$$E_{1,2} = 0, \tag{3.19}$$

$$E_{3,4}(\mathbf{q}) = 4 \pm 2\sqrt{G(\mathbf{q})}. \tag{3.20}$$

Here, $G(\mathbf{q})$ is given by the expression:

$$G(\mathbf{q}) = \cos\left(\frac{q_x}{2}\right)\cos\left(\frac{q_y}{2}\right) + \cos\left(\frac{q_x}{2}\right)\cos\left(\frac{q_z}{2}\right) + \cos\left(\frac{q_y}{2}\right)\cos\left(\frac{q_z}{2}\right) + 1. \tag{3.21}$$

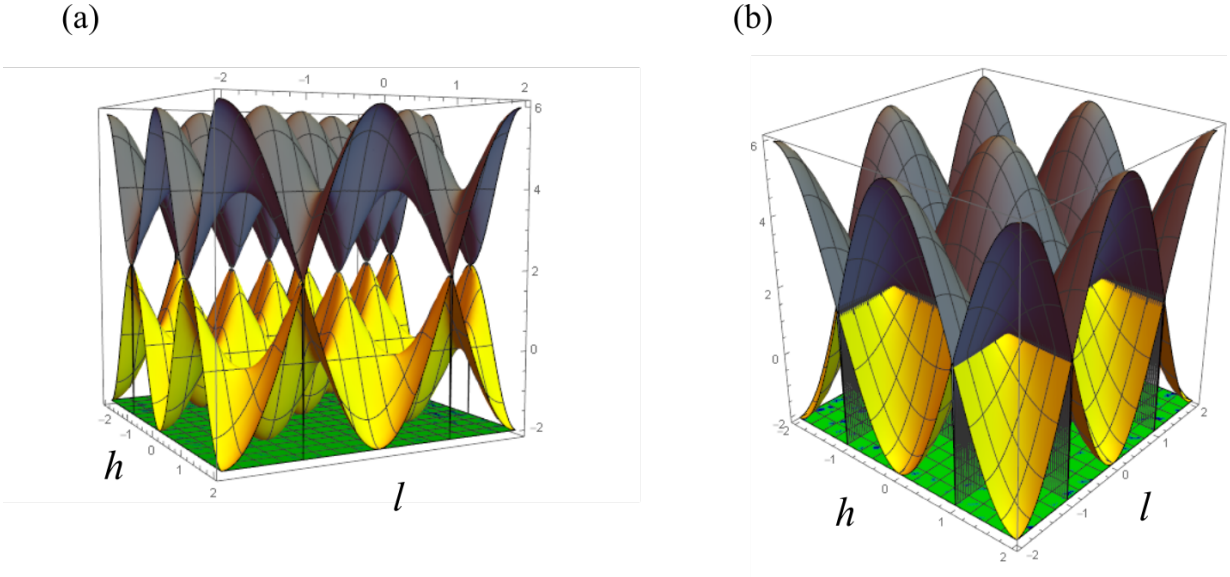

Figure 3.3: Eigenbands (intensity along the z axis) of the nearest neighbour model in reciprocal space in the $(h\,h\,l)$ plane for panel (a) and in $(h\,0\,l)$ plane for panel (b). Both show (2 degenerate) low lying flat bands. The x, y axes are wavevectors in units of $\frac{2\pi}{a}$.

The two eigenvalues in Eq. (3.20), corresponding to $E_{1,2}$ is minimum and 0 for every wavevector $\mathbf{q}$, in the BZ. These are the flat ($\mathbf{q}$-independent) low-lying (2 degenerate) eigenbands shown in Fig. 3.3. One notes that the dispersive bands corresponding to $E_{3,4}$ are always at higher energies and touch the flat bands at $\mathbf{q} = \mathbf{0}$, $\mathbf{q} = \frac{2\pi}{a}[111]$ and other symmetry related points. As we shall see in later sections, this flat band plays a key role in the flat NSF neutron scattering channel in the $[hhl]$ plane for Ising spins on a pyrochlore. First, we consider a special eigenvector of $J^{ab}(\mathbf{q})$ of the form:

$$|P\rangle = \frac{1}{\sqrt{2}}(0, 0, -1, 1). \tag{3.22}$$

This is an eigenvector corresponding to the null eigenvalues $E_{1,2}$ in the $[hhl]$ plane. This eigenvector may be obtained in a brute force fashion from Wolfram Mathematica's analytical schemes and rotating the 2 degenerate eigenvectors corresponding to $E_{1,2}$ appropriately or we can simply motivate it by inspecting the form of the interaction matrix, $J^{ab}(\mathbf{q})$, in the $[hhl]$ plane. This is given by:

$$J^{ab}(hhl) = \begin{pmatrix} 2 & 2\cos\left(\frac{h}{2}\right) & 2\cos\left(\frac{h+l}{4}\right) & 2\cos\left(\frac{h+l}{4}\right) \\ 2\cos\left(\frac{h}{2}\right) & 2 & 2\cos\left(\frac{h-l}{4}\right) & 2\cos\left(\frac{h-l}{4}\right) \\ 2\cos\left(\frac{h+l}{4}\right) & 2\cos\left(\frac{h-l}{4}\right) & \mathbf{2} & \mathbf{2} \\ 2\cos\left(\frac{h+l}{4}\right) & 2\cos\left(\frac{h-l}{4}\right) & \mathbf{2} & \mathbf{2}. \end{pmatrix} \tag{3.23}$$

Note that the column 3 and 4 as well as row 3 and 4 are exactly equal with a shared sub-block composed of the same number 2. This is shown in red. Here $q_x = q_y = h$ and $q_z = l$. The form of the above matrix implies trivially that $|P\rangle$ is an eigenvector of $J^{ab}(hhl)$, i.e. :

$$\langle P|J^{ab}(hhl)|P\rangle = 0. \tag{3.24}$$

Thus, we have established $|P\rangle$ as an eigenvector of the interaction matrix in the $[hhl]$ plane corresponding to the flat eigenvalues. We shall see in the next section how this eigenvector pops back up on considering the geometrical properties of the pyrochlore and polarized neutron scattering. We further noted that displacing any one sublattice in a tetrahedron by a small number δ', destroys the tetrahedral symmetry and dispersion arises in one of the flat bands. This further shows that flat bands are connected to the geometry of the pyrochlore.

3.2.3 Geometrical Insight into Polarized Neutron Scattering

The total energy-integrated magnetic scattering cross-section was obtained in Eq. (2.15) as:

$$\frac{d\sigma(\mathbf{Q})}{d\Omega} = \frac{C[\mathcal{F}(\mathbf{Q})]^2}{N_{\text{FCC}}} \sum_{i,j} \sum_{a,b} \langle \mu^a_{i\perp} \cdot \mu^b_{j\perp} \rangle e^{\mathrm{i}\mathbf{Q}\cdot\mathbf{R}^{ab}_{ij}}. \tag{3.25}$$

Here C is a constant, Ω the solid angle, $\mathcal{F}(\mathbf{Q})$ is magnetic form factor for the probed magnetic ions and $\mathbf{Q}$ is the momentum transfer between the initial and final neutron momenta. $\mathbf{Q} = \mathbf{G} + \mathbf{q}_{\text{BZ}}$, where $\mathbf{q}_{\text{BZ}}$ lies in the FBZ of the FCC lattice (see Appendix A.2) and $\mathbf{G}$ are FCC reciprocal lattice vectors. Here $\mu^a_{i\perp}$ [6] represents the magnetic moment at FCC site i and sublattice a. The $\perp$ represents the fact that the neutrons are only able to probe moments perpendicular to the the neutron momentum transfer $\mathbf{Q}$ (see Sec. 2.1). This implies:

$$\mu^a_{i\perp} = \mu^a_i - (\mu^a_i \cdot \mathbf{Q})\mathbf{Q}/|\mathbf{Q}|^2. \tag{3.26}$$

The magnetic moment μ^a_i is composed of the spin, the g-factor and the Bohr magneton μ_{B}. The g-factor is in general a site dependent tensor which connects the microscopic spins $\mathbf{S}$ to magnetic moments (interacting with the neutron):

$$\mu^\eta_i = \mu_{\text{B}} \sum_\nu g^{\eta\nu} S^\nu_i, \tag{3.27}$$

[6] Here, μ_i and $\mu^a_{i\perp}$ are vectors and should be boldfaced.

where the η, ν are spin-components, i represents the lattice sites. For Ising spins σ_i constrained along the local easy axes this simplifies as:

$$\mu_i^a = (g_z \mu_B) \sigma_i^a \hat{\mathbf{z}}^a. \tag{3.28}$$

We absorb the factor $(g_z \mu_B)$ in the constant in the expression Eq. (3.25) and Eq. (3.26) reduces to :

$$\sigma_{i\perp}^a \text{ [7]} = \sigma_i^a \hat{\mathbf{z}}^a - (\sigma_i^a \hat{\mathbf{z}}^a \cdot \mathbf{Q})\mathbf{Q}/|\mathbf{Q}|^2. \tag{3.29}$$

One may substitute the above in Eq. (3.25) and work out the trigonometric identities to separate out the NSF and the SF channel contributions. A more intuitive picture is obtained by considering Eq. (3.29). The first term on the right is the original vector along $\hat{\mathbf{z}}^a$ and the second term subtracts the projection of $\hat{\mathbf{z}}^a$ along $\hat{\mathbf{Q}}$ from the original vector. Then, one is left with the entirety of the original vector $\sigma_i^a \hat{\mathbf{z}}^a$ projected in the plane perpendicular to $\hat{\mathbf{Q}}$. This plane may be decomposed into two axes along the neutron polarization $\hat{\mathbf{P}}$ and perpendicular to both $\hat{\mathbf{P}}$ and $\hat{\mathbf{Q}}$, call it $\hat{\mathbf{R}}$ (see Fig. 3.4).

Thus, the spin vectors may be written as components along the orthogonal 3D axes $\hat{\mathbf{P}}$, $\hat{\mathbf{Q}}$ and $\hat{\mathbf{R}}$. As discussed (in Sec. 2.1), if the neutron polarization direction is parallel/anti-parallel to the direction of the local magnetic moment probed in the system, the spin of the incoming and outgoing neutron remains unchanged, which is the non-spin flip (NSF) channel. However, if the neutron polarization is perpendicular to the alignment of the local magnetic moment probed, the spin of the neutron will flip and this is called the spin flip (SF) channel.

[7] $\sigma_{i\perp}^a$ is a vector and should be boldfaced.

So, summarizing, the local magnetic moment in the sample may be aligned in any direction and have components projected along axes $\hat{\mathbf{P}}$, $\hat{\mathbf{Q}}$ and $\hat{\mathbf{R}}$. The incoming neutron polarization is along $\hat{\mathbf{P}}$. All contributions to the neutron scattering from magnetic moments along $\hat{\mathbf{Q}}$ are not probed. Magnetic moments along $\hat{\mathbf{P}}$ do **not** flip the spins of the incoming neutrons while magnetic moments along $\hat{\mathbf{R}}$ flip the spin of the neutrons. By separating the neutron scattering contributions along $\hat{\mathbf{P}}$ and $\hat{\mathbf{R}}$, we effectively separate the SF and NSF channel. By considering the sum of contributions along $\hat{\mathbf{P}}$ and $\hat{\mathbf{R}}$, we obtain the total neutron scattering given by the expression in Eq. (3.25). From here on forth, we shall replace $\hat{\mathbf{P}}$ by $\hat{\mathbf{z}}_{\mathrm{NSF}}$ and $\hat{\mathbf{R}}$ by $\hat{\mathbf{z}}_{\mathrm{SF}}$. This implies that Eq. (3.29) can be rewritten as as vector projected along $\hat{\mathbf{z}}_{\mathrm{NSF}}$ and $\hat{\mathbf{z}}_{\mathrm{SF}}$, which is given by:

$$\sigma^a_{i\perp} = \sigma^a_i(\hat{\mathbf{z}}^a \cdot \hat{\mathbf{z}}_{\mathrm{NSF}})\hat{\mathbf{z}}_{\mathrm{NSF}} + \sigma^a_i(\hat{\mathbf{z}}^a \cdot \hat{\mathbf{z}}_{\mathrm{SF}})\hat{\mathbf{z}}_{\mathrm{SF}}. \tag{3.30}$$

The expectation value in Eq. (3.25) may be re-expressed as:

$$\langle \mu^a_{i\perp} \cdot \mu^b_{j\perp} \rangle = (g_z\mu_B)^2 \langle \sigma^a_{i\perp} \cdot \sigma^b_{j\perp} \rangle. \tag{3.31}$$

The factor $(g_z\mu_B)^2$ is absorbed into the constant upfront of Eq. (3.25) and the expression for the dot product using Eq. (3.30):

$$\langle \sigma^a_{i\perp} \cdot \sigma^b_{j\perp} \rangle = \langle \sigma^a_i \sigma^b_j \rangle (\hat{\mathbf{z}}^a \cdot \hat{\mathbf{z}}_{\mathrm{NSF}})(\hat{\mathbf{z}}^b \cdot \hat{\mathbf{z}}_{\mathrm{NSF}}) + \langle \sigma^a_i \sigma^b_j \rangle (\hat{\mathbf{z}}^a \cdot \hat{\mathbf{z}}_{\mathrm{SF}})(\hat{\mathbf{z}}^b \cdot \hat{\mathbf{z}}_{\mathrm{SF}}). \tag{3.32}$$

Using Eq. (3.32) and Eq. (3.25), we rewrite the channel-separated total neutron scat-

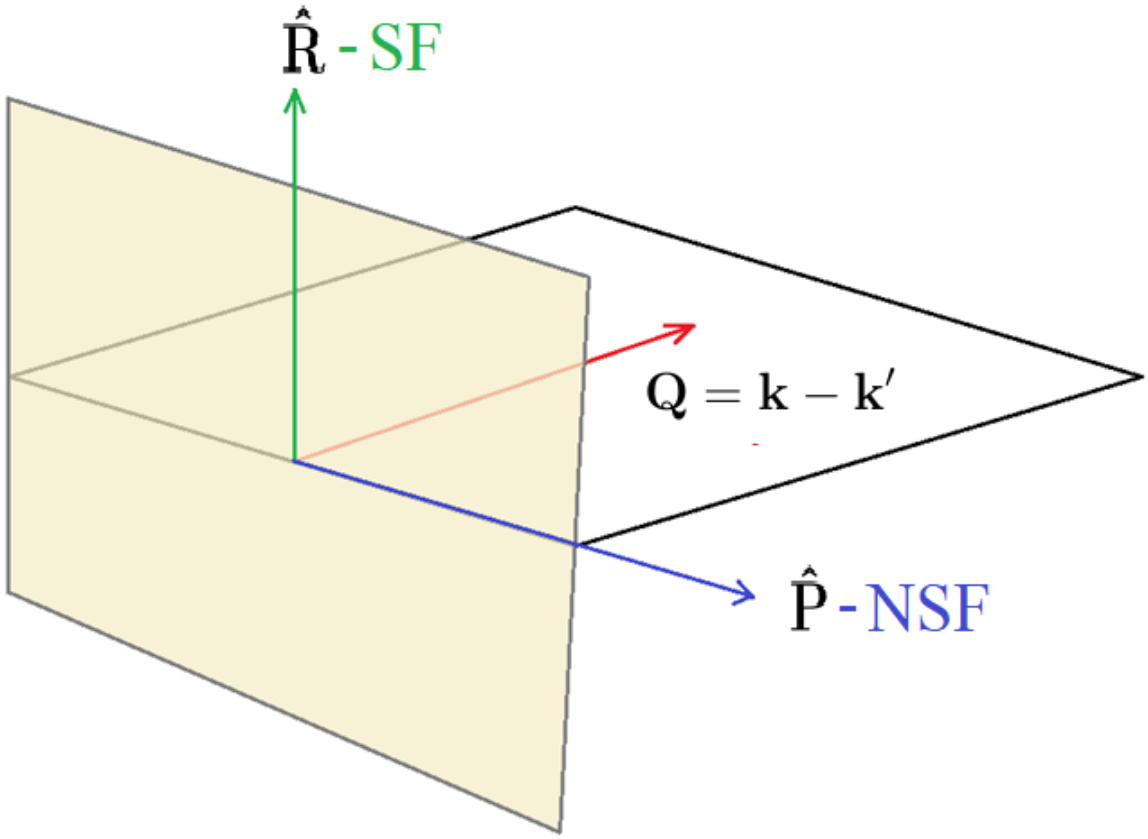

Figure 3.4: Figure shows the geometry of polarized neutron scattering when the neutron polarization is along $\hat{\mathbf{P}}$ which is $\hat{\mathbf{z}}_{\mathrm{NSF}}$ in this case. $\mathbf{Q}$ is the momentum transfer given by the difference of initial and final neutron momenta ($\mathbf{k}$, $\mathbf{k}'$ respectively). Magnetic moments along $\hat{\mathbf{Q}}$ will not contribute to the scattering. Only magnetic moments along $\hat{\mathbf{P}}$ will contribute to the non-spin flip (NSF) channel. Magnetic moments along $\hat{\mathbf{R}} = \hat{\mathbf{P}} \times \hat{\mathbf{Q}}$ will contribute to the spin-flip channel (SF) and is $\hat{\mathbf{z}}_{\mathrm{SF}}$ in this case. If contributions along $\hat{\mathbf{P}}$ and $\hat{\mathbf{R}}$ are not resolved (but are just added), we obtain the total (elastic) magnetic neutron scattering.

tering cross-section (elastic) where all the constants are absorbed in C:

$$\frac{d\sigma(\mathbf{Q})}{d\Omega} = C\left(\sum_a\sum_b \langle\sigma^a(-\mathbf{Q})\sigma^b(\mathbf{Q})\rangle(\hat{\mathbf{z}}^a\cdot\hat{\mathbf{z}}_{\mathrm{NSF}})(\hat{\mathbf{z}}^b\cdot\hat{\mathbf{z}}_{\mathrm{NSF}})\right) + \left(\sum_a\sum_b \langle\sigma^a(-\mathbf{Q})\sigma^b(\mathbf{Q})\rangle(\hat{\mathbf{z}}^a\cdot\hat{\mathbf{z}}_{\mathrm{SF}})(\hat{\mathbf{z}}^b\cdot\hat{\mathbf{z}}_{\mathrm{SF}})\right). \quad (3.33)$$

Here the NSF channel may be separated easily and is given by the expression:

$$\frac{d\sigma(\mathbf{Q})}{d\Omega}|_{\mathrm{NSF}} = C\left(\sum_a\sum_b \langle\sigma^a(-\mathbf{Q})\sigma^b(\mathbf{Q})\rangle(\hat{\mathbf{z}}^a\cdot\hat{\mathbf{z}}_{\mathrm{NSF}})(\hat{\mathbf{z}}^b\cdot\hat{\mathbf{z}}_{\mathrm{NSF}})\right). \quad (3.34)$$

In the experiment conducted by Fennel *et al.* (Ref. [19]), the neutron polarization direction chosen is given by $\mathbf{P}_{\mathrm{Fennel}} = [1\bar{1}0]$, $\mathbf{Q}_{\mathrm{Fennel}} = [hhl]$ and $\mathbf{R}_{\mathrm{Fennel}} = \mathbf{P}_{\mathrm{Fennel}} \times \mathbf{Q}_{\mathrm{Fennel}}$. As discussed before, magnetic moments along $\hat{\mathbf{P}}_{\mathrm{Fennel}}$ (denoted as $\hat{\mathbf{z}}_{\mathrm{NSF}}$ hereon) lead to non-spin flip scattering (NSF) contribution and moments along $\hat{\mathbf{R}}_{\mathrm{Fennel}}$ (denoted by $\hat{\mathbf{z}}_{\mathrm{SF}}$) lead to a contribution to the spin flip (SF) channel. Studying the projector $(\hat{\mathbf{z}}^a\cdot\hat{\mathbf{z}}_{\mathrm{NSF}})$, which is a 4×1 row vector, we find:

$$(\hat{\mathbf{z}}^a\cdot\hat{\mathbf{z}}_{\mathrm{NSF}}) = \begin{cases} \pm\sqrt{2/3} & \text{if } a\equiv 3,4 \\ 0 & \text{if } a\equiv 1,2 \end{cases}. \quad (3.35)$$

Here, a are the sublattice labels. We see that only 2 of the four sublattices (labelled by $3,4$ in our sublattice conventions. See Appendix A for sublattice conventions) in a tetrahedron contribute to the NSF scattering. This was noted by Fennel *et al.* in the appendix of their

2009 Science paper [19]. Denoting the projector $(\hat{\mathbf{z}}^a \cdot \hat{\mathbf{z}}_{\rm NSF})$ as P^a, we see:

$$P^a = (\hat{\mathbf{z}}^a \cdot \hat{\mathbf{z}}_{\rm NSF}) = \sqrt{\frac{2}{3}}(0, 0, -1, +1). \tag{3.36}$$

We see that the neutron projector for the NSF channel in the (hhl) plane P^a, for two sublattices $(a = 1, 2)$, is null. These two sublattices do not contribute to the NSF channel in the (hhl) plane. Rewriting Eq. (3.34) with the projector P^a, we obtain:

$$\frac{d\sigma(\mathbf{Q})}{d\Omega}|_{\rm NSF} = C\left(\sum_a \sum_b P^a \langle \sigma^a(-\mathbf{Q})\sigma^b(\mathbf{Q})\rangle P^b\right). \tag{3.37}$$

The projector P^a contains the information about the geometry of the arrangements of spins (along local easy axes $\hat{\mathbf{z}}^a$) as well as the neutron polarization directions $\hat{\mathbf{z}}_{\rm NSF}$. Thus, the 16 term sum in Eq. (3.37) reduces to just 4 terms because of purely geometric reasons. Only $a, b \equiv 3, 4$ sublattices (see Fig. A.1 and Appendix A for sublattice conventions) contribute and Eq. (3.37) reduces to just the sums over these sublattices, giving:

$$\frac{d\sigma(\mathbf{Q})}{d\Omega}|_{\rm NSF} = \frac{2}{3}(\langle \sigma^4(-\mathbf{Q})\sigma^4(\mathbf{Q})\rangle + \langle \sigma^3(-\mathbf{Q})\sigma^3(\mathbf{Q})\rangle - \langle \sigma^4(-\mathbf{Q})\sigma^3(\mathbf{Q})\rangle - \langle \sigma^3(-\mathbf{Q})\sigma^4(\mathbf{Q})\rangle), \tag{3.38}$$

where the constants up-front are implicit. Since all lattice points are equivalent in the paramagnetic regime [8], $\langle \sigma^4(-\mathbf{Q})\sigma^4(\mathbf{Q})\rangle = \langle \sigma^3(-\mathbf{Q})\sigma^3(\mathbf{Q})\rangle$ and $\langle \sigma^4(-\mathbf{Q})\sigma^3(\mathbf{Q})\rangle = \langle \sigma^3(-\mathbf{Q})\sigma^4(\mathbf{Q})\rangle$,

[8] For temperatures above the transition, no symmetry is broken and all lattice points are equivalent. For the large-N case, the model always remains paramagnetic [11] and no symmetry is broken above the large-N instability, below which λ, the lagrange multiplier cannot be found.

this reduces Eq. (3.38) further :

$$\frac{d\sigma(\mathbf{Q})}{d\Omega}|_{\text{NSF}} = \frac{4}{3}(\langle\sigma^3(-\mathbf{Q})\sigma^3(\mathbf{Q})\rangle - \langle\sigma^3(-\mathbf{Q})\sigma^4(\mathbf{Q})\rangle \tag{3.39}$$

Eq. (3.39) shows explicitly how NSF channel contributions come solely from sublattices 3 and 4. Thus, only chains of spins corresponding to $3, 4$ sublattices contribute, which are the so called α-chains (see Fig. 3.5 and Fig. A.1). Incidentally, the α-chains extend parallel to the neutron polarization $\hat{\mathbf{z}}_{\text{NSF}}$ (see Fig. 3.5) :

$$\mathbf{r}^3 - \mathbf{r}^4 = \frac{1}{4}(1, -1, 0) \propto \hat{\mathbf{z}}_{\text{NSF}}. \tag{3.40}$$

Here, $\mathbf{r^3}$ and $\mathbf{r^4}$ are the positions of sublattice 3 and 4. However, this does not shed light as to why the NSF scattering is $\mathbf{Q}$-independent. In general, the Fourier transformed correlation fuctions in Eq. (3.39) should be different and dependent on $\mathbf{Q}$ and it is unclear how the two correlation functions conspire to yeild a flat NSF. The careful reader might note that the vector form of the projector P^a (Eq. (3.49)) is proportional to the special eigenvector $|P\rangle$ (Eq. (3.22)) of the interaction matrix $J^{ab}(\mathbf{Q})$ upto a multiplicative constant. This equivalence is the key insight which will help us connect flat NSF to the flat bands as discussed in the next section.

In this section, we discussed some preliminary results regarding polarized magnetic neutron scattering and saw how only the α-chains contribute to the scattering intensity in the NSF channel. In the next sections, we develop the key results and findings of this project.

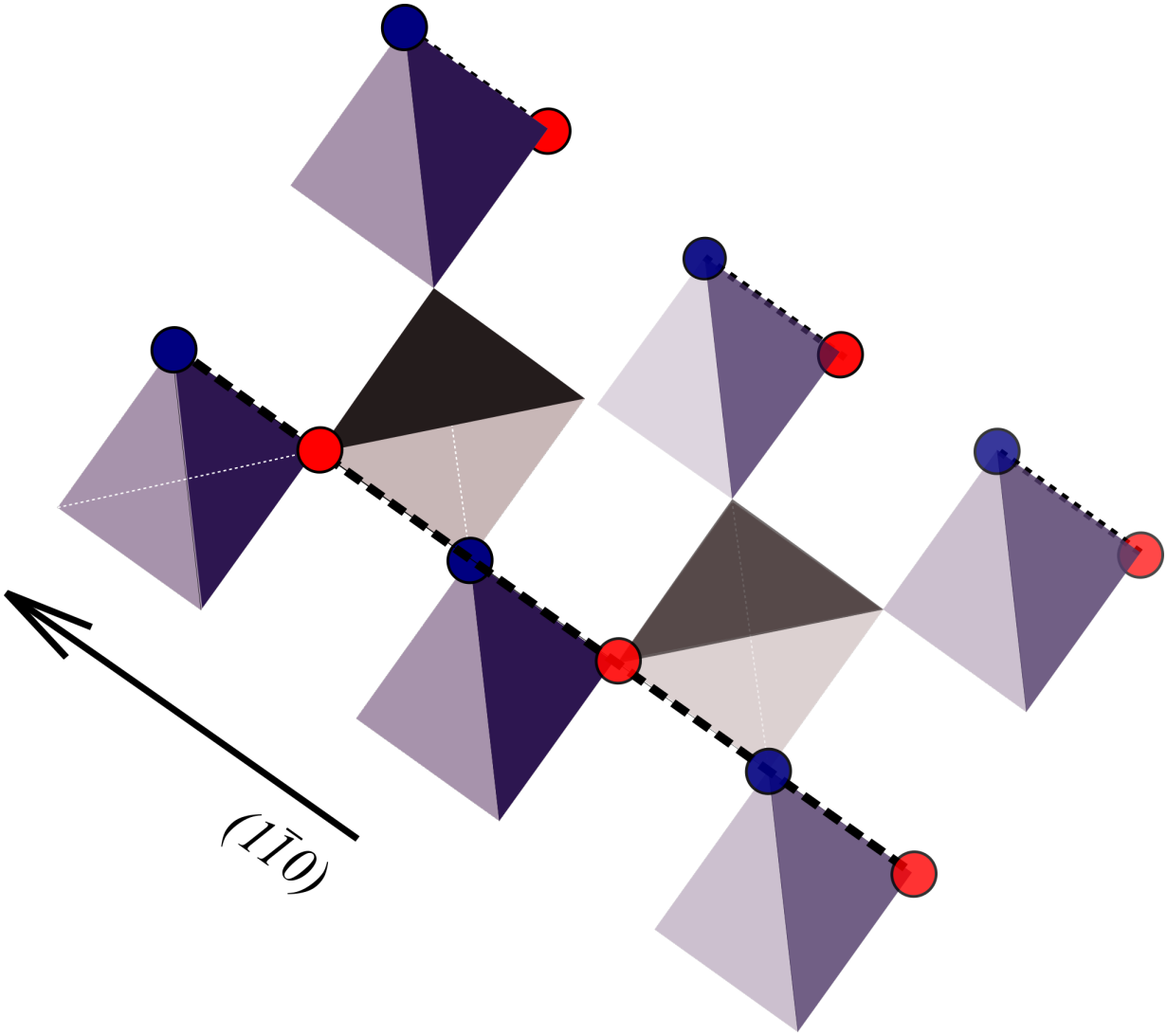

Figure 3.5: The geometry of the polarized neutron scattering is such that only two sublattices of the tetrahedron (sublattices 3 and 4 in our convention, showed as blue and red spheres, see Appendix A for sublattice convention) contribute to the NSF channel scattering. These form chains in the lattice and are called α-chains in this thesis. The α-chains extend in both directions and parallel α-chains may be reached by hopping over two bonds in any direction starting on either sublattice 3 or 4. Further, the direction of the α-chain happens to be parallel to the neutron polarization direction $\hat{\mathbf{z}}_{\mathrm{NSF}}$ in the experiment done by Fennel *et al*. in Ref. [19]. Also see Fig. A.1

3.3 Key Results

3.3.1 Flat Bands to flat NSF

We saw in previous sections how the interaction matrix $J^{ab}(\mathbf{q})$, hosts two degenerate flat eigenbands and one of the eigenvectors $|P\rangle$ (Eq. (3.22)) (in the $[hhl]$ plane!) corresponding to the $\mathbf{q}$-independent eigenvalues is proportional (upto some multiplicative constant) to the neutron scattering projector P^a (Eq. (3.49)) for the NSF channel. This projector encodes the information of the α-chains (see Fig. 3.5) and of the alignment of the spins (the easy axis anisotropy in this case) projected onto the polarization direction of the incoming neutron spin. We rewrite for convenience:

$$(\hat{\mathbf{z}}^a \cdot \hat{\mathbf{z}}_{\text{NSF}}) = P^a \propto |P\rangle \propto (0, 0, -1, +1). \tag{3.41}$$

For the rest of this chapter, we utilize the large-N approximation (Eq. (2.68)) and compute the spin-spin correlation functions [15] which are given by (see Eq. (2.67)) :

$$\langle \sigma^a(-\mathbf{Q})\sigma^b(\mathbf{Q})\rangle = (\lambda \mathbb{I}_{4\times 4} + \beta J(\mathbf{Q}))^{-1}_{ab}. \tag{3.42}$$

Here, λ (temperature dependent quantity) is found self-consistently from the spin length constraint and β is the inverse temperature. $\mathbf{Q}$ and $\mathbf{q}$ are used interchangeably and refer to all possible wavevectors. Using the interaction matrices with constant diagonal shits (Eq. (3.17)), λ is interpreted as the stiffness of the Coulomb phase [11]. The expression

for the polarized neutron scattering (Eq. (3.37)) for the NSF channel is given by:

$$\left.\frac{d\sigma(\mathbf{Q})}{d\Omega}\right|_{\text{NSF}} = C\left(\sum_a\sum_b P^a\langle\sigma^a(-\mathbf{Q})\sigma^b(\mathbf{Q})\rangle P^b\right). \tag{3.43}$$

Ignoring the constant upfront and substituting Eq. (3.42) in the above we obtain:

$$\left.\frac{d\sigma(\mathbf{Q})}{d\Omega}\right|_{\text{NSF}} = \sum_a\sum_b P^a(\lambda\mathbb{I}_{4\times4} + \beta J(\mathbf{Q}))^{-1}_{ab}P^b. \tag{3.44}$$

We noted before how $|P\rangle \propto P^a$ and is the eigenvector for the flat band in the (hhl) plane. We refer to the neutron projector P^a as P or $|P\rangle$ for the remainder of the presentation. The eigenvectors do not change on addition of a multiple of the identity, mutiplying a constant to the matrix and inverting it. This is seen easily for a general operator $\tilde{O}$ and its normalized eigenvectors $|\epsilon\rangle$ corresponding to eigenvalues ϵ:

$$\langle\epsilon|\beta\tilde{O}|\epsilon\rangle = \epsilon\beta, \tag{3.45}$$

$$\langle\epsilon|(\beta\tilde{O} + c\mathbb{I}_{4\text{x}4})|\epsilon\rangle = \beta\epsilon + c, \tag{3.46}$$

$$\langle\epsilon|(\beta\tilde{O} + c\mathbb{I}_{4\text{x}4})^{-1}|\epsilon\rangle = (\beta\epsilon + c)^{-1}. \tag{3.47}$$

The same follows for the correlation matrix $\mathcal{M}^{-1}_{ab} = (\lambda\mathbb{I}_{4\times4} + \beta J(\mathbf{Q}))^{-1}_{ab}$ and Eq. (3.44) which is written in matrix multiplication form:

$$\left.\frac{d\sigma(\mathbf{Q})}{d\Omega}\right|_{\text{NSF}} = P(\mathcal{M})^{-1}P^T. \tag{3.48}$$

where P is the projector for the neutron scattering and is proportional to the eigenvector of the flat bands. P is given by:

$$P = \sqrt{\frac{2}{3}}(0, 0, -1, +1). \tag{3.49}$$

In the $[hhl]$ plane, sandwiching the interaction matrix $J_{ab}(hhl)$ between the neutron projectors:

$$\begin{aligned} \langle P|J(hhl)|P\rangle &= 0, & (3.50)\\ \langle P|\beta J(hhl)|P\rangle &= 0, & (3.51)\\ \langle P|\lambda \mathbb{I}_{4\times 4} + \beta J(hhl)|P\rangle &= \frac{4\lambda}{3}. & (3.52) \end{aligned}$$

This yields our final result for the flat NSF, as described in the large-N approximation:

$$\left.\frac{d\sigma(\mathbf{Q})}{d\Omega}\right|_{\text{NSF}} = P(\mathcal{M})^{-1}P^T = \frac{4}{3\lambda}. \tag{3.53}$$

Thus, we see that the NSF channel of the polarized neutron scattering (in the $[hhl]$) plane effectively projects the flat bands of the interaction matrix $J(\mathbf{Q})$ and results in a flat NSF. This happens since only spins in the α-chain contribute.

3.3.2 Measuring the emergent field

We found that the NSF channel intensity is $\mathbf{Q}$-independent and given by $\frac{4}{3\lambda}$ where λ is computed self-consistently from the spin length constraint in Eq. (2.70). In the large-

N approximation, utilizing Eq. (3.17), λ is interpreted as the stiffness of the Coulomb phase [11]. To clarify what the neutron scattering is picking up, we transform the neutron scattering expression:

$$\frac{d\sigma(\mathbf{Q})}{d\Omega} = C\left(\sum_a \sum_b \langle \sigma^a(-\mathbf{Q})\sigma^b(\mathbf{Q})\rangle \left[(\hat{\mathbf{z}}^a \cdot \hat{\mathbf{z}}_{\mathrm{NSF}})(\hat{\mathbf{z}}^b \cdot \hat{\mathbf{z}}_{\mathrm{NSF}}) + (\hat{\mathbf{z}}^a \cdot \hat{\mathbf{z}}_{\mathrm{SF}})(\hat{\mathbf{z}}^b \cdot \hat{\mathbf{z}}_{\mathrm{SF}})\right]\right), \tag{3.54}$$

to the flux/charge picture using the transformation (see Eq. (3.6)):

$$M(\mathbf{Q}) = \frac{1}{2}\sum_{a\in\boxtimes} \sigma_a(\mathbf{Q}), \tag{3.55}$$

$$\mathbf{B}(\mathbf{Q}) = \sqrt{\frac{4}{3}}\sum_{a\in\boxtimes} \sigma_a(\mathbf{Q})\hat{\mathbf{z}}_a. \tag{3.56}$$

We obtain:

$$\left.\frac{d\sigma(\mathbf{Q})}{d\Omega}\right|_{\mathrm{NSF}} = \frac{4}{3}\left\langle |\mathbf{B}(\mathbf{Q})\cdot\hat{\mathbf{z}}_{\mathrm{NSF}}|^2\right\rangle, \tag{3.57}$$

$$\left.\frac{d\sigma(\mathbf{Q})}{d\Omega}\right|_{\mathrm{SF}} = \frac{4}{3}\left\langle |\mathbf{B}(\mathbf{Q})\cdot\hat{\mathbf{z}}_{\mathrm{SF}}|^2\right\rangle. \tag{3.58}$$

So, we see here clearly, the NSF and SF channels are probing the correlations between the emergent fluxes along $\hat{\mathbf{z}}_{\mathrm{NSF}}$ and $\hat{\mathbf{z}}_{\mathrm{SF}}$ directions respectively. Thus, in this subsection, the magnetic neutron scattering is shown to effectively probe the correlations between the emergent fluxes in this system. In the next subsection, we shall study the effects of further-neighbour interactions in this model.

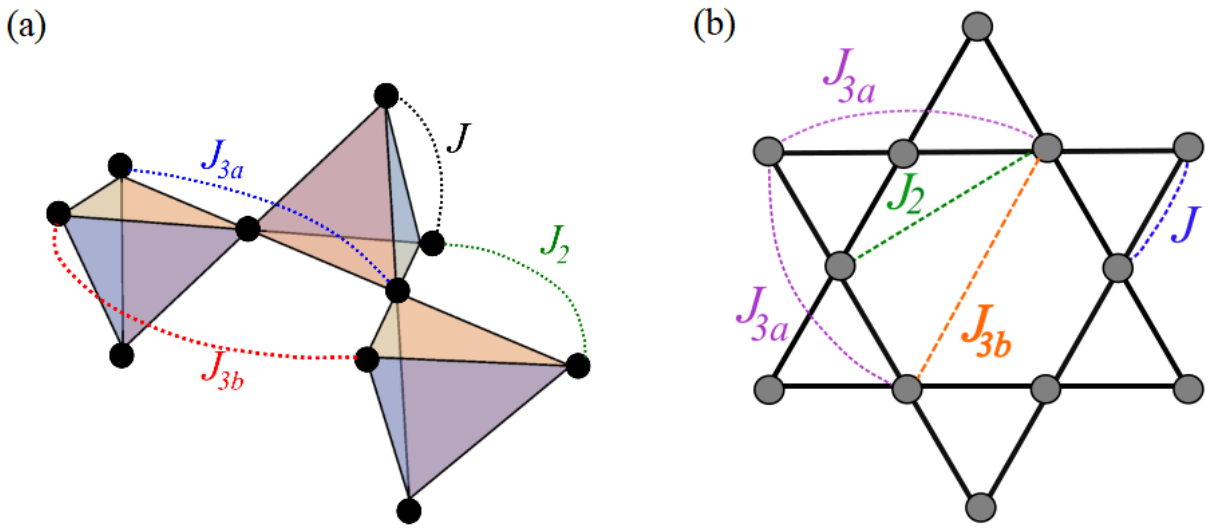

Figure 3.6: Figures show further-neighbour couplings on the pyrochlore lattice. Panel (b) is the kagomé layer slice of the pyrochlore lattice perpendicular to $\langle 111 \rangle$ direction.

3.3.3 Extended spin ice and effect of further-neighbour interactions.

In this subsection, we consider the effect of further-neighbor interactions. In general, further-neighbour interactions will perturb the ground-state degeneracy which manifests as flat eigenbands of the interaction matrix $J(\mathbf{q})$. Consequently, the NSF scattering is expected to be dispersive. The Hamiltonian is given by:

$$\mathcal{H} = \sum_{q} \sum_{a,b} J_{ab}(\mathbf{q}) \sigma_a(-\mathbf{q}) \sigma_b(\mathbf{q}), \tag{3.59}$$

where the adjacency matrix $J(\mathbf{q})$ includes further-neighbor exchange:

$$J_{ab}(\mathbf{q}) = J(A_{ab}(\mathbf{q}) + \frac{J_2}{J} C_{ab}(\mathbf{q}) + \frac{J_{3a}}{J} D_{ab}(\mathbf{q}) + \frac{J_{3b}}{J} E_{ab}(\mathbf{q})). \tag{3.60}$$

Here, J is the interaction strength for nearest-neighbour couplings and A_{ab} is the nearest-neigbour adjacency matrix. J_2, J_{3a} and J_{3b} refer to the magnitude of further-neighbour exchange corresponding to the 2nd nearest neighbour and two inequivalent further-neighbour couplings. $C_{ab}(\mathbf{q})$, $D_{ab}(\mathbf{q})$, $E_{ab}(\mathbf{q})$[9] are their Fourier transformed adjacency matrices (see Appendix A.4).

We saw before, how $A_{ab}(\mathbf{q})$ (referred to as $J_{ab}(\mathbf{q})$ in previous sections) has an eigenvector $|P\rangle$ corresponding to flat eigenvalues in the $[hhl]$ plane. Arbitary choices of the coupling strengths perturb this flat-eigenband and lead to dispersive eigenmodes. However, a special case is obtained when $J_2 = J_{3a} \equiv J'$ and $J_{3b} = 0$. For $-0.5 < J' < 0.25$, it was noted that the spin ice ground state with spins following the ice-rules is maintained [63]. This has been called extended spin ice (ESI) in the literature and we refer the interested reader to Refs. [46, 63, 66] for further details and discussions. Considering the ESI case and following Refs. [21, 42] we shift the adjacency matrices (optional step):

$$J'C^{ab}(\mathbf{q}) \to J'C^{ab}(\mathbf{q}) + 4J'\mathbb{I}_{4\text{x}4}, \tag{3.61}$$

$$J'D^{ab}(\mathbf{q}) \to J'D^{ab}(\mathbf{q}) - 6J'\mathbb{I}_{4\text{x}4}. \tag{3.62}$$

Now, the new matrices with constant shifts are referred to as the interaction matrices[10] (following Ref. [11]). In the $[hhl]$ plane, the further-neigbour matrices $J'C_{ab}(hhl) + J'D_{ab}(hhl)$

[9] To keep names of adjacency matrices consistent, we term the nearest-neighbour exchange $A_{ab}(\mathbf{q})$, we reserve $B_{ab}(\mathbf{q})$ for the breathing pyrochlore case with two inequivalent nearest-neighbour couplings (see Chap. 4). We term the further-neighbour adjacency matrices in order as $C_{ab}(\mathbf{q})$, $D_{ab}(\mathbf{q})$, $E_{ab}(\mathbf{q})$ corresponding to the second nearest-neighbour coupling J_2 and the two inequivalent third neighbour couplings J_{3a} and J_{3b}. Finally, simply $J_{ab}(\mathbf{q})$ is the full adjacency matrix with both nearest-neighbour and further-neighbour exchange given in Eq. (3.60)

[10] Before the constant shift is added we have the usual adjacency matrices. After the constant shift is added we call these new matrices the interaction matrices [11].

together have the same form as in Eq. (3.23), namely the 3, 4 sublattice sub-block having the same elements given by:

$$\begin{pmatrix} 2\left(2C\left(\frac{h+l}{2}\right)+C(h)-1\right) & 4C\left(\frac{l}{2}\right) & 4C\left(\frac{h}{2}\right)C\left(\frac{h-l}{4}\right) & 4C\left(\frac{h}{2}\right)C\left(\frac{h-l}{4}\right) \\ 4C\left(\frac{l}{2}\right) & 2\left(2C\left(\frac{h-l}{2}\right)+C(h)-1\right) & 4C\left(\frac{h}{2}\right)C\left(\frac{h+l}{4}\right) & 4C\left(\frac{h}{2}\right)C\left(\frac{h+l}{4}\right) \\ 4C\left(\frac{h}{2}\right)C\left(\frac{h-l}{4}\right) & 4C\left(\frac{h}{2}\right)C\left(\frac{h+l}{4}\right) & 4C\left(\frac{h}{2}\right)C\left(\frac{l}{2}\right) & 4C\left(\frac{h}{2}\right)C\left(\frac{l}{2}\right) \\ 4C\left(\frac{h}{2}\right)C\left(\frac{h-l}{4}\right) & 4C\left(\frac{h}{2}\right)C\left(\frac{h+l}{4}\right) & 4C\left(\frac{h}{2}\right)C\left(\frac{l}{2}\right) & 4C\left(\frac{h}{2}\right)C\left(\frac{l}{2}\right) \end{pmatrix} \tag{3.63}$$

Here the C refers to the cosine function. It is readily seen that the NSF projector $|P\rangle \propto (0,0,-1,1)$, is also an eigenvector of above matrix with 0 eigenvalue. Thus we see that each term in the interaction matrix:

$$J_{ab}(\mathbf{q}) = J(A_{ab}(\mathbf{q}) + \frac{J'}{J}C_{ab}(\mathbf{q}) + \frac{J'}{J}D_{ab}(\mathbf{q})), \tag{3.64}$$

with $\mathbf{q} \in [hhl]$, share the same eigenvector $|P\rangle$ corresponding to flat eigenvalues. Thus, $\mathcal{M}^{-1}_{ab} = (\lambda \mathbb{I}_{4\times 4} + \beta J(\mathbf{Q}))^{-1}_{ab}$ will also have the same eigenvector $|P\rangle$. For the NSF neutron scattering Eq. (3.48) we then have:

$$\frac{d\sigma(\mathbf{Q})}{d\Omega}|_{\text{NSF}} = P(\mathcal{M})^{-1}P^T = \frac{4}{3\lambda}. \tag{3.65}$$

Thus, the NSF channel scattering for the ESI case is also $\mathbf{q}$-independent. The above analysis works out in a similar fashion for Ising spins (constrained along the local easy axis) on a breathing pyrochlore (see Appendix A.3) by inspecting the interaction matrices (provided in Appendix A.4) in the $[hhl]$ plane. The ESI result may also be deduced from the

fact that the matrix given by $C_{ab}(\mathbf{q}) + D_{ab}(\mathbf{q})$ can be written as a polynomial of $A_{ab}(\mathbf{q})$ and will share eigenvectors (see appendices of Ref. [46]). Deviations from flatness are produced when $J_2 \neq J_{3a}$, as well as the addition of J_{3b} interactions. The question then arises if some qualitative feature in the non-flat NSF can provide us insights into the relevant further-neighbour interactions. Further, it turns out, that in the large-N approximation, one may extract λ from the neutron scattering intensity using certain general identities detailed below.

Considering the actual intensity of the NSF channel and the SF channel, one finds the geometrical identities true along the high symmetry lines (see panels (g), (h) and (i) of Fig. 3.7 - 3.10. Also see Fig. (3), panel **A** in Ref. [19]):

$$\left.\frac{d\sigma(\mathbf{Q})}{d\Omega}\right|_{hhh}^{\mathrm{NSF}} = \left.\frac{d\sigma(\mathbf{Q})}{d\Omega}\right|_{hhh}^{\mathrm{SF}}, \tag{3.66}$$

$$\left.\frac{d\sigma(\mathbf{Q})}{d\Omega}\right|_{hh\bar{h}}^{\mathrm{NSF}} = \left.\frac{d\sigma(\mathbf{Q})}{d\Omega}\right|_{hh\bar{h}}^{\mathrm{SF}}, \tag{3.67}$$

$$\left.\frac{d\sigma(\mathbf{Q})}{d\Omega}\right|_{00l}^{\mathrm{NSF}} = \left.\frac{d\sigma(\mathbf{Q})}{d\Omega}\right|_{00l}^{\mathrm{SF}}. \tag{3.68}$$

Here, the NSF and SF scattering intensity along the above mentioned lines in $\mathbf{q}$-space show exactly the same intensity. In the large-N approximation, we compute the intensities along the high symmetry directions of the SF and NSF channel and find :

$$\left.\frac{d\sigma(\mathbf{Q})}{d\Omega}\right|_{hhh}^{\mathrm{NSF}} = \left.\frac{d\sigma(\mathbf{Q})}{d\Omega}\right|_{hhh}^{\mathrm{SF}} = \left.\frac{d\sigma(\mathbf{Q})}{d\Omega}\right|_{hh\bar{h}}^{\mathrm{NSF}} = \left.\frac{d\sigma(\mathbf{Q})}{d\Omega}\right|_{hh\bar{h}}^{\mathrm{SF}} = K(h), \tag{3.69}$$

where $K(h)$ is given by:

$$K(h) = \frac{4}{3}\left(\frac{1}{\lambda + \frac{w - w\cos(h)}{T}}\right), \tag{3.70}$$

where $w = 2(J_2 - J_{3a} + 4J_{3b})$. Here, we have also considered the third neighbour interaction J_{3b} (see Appendix A.4). Note w is zero for ESI ($J_2 = J_{3a}$, $J_{3b} = 0$) where **q**-independent NSF scattering is obtained. Depending on the sign of w, either the minimum or the maximum will be $\frac{4}{3\lambda}$. Using the above equation, an easy scheme may be used to obtain λ from the neutron scattering intensities. The procedure is:

1. Obtain the line cuts along the (hhh) directions, $K(h)$. (here h is not in units of $2\pi/a$, further we remind the reader that the primitive unit cell length, $a = 1$ in this treatment.)

2. Obtain intensity $K(h)$ at points $h = \pi$ and $h = \pi/2$.

3. Utilize the identity $\frac{2}{K(\pi/2)} - \frac{1}{K(\pi)} = \frac{3\lambda}{4}$ to obtain the stiffness from the neutron scattering intensity.

3.3.4 Summary

In this chapter, we investigated Ising spins on a pyrochlore lattice and found:

- Flat bands (**q**-independent) in the eigenspectrum corresponding to eigenvector $|P\rangle$ (see Eq. (3.22)) in the $[hhl]$ plane.

- Geometrically, the NSF channel has contributions only from two of the four sublattices in a tetrahedron. In this thesis, these are sublattices 3 and 4 which define the

α-chains (see Fig. 3.5 and Fig. A.1).

- The neutron scattering expression (in Fourier space) may be written as $\langle P|\mathcal{M}^{-1}|P\rangle$ (see Eq. (3.48)) wherein the neutron projector $|P\rangle$, is proportional to the eigenvector for the flat bands (for NSF scattering) in the $[hhl]$ plane. This yields Eq. (3.53), i.e. $\frac{d\sigma(\mathbf{Q})}{d\Omega}|_{\rm NSF} = \frac{4}{3\lambda}$.

- NSF is also flat for ESI ($J_2 = J_{3a}$, see Ref. [63]) and Ising spins on a breathing pyrochlore (see next chapter and Appendix A.3) as the interaction matrix in these cases share the eigenvector $|P\rangle$ corresponding to the flat bands in the $[hhl]$ plane.

- The flat NSF intensity provides us a way to directly measure the stiffness of the Coulomb phase. The neutron scattering probes correlations of the emergent fluxes along (and perpendicular to) the neutron polarization directions (see Eq. (3.58)).

- A general scheme may be utilized to obtain the stiffness λ in the presence of further-neighbour interactions, as detailed in the previous section, using Eq. (3.70) and the geometrical identities of Eq. (3.69).

In this chapter, we studied Ising pseudo-spins on the pyrochlore lattice. We looked at magnetic neutron scattering using the Large-N approximation and further studied the spin flip and non-spin flip channels for polarized neutron scattering. In the next chapter, we shall study Heisenberg spins on a related lattice called the breathing pyrochlore lattice. Therein, we find various ordered phases including one ordered phase which is unreported in previous studies and a state characterized by line degeneracies[11]. We also find a phase with

[11]Line degeneracies in the momentum space eigenspectrum of the adjacency matrix

emergent tetrahedral clusters interacting via AFM exchange and a classical spin liquid for nearest-neighbour AFM interactions.

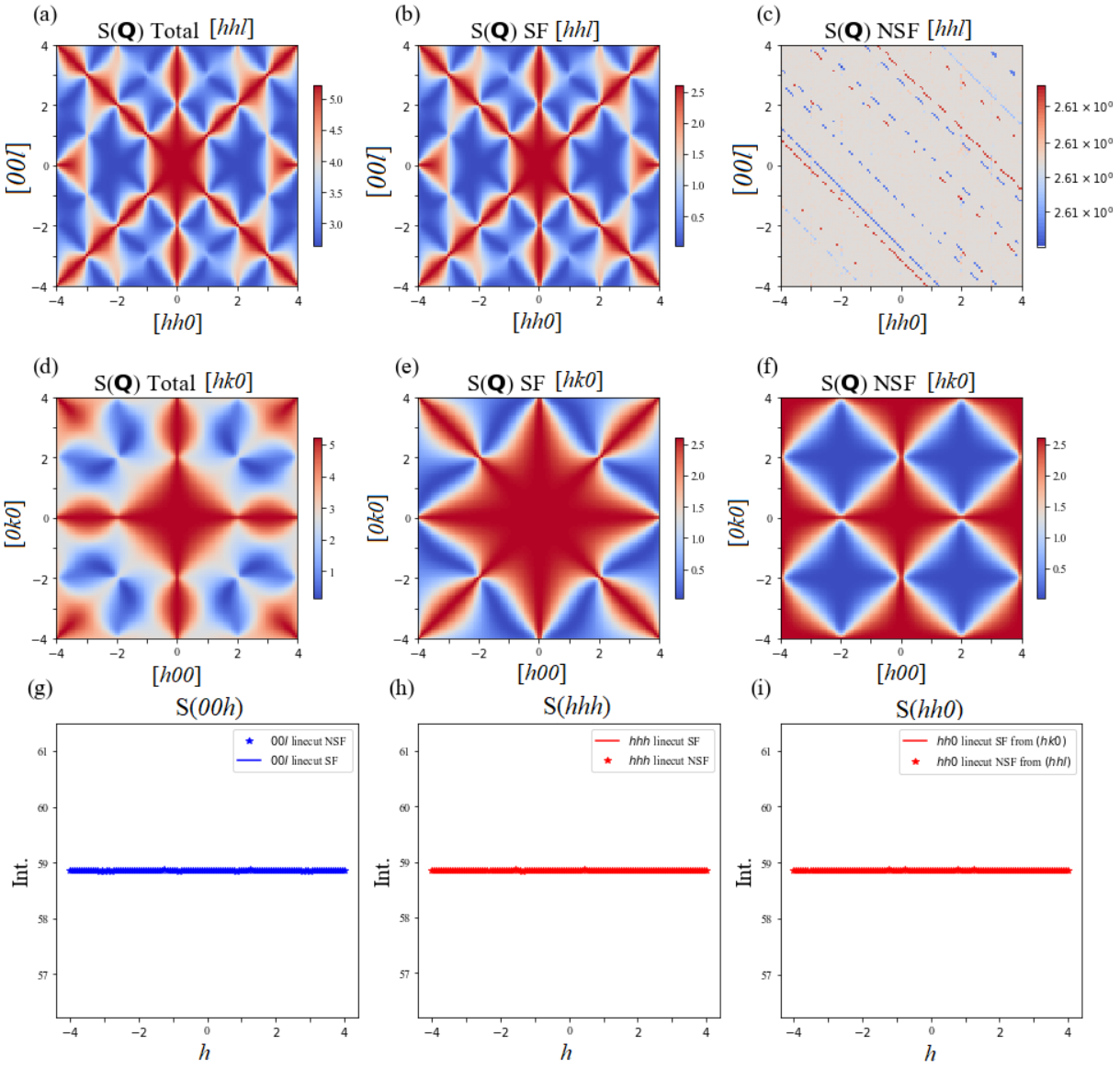

Figure 3.7: Figure shows neutron scattering structure factors $\mathrm{S}(\mathbf{Q})$ (using large-N) for spin ice, in the $[hhl]$ plane ((a), (b) and (c)), $[hk0]$ plane ((d), (e) and (f)) and its intensities on linecuts along $(00h)$, (hhh) and $(hh0)$ lines ((g), (h) and (i) respectively). (a) and (d) show the total neutron scattering while (b), (e) and (c), (f) show the SF and NSF channels respectively. Note the characteristic pinch-points at [111] and [200]. (c) shows the NSF channel, flat (upto machine precision) with intensity, $\frac{4}{3\lambda} \approx 2.6139$. (g), (h), (i) show equality of intensities along the aforementioned directions. Parameters: $T = 0.1$, $J = 1$, $\lambda = 0.510075$. The axes are in units of $\frac{2\pi}{a}$, except the y-axes of (g), (h) and (i) which are intensities, read off as $2.6139.. + \text{Int.} \times 10^{-12}$, where "Int." is the y-axis value.

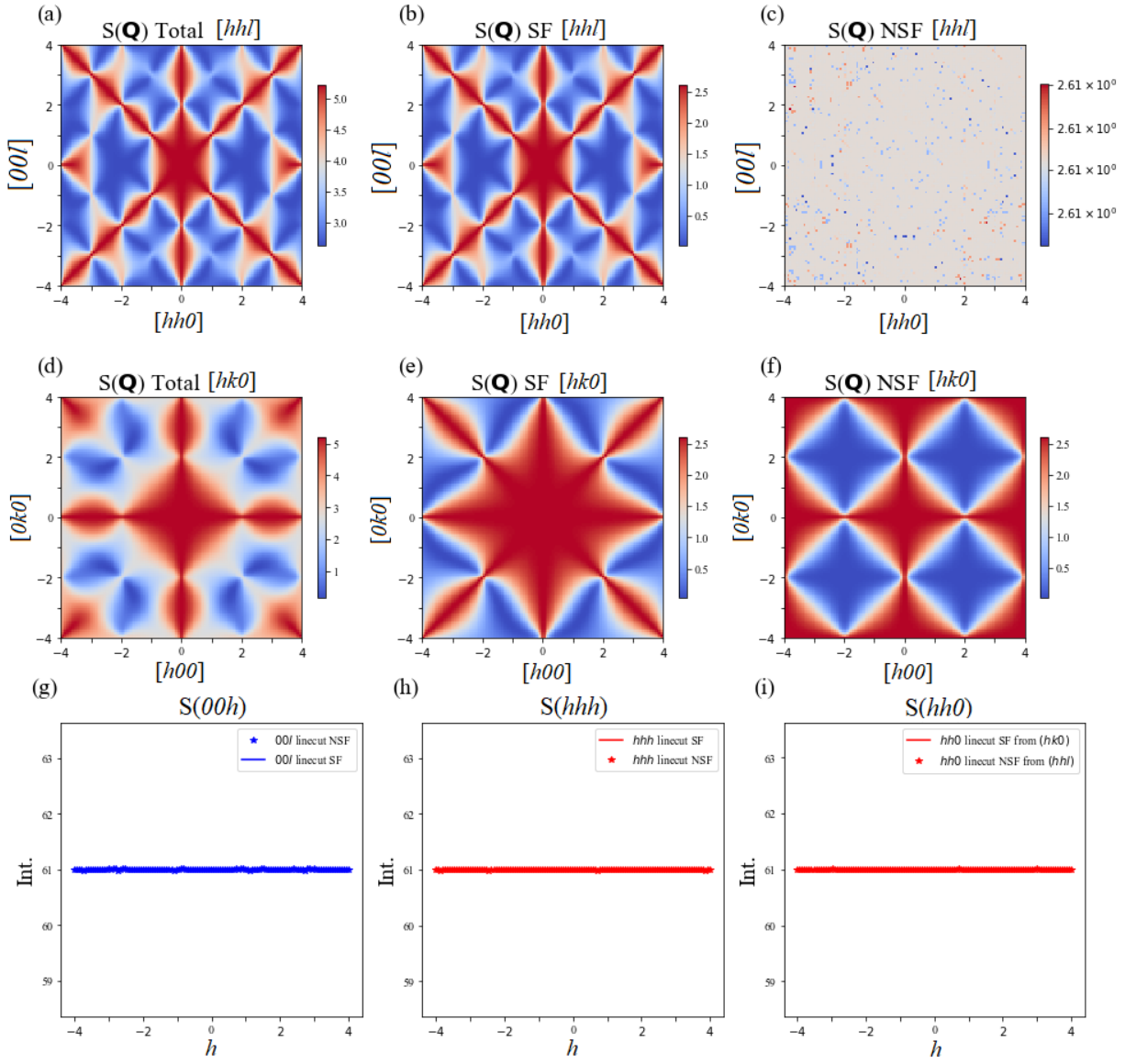

Figure 3.8: Figure shows neutron scattering structure factors S($\mathbf{Q}$) (using large-N) for ESI, in the $[hhl]$ plane ((a), (b) and (c)), $[hk0]$ plane ((d), (e) and (f)) and its intensities on linecuts along $(00h)$, (hhh) and $(hh0)$ lines ((g), (h) and (i) respectively). (a) and (d) show the total neutron scattering while (b), (e) and (c), (f) show the SF and NSF channels respectively. The pinch-points persist in ESI and the NSF channel is still flat (upto machine precision) with intensity $\frac{4}{3\lambda} \approx 2.610$. (g), (h), (i) show equality of intensities (upto machine precision) along the aforementioned directions. Parameters: $T = 0.1$, $J = 1$, $J_2 = J_{3a} = 0.02$, $\lambda = 0.5107969$. The axes are in units of $\frac{2\pi}{a}$, except the y-axes of (g), (h) and (i) which are intensities, to be read off as 2.610.. + Int. $\times 10^{-12}$, where "Int." is the y-axis value. .

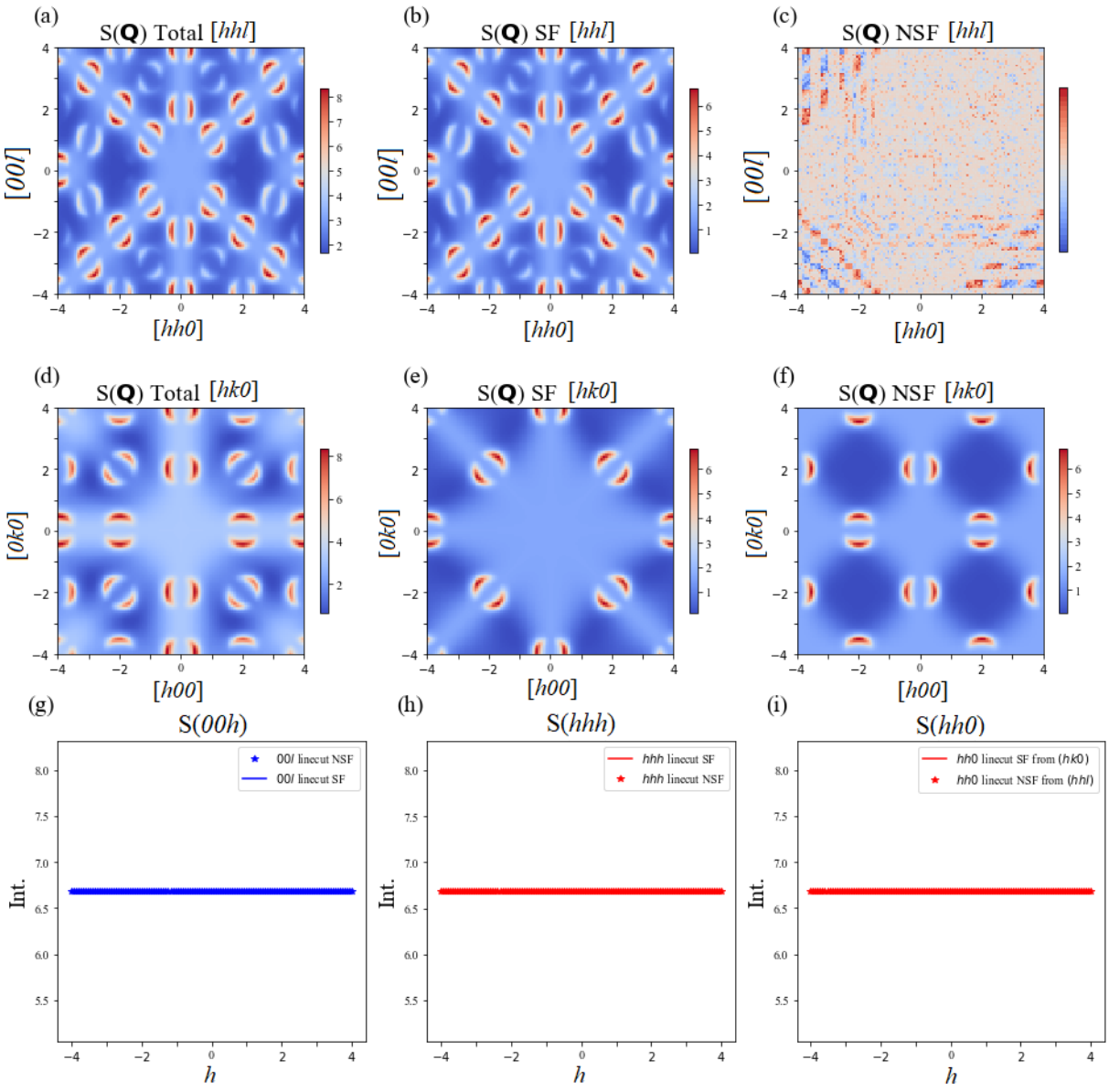

Figure 3.9: Neutron scattering structure factors $S(\mathbf{Q})$ (using large-N) for spin slush: A point on the ESI line given by $J_2 = J_{3a} = J/4$, at which the spins exhibit dynamical heterogeneity and the ground state is composed of two-in/two-out as well as three-in/one-out, three-out/one-in and all-in/all-out configurations of spins (see Ref. [63] for further details). Plots are in the $[hhl]$ plane ((a), (b) and (c)), $[hk0]$ plane ((d), (e) and (f)) and its intensities on linecuts along $(00h)$, (hhh) and $(hh0)$ lines ((g), (h) and (i) respectively). (a) and (d) show the total neutron scattering while (b), (e) and (c), (f) show the SF and NSF channels respectively. The scattering shows half moon features, centred at the zone centres characteristic of spin slush. (g), (h), (i) display the linecuts showing $\mathbf{q}$-independent neutron intensities. The NSF channel is flat with intensity $\frac{4}{3\lambda} \approx 1.6284$. Parameters: $T = 0.4$, $J = 1$, $J_2 = J_{3a} = 0.25$, $\lambda = 0.818779$. The axes are in units of $\frac{2\pi}{a}$, except the y-axes of (g), (h) and (i) which are intensities, read as $1.628 + \text{Int.} \times 10^{-12}$.

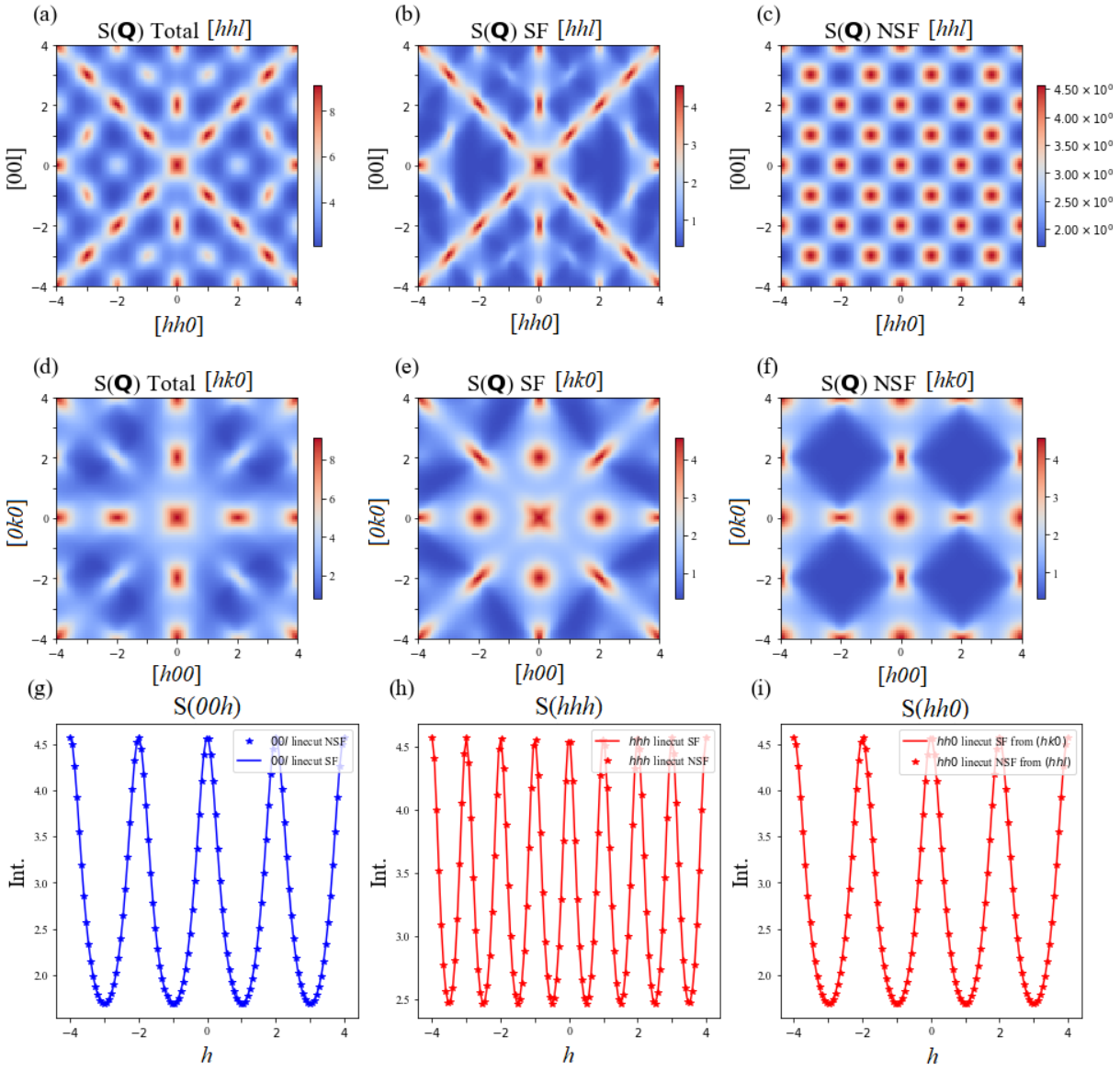

Figure 3.10: Figure shows neutron scattering structure factors S($\mathbf{Q}$) (using large-N) for Ising spins on a pyrochlore interacting via further-neighbour interactions, J_2 and J_{3a} of unequal magnitudes. S($\mathbf{Q}$) is shown in the $[hhl]$ plane ((a), (b) and (c)), $[hk0]$ plane ((d), (e) and (f)) and its intensities on linecuts along $(00h)$, (hhh) and $(hh0)$ lines ((g), (h) and (i) respectively). (a) and (d) show the total neutron scattering while (b), (e) and (c), (f) show the SF and NSF channels respectively. Note the checkerboard pattern in the NSF channel. (g), (h), (i) show equal intensities along the aforementioned directions.This would have been flat if $J_2 = J_{3a}$, but is now modulated via Eq. (3.70) and the maxima is given by $\frac{4}{3\lambda} \approx 4.573$. Parameters: $T = 1.6$, $J = 1$, $J_2 = -0.1$, $J_{3a} = -0.2$, $\lambda = 0.2915469$. The axes are in units of $\frac{2\pi}{a}$ except the y-axes of (g), (h) and (i) which are intensities.

Chapter 4

Heisenberg Spins on a Breathing Pyrochlore Lattice

4.1 Introduction and Materials

In this chapter, we study Heisenberg spins on a breathing pyrochlore lattice (see Appendix A.3). The breathing pyrochlore lattice is composed of corner-sharing tetrahedra of two different sizes, i.e. all the "up" tetrahedra are larger (in our conventions) than the "down" tetrahedra (see Fig. 4.1). This breathing anisotropy leads to two new free parameters. One of these is due to the ratio ($B_f \equiv \frac{J_b}{J_a}$) of interaction strengths between the larger (J_b) and smaller tetrahedra (J_a) and the other parameter is the ratio between the bond lengths of the two tetrahedra given by $\gamma \equiv \frac{L_b}{L_a}$. Here, L_b is the bond length of the bigger tetrahedra and L_a is that of the smaller tetrahedra (see Fig. 4.1(b)). After a short discussion of

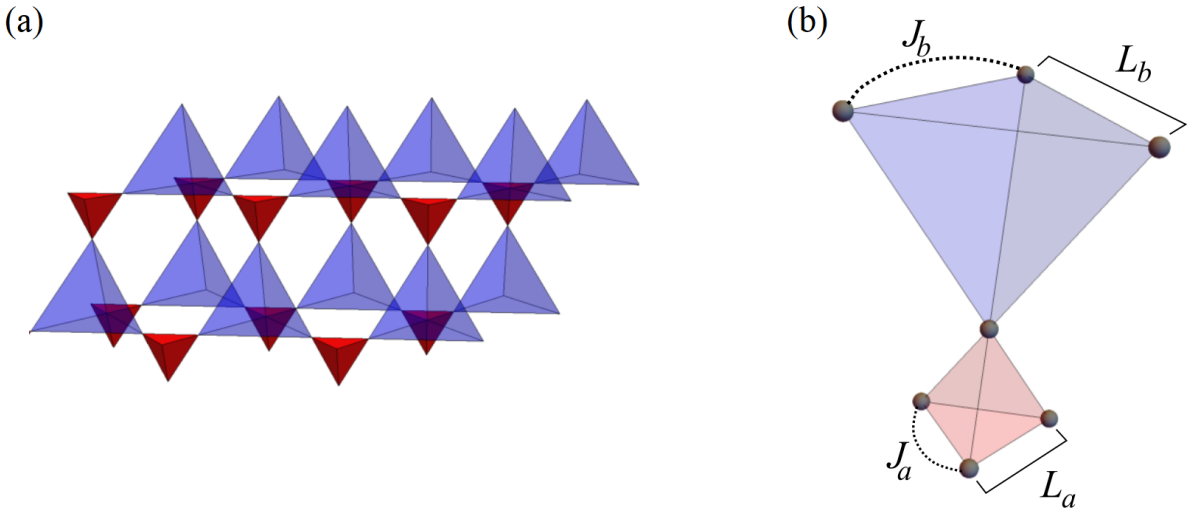

Figure 4.1: Figures illustrate the breathing pyrochlore with blue large tetrahedra and small red ones. Panel (a) shows the breathing lattice and illustrates that the breathing pyrochlore may be constructed from tetrahedra of just one type i.e. either the red ones or the blue ones (the author suggests imagining the blue tetrahedra to be transparent). Panel (b) shows a tetrahedral unit with the two couplings introduced in the text namely J_a and J_b as well as the bond lengths i.e. L_a and L_b.

materials and relevant models, we first review the J_a and J_b case, to survey the magnetic phases without any further-neighbour coupling. We find the well studied classical spin liquid for both AF J_a and J_b, the ferromagnet for both FM J_a and J_b and for oppositely signed J_a and J_b, we find a phase with clusters of spins behaving as emergent moments and interacting via AFM interactions [21]. We then add a further J_2 coupling (see Fig. 4.10), study the ordered phases at the mean field level and provide phase diagrams of the same.

Naturally, one begins by asking what happens in the extreme case where either coupling J_a or J_b is negligibly small. This is the isolated tetrahedra limit where the single tetrahedron model is valid [23, 67]. The breathing pyrochlore lattice is constructed with layers of small

tetrahedra where the big tetrahedra just take up the space between the layers (see Fig. 4.1 and Appendix A.3), thus the ions in a small tetrahedra cluster together and the physics of the isolated tetrahedra emerges.

$Ba_3Yb_2Zn_5O_{11}$ (BYZO) is an example of such a compound where the interactions are significant for just the small Yb^{3+} tetrahedra ($B_f \approx 0$) [23, 67, 68, 69]. Moreover, the bond-length ratio γ is close to 2, leading to effectively decoupled tetrahedron. Inelastic neutron scattering and thermodynamic data were used to extract the relevant parameters for the effective single tetrahedron anisotropic exchange model and found predominant Heisenberg anti-ferromagnetic exchange with a large Dzyaloshinskii-Moriya interaction [67].

Intermediate range of B_f is realized in a family of A-site ordered spinels [70, 71] (space group $F\bar{4}3m$) involving transition metal ions on a breathing pyrochlore lattice. This so called chromium breathing pyrochlore family has recently gained much attention [22, 72] and consists of a broad range of compounds. Most notably $LiInCr_4O_8$, $LiGaCr_4O_8$, $LiInCr_4S_8$, $LiGaCr_4S_8$, $CuInCr_4S_8$ and $CuInCr_4Se_8$ were studied using density functional theory (DFT) [73] and PFFRG (pseudo-fermion functional renormalization group) [13, 74, 75, 76] and it was concluded that further-neighbour exchange leads to appreciable change in the low temperature correlations and magnetic behaviour as compared to just the nearest-neighbour case [22].

Further, while the oxide materials have anti-ferromagnetic nearest-neighbour interactions, substitution of the oxygen with larger anions such as sulfur or selenium was noted to enhance ferromagnetic exchange couplings for one or both tetrahedra [21, 22]. DFT analysis was carried out at low temperature for $LiInCr_4O_8$ and $LiGaCr_4S_8$. All the above

Material	J_a	J_b
$LiInCr_4O_8$	AFM	AFM
$LiGaCr_4O_8$	AFM	AFM
$LiInCr_4S_8$	FM	FM

Material	J_a	J_b
$LiGaCr_4S_8$	FM	FM
$CuInCr_4S_8$	AFM	FM
$CuInCr_4Se_8$	FM	FM

Table 4.1: Showing the nearest-neighbour exchange couplings obtained from the DFT analysis of Ref. [22] at room temperatures. Larger anions such as selenium and sulpher are seen to enhance FM couplings as compared to oxygen.

mentioned compounds were also analyzed (using DFT) at room temperature. They found that, while $LiInCr_4O_8$ and $LiGaCr_4O_8$ have spins on both tetrahedra interacting via anti-ferromagnetic exchange, $LiInCr_4S_8$, $LiGaCr_4S_8$ and $CuInCr_4Se_8$ have both J_a and J_b as ferromagnetic. $CuInCr_4S_8$ was found to have opposite signs for the two tetrahedra [22] (see Tab. 4.1). Further-neighbour interactions also play a prominent role in these compounds with larger coupling strengths in the sulfide compounds.

The isotropic Heisenberg model with anti-ferromagnetic $J_a = J_b$ is a classical spin liquid [21, 22] and has a large groundstate degeneracy, which manifests as two low-lying flat bands (see Sec. 3.2.2 and Fig. 4.4) in the eigenspectrum. The addition of J_2 and other further-neighbor interactions typically lift this ground state degeneracy and the model tansitions into an ordered state (below T_c acc. to MFT, see Eq. (2.50)).

Interestingly, the compounds $LiInCr_4O_8$ and $LiGaCr_4O_8$, first synthesized in 1966 [70, 77], undergo a two-state symmetry lowering process: a magneto-structural transition followed by magnetic ordering as one lowers the temperature [72, 78]. The effect of distortions and spin-lattice coupling was theoretically examined based on a "site-phonon" Heisenberg

model. Such a model leads to effective bi-quadratic spin-spin interaction which drives the system to order into a $\mathbf{q}_{\text{ord}} = (1/2, 1/2, 1/2)$ state in the presence of strong spin-lattice coupling and into a $\mathbf{q}_{\text{ord}} = (1, 1, 0)$ state when spin-lattice coupling is weak [72]. The chromium ions have a spin of $S = 3/2$ and our large-N and MFT computations should be quite relevant for temperatures above any such aforementioned transition [21, 22].

In the next section, we introduce the Hamiltonian for isotropic spins residing on a breathing lattice. We first analyze the scenario for $J_a \neq J_b$ and then consider the effect of next nearest-neighbour exchange coupling, J_2.

4.2 Model Hamiltonians

In this section, we introduce the effective Heisenberg Hamiltonian with inequivalent nearest-neighbour exchange couplings J_a and J_b. It is given by [21]:

$$\mathcal{H} = \frac{1}{2}\left(\sum_{(i,c);\,(j,d)\in A} J_a\, A_{ij}^{cd}\; \mathbf{S}_i^c \cdot \mathbf{S}_j^d + \sum_{(i,c);\,(j,d)\in B} J_b\, B_{ij}^{cd}\; \mathbf{S}_i^c \cdot \mathbf{S}_j^d \right). \tag{4.1}$$

Here J_a is the magnetic exchange between ions in the smaller tetrahedra while J_b represent the couplings in the larger tetrahedra. i, j are FCC site labels and c, d are sublattice labels. The first and second sum are between spins in the small (A) and big (B) tetrahedra respectively. A_{ij}^{cd} and B_{ij}^{cd} are the adjacency matrices for the small and big tetrahedra in real space. Their Fourier transforms may be found in Appendix A.4. Further information on the breathing lattice may be found in Appendix A.3. The Fourier transform definition

is reproduced for convenience and is given by:

$$J^{cd}(\mathbf{q}) = \sum_{i,j} J_{ij}^{cd}\, e^{i\mathbf{q}\cdot(\mathbf{R}_i^c - \mathbf{R}_j^d)}. \tag{4.2}$$

Here, $J(\mathbf{q})$ is the Fourier transformed adjacency matrix and $\mathbf{R}_i^a$ denotes the site on FCC lattice point i and sublattice c. Here, J_{ij}^{cd} is the real space adjacency matrix and is given by:

$$J_{ij}^{cd} = J_a A_{ij}^{cd} + J_b B_{ij}^{cd} \tag{4.3}$$

We study the eigensystem of $J(\mathbf{q})$ and utilize the ordering wavevectors ($\mathbf{q}_{\text{ord}}$) to characterize the phases. The $\mathbf{q}_{\text{ord}}$ are the wavevectors at which the eigenvalues of $J(\mathbf{q})$ is a global minimum (further discussed in later sections, see Sec. 4.3.2 and Eq. (2.50) and ensuing discussions).

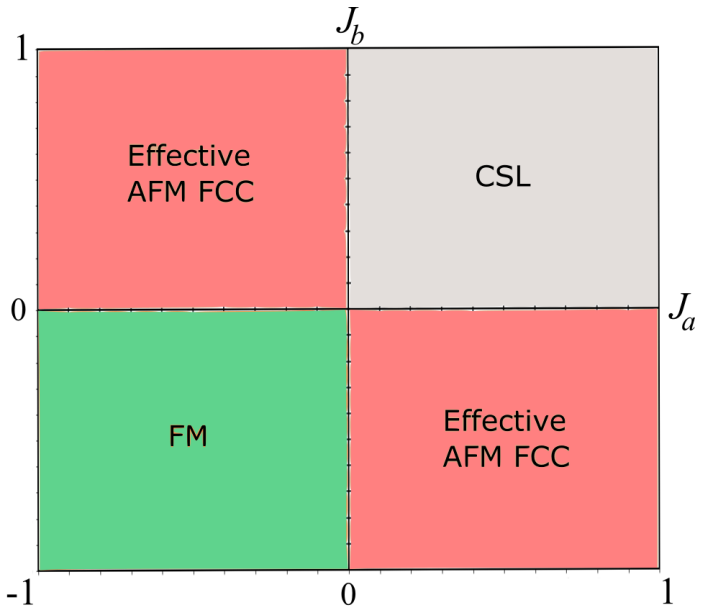

Figure 4.2: Mean field phase diagram for J_a and J_b. A Coulomb spin liquid is stabilized when both exchange parameters are AFM and positive (in the first quadrant). Negative parameters result in a FM ordered phase with ordering wavevector $(\mathbf{q}_{\text{ord}}) = \frac{2\pi}{a}(0,0,0)$. Oppositely signed J_a and J_b result in an effective AFM-FCC phase with ordering wavevectors of the type $(\mathbf{q}_{\text{ord}}) \equiv \frac{2\pi}{a}(h,0,1)$ and other symmetry related points, in which h is not selected at the MF level, thus exhibiting a line degeneracy.

4.2.1 Review of $\mathbf{J_a}$ - $\mathbf{J_b}$ Phase Diagram

We first review the expected phases and spin-structure factors with differing J_a and J_b but with no further-neighbour interactions. While Benton and Shannon constructed their phase diagram using analytical arguments [21], we do so by characterizing the ordering wavevectors at which the eigenvalue of the momentum space adjacency matrix is minimum for all $\mathbf{q}$-vectors in the FBZ (see Fig. 4.2, Eq. (2.50) and following discussions, also see Ref. [35]). In this section, $\mathbf{Q}$ and $\mathbf{q}$ are used interchangeably and denote any wavevector in reciprocal space. The transition temperature, T_c, according to mean-field theory is this global minimum eigenvalue divided by the number of components of the spins. We denote the four unique eigenvalues in $\mathbf{q}$-space as Λ_1, Λ_2, Λ_3 and Λ_4.

For $J_a = J_b$, that is the isotropic limit, there are two degenerate low lying flat (independent of $\mathbf{q}$) bands in the eigenspectrum (see Sec. 3.2.2 and Fig. 4.3) indicating massive ground state degeneracy in the FBZ leading to the characteristic pinch-points (see Fig. 4.4(c)) in the spin structure factor [11, 19, 21, 42, 43, 45, 79]. Likewise, for different anti-ferromagnetic J_a and J_b, this degeneracy persists and we observe pinch-points (see Fig. 4.4(c)) at low temperatures hinting at the existence of a Coulomb phase [11, 17, 45]. This $\mathbf{q}$-independent degeneracy may be further investigated by analytically computing the eigenvalues, two (six when using 12×12 adjacency matrix[1]) of which are given by [21]:

$$\Lambda_1 = \Lambda_2 = -J_a - J_b. \tag{4.4}$$

[1]The Fourier transformed 12×12 adjacency matrix for isotropic interactions takes the form $J^{cd}(\mathbf{q})\,\delta_{\mu\nu}$ where c, d are sublattice labels and μ, ν are spin components.

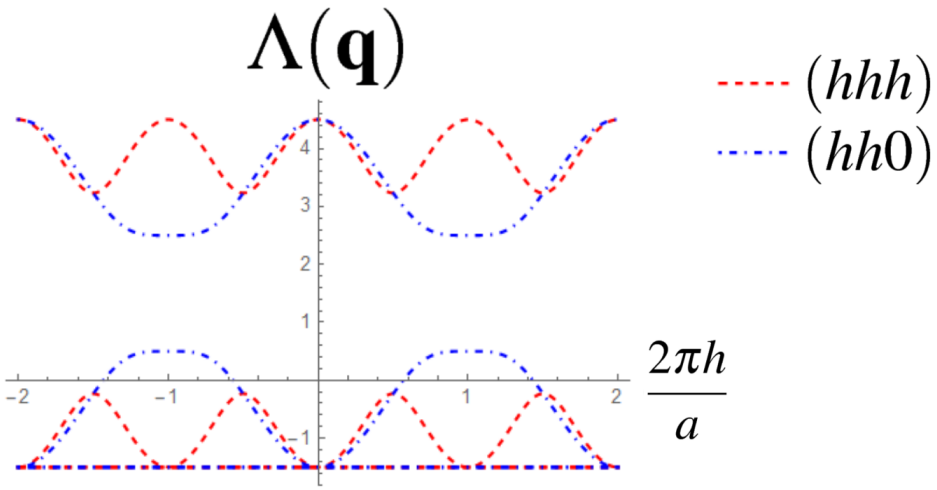

Figure 4.3: Eigenvalues $\Lambda(\mathbf{q})$, as a function of $\mathbf{q}$ in units of $\frac{2\pi}{a}$ (h takes values in the ticks). Here $J_a = 1$ and $J_b = 0.5$. Note the low lying flat bands along the (hhh) and $(hh0)$ signifying massive ground state degeneracy.

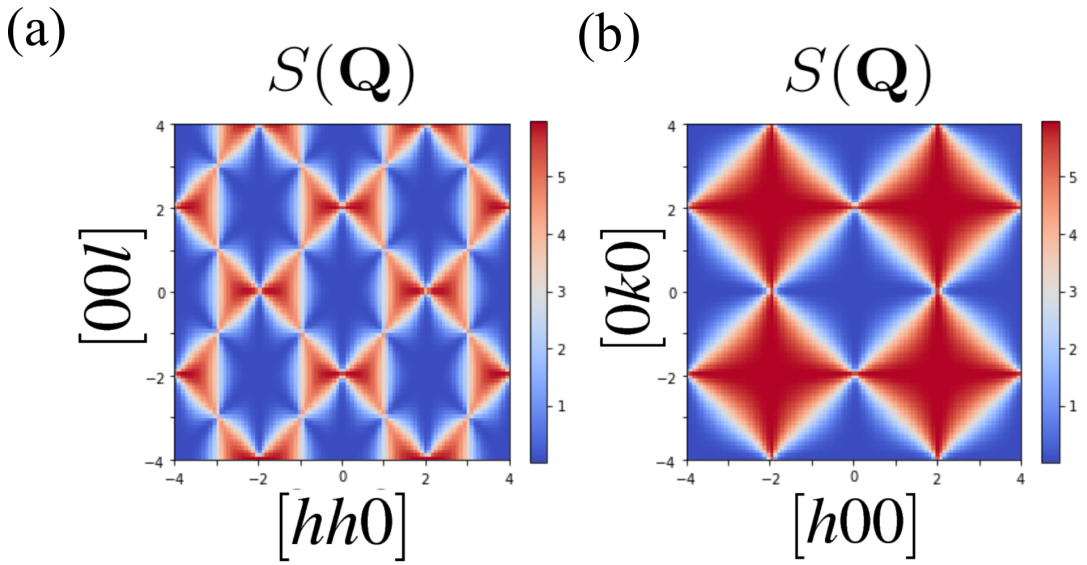

Figure 4.4: Spin susceptibilities $S(\mathbf{Q})$ in the $[hhl]$ and $[hk0]$ planes using large-N approximation. Note the pinch-points in panel (a) (in the $[hhl]$ plane) at [220] Intensity has arbitary units and the axes are in units of $\frac{2\pi}{a}$. Here $J_a = 1$, $J_b = 0.5$ and $T/J_a = 0.005$.

This is the minimum branch for both anti-ferromagnetic J_a and J_b. This condition leads to net spin of each tetrahedron vanishing separately to minimize the Hamiltonian [60, 79]. To show this, we rewrite the sum in the Hamiltonian as a sum over spins in each tetrahedra (magnetization is denoted by $\mathbf{M}_\tau$) and a sum over terahedra (an overall additive constant ignored here [79]), given by:

$$\mathcal{H} = \frac{1}{2}\left(J_a \sum_{\tau \in A} {\mathbf{M}_\tau}^2 + J_b \sum_{\tau \in B} {\mathbf{M}_\tau}^2 \right), \tag{4.5}$$

where the magnetization in each tetrahedra is given by:

$$\mathbf{M}_\tau = \sum_{a \in \tau} \mathbf{S}_a.$$

Here, $\mathbf{S}_a$ is a spin in the tetrahedron denoted by τ. The above equation shows that $\mathbf{M}_\tau = \mathbf{0}$ is a classical ground state of the system with positive J_a and J_b [21, 79]. The other two eigenvalues are $\mathbf{q}$-dependent and are given by:

$$\Lambda_{3,4}(\mathbf{q}) = J_a + J_b \pm G(\mathbf{q}), \tag{4.6}$$

where $G(\mathbf{q})$ is given by:

$$G(\mathbf{q}) = 2\sqrt{J_a J_b \cos\left(\frac{q_z}{2}\right)\left(\cos\left(\frac{q_x}{2}\right) + \cos\left(\frac{q_y}{2}\right)\right) + J_a J_b \cos\left(\frac{q_x}{2}\right)\cos\left(\frac{q_y}{2}\right) - J_a J_b + J_a^2 + J_b^2}.$$

Fig. 4.3 and Fig. 4.4 illustrate the case for $J_a = 1$, $J_b = 0.5$. The eigenvalues, $\Lambda(\mathbf{q})$, which are functions of the reciprocal lattice vectors $\mathbf{q}$ are plotted along the (hhh)

and $(hh0)$ lines showing the persistent degeneracy in the FBZ. Fig. 4.4 shows the spin structure factors $S(\mathbf{Q})$ (computed using Eq. (2.68) and Eq. (2.65)[2]) and the pinch-points therein at $\frac{2\pi}{a}(0,0,2)$, $\frac{2\pi}{a}(0,2,2)$ and symmetry related points. Thus we see, for the case of anti-ferromagnetic and inequivalent J_a and J_b , there is a degenerate classical ground state (which translates to extensive number of degenerate ordering wavevectors at the MF level) and the model is in a Coulomb phase at low temperatures [21].

When J_a and J_b are both ferromagnetic (negative in our convention), the Hamiltonian (4.5) is minimum for ${\mathbf{M}_\tau}^2 = 1$. Thus the magnetization on each tetrahedra is maximal and the system has a collinear ferromagnetic ground state (see Fig. 4.17(a)). This is further illustrated in Fig. 4.5 showing the eigenvalues and the spin-susceptibility (Fig. 4.6) $S(\mathbf{Q})$[3]. Fig. 4.5 shows the minimum of the eigenvalues appearing at $\frac{2\pi}{a}(0,0,0)$ and other zone centres signifying a $\mathbf{q} = 0$ ferromagnetic ordered state.

When J_a and J_b are of opposite sign, the ferromagnetic tetrahedra with four spins collinearly align and behave as a single magnetic moment (effective $S = 6$ for Cr^{3+} ions[4]) which interacts anti-ferromagnetically with the other effective moments arranged in an FCC lattice (see Fig. 4.7). The system thus behaves as an effective FCC anti-ferromagnet (effective AFM-FCC) and the spin structure factor $S(\mathbf{Q})$ of this system is given by $S(\mathbf{Q})$ of the FCC anti-ferromagnet multiplied with the square of the Fourier transform of the pyrochlore magnetic basis form factor (see appendices of Ref. [22]). In the nearest-neighbour anti-ferromagnetic FCC model, it is known that thermal fluctuations favour states with

[2] In the large-N approximation, we first find the lagrange multiplier λ using Eq. (2.65) and then substitute it in Eq. (2.68) to obtain the structure factor which is plotted in $\mathbf{q}$-space.

[3] Q and q are used interchangably here.

[4] $S = 3/2$ for Cr^{3+} ions.

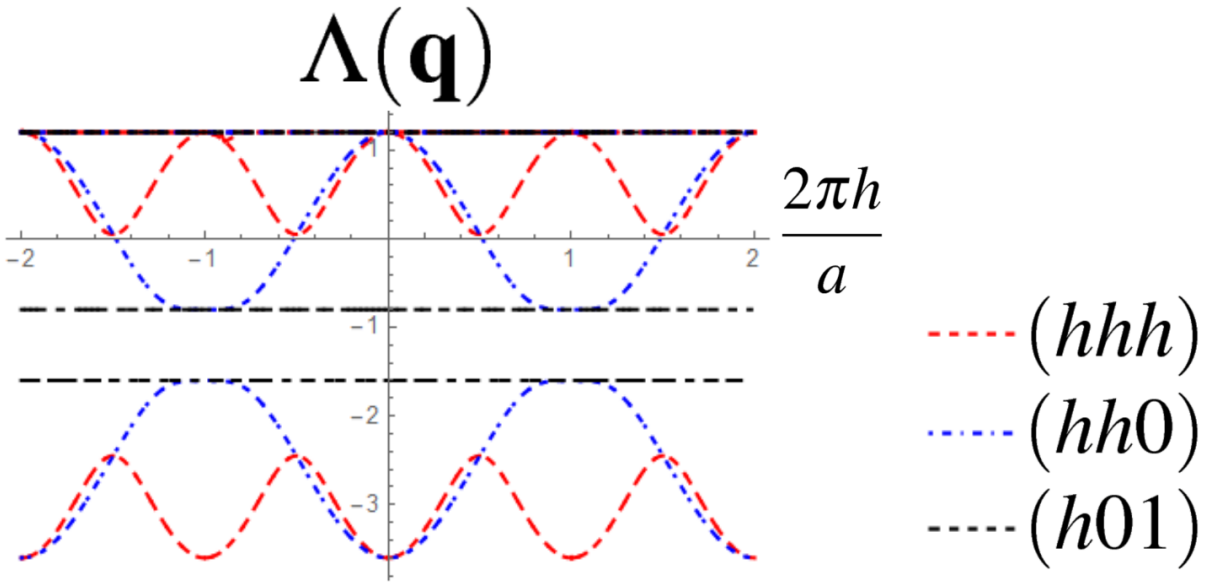

Figure 4.5: Eigenvalues $\Lambda(\mathbf{q})$, as functions of $\mathbf{q}$ in units of $\frac{2\pi}{a}$ (h takes values of the ticks). Here J_a= -0.7 and J_b= -0.5. Note the minima at ordering vectors $\frac{2\pi}{a}(0,0,0)$ and other symmetry related points.

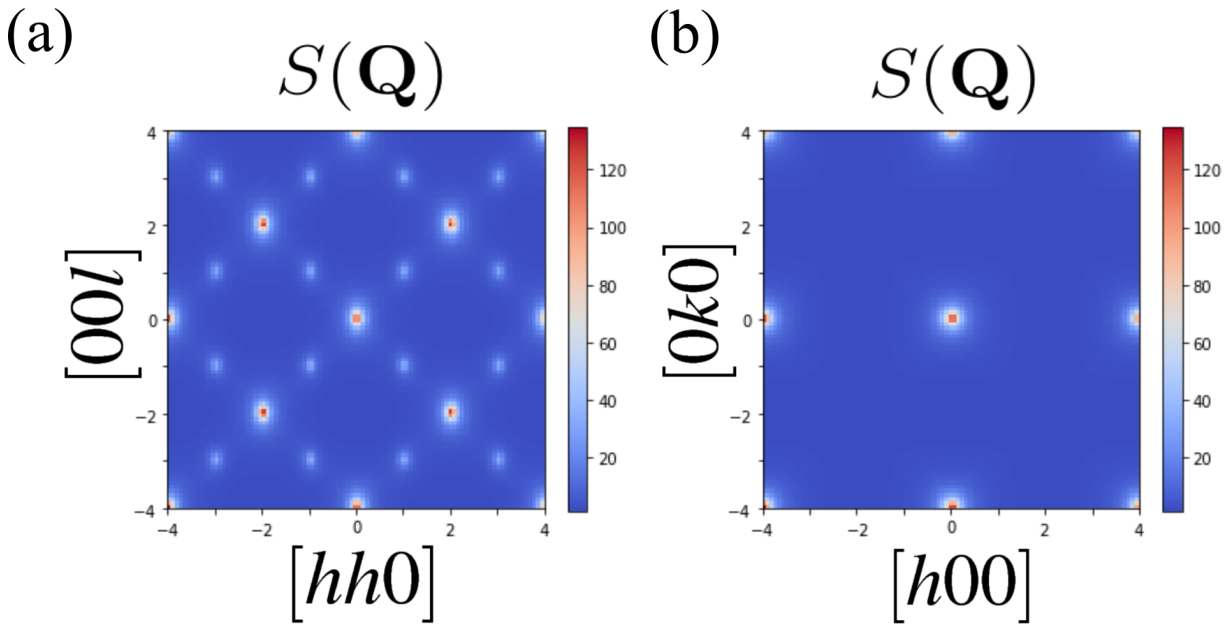

Figure 4.6: Spin susceptibilities $S(\mathbf{Q})$ in the $[hhl]$ and $[hk0]$ planes using large-N approximation. Intensity has arbitrary units and the axes are in units of $\frac{2\pi}{a}$. Here J_a = -0.7, J_b = -0.5 and T/J_a = 0.6 showing peaks at ordering vectors $\frac{2\pi}{a}(0,0,0)$ and other zone centers.

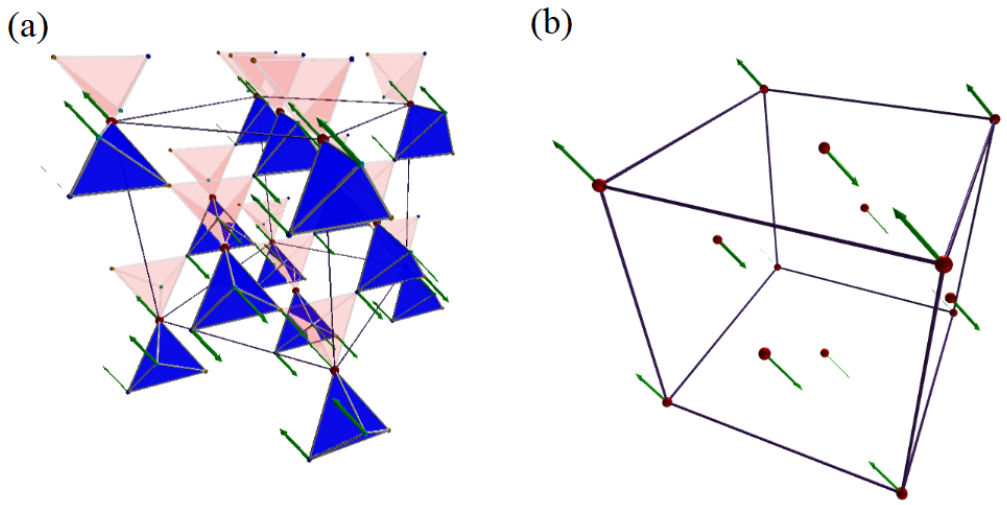

Figure 4.7: Figures show the effective anti-ferromagnet on a FCC lattice. (a) Ferromagnetically interacting spins on a tetrahedra, cluster to form effective magnetic moments. (b) shows these effective moments (anti-ferromagnetically interacting) on the FCC lattice.

$\mathbf{q_{ord}} = \frac{2\pi}{a}(1,0,0)$ referred to Type I AFM [80] as evidenced by spin-wave calculations and Monte-Carlo simulations [81, 82]. The breathing pyrochlore with J_a and J_b of opposite signs has a line degeneracy along the $\frac{2\pi}{a}(1,0,h)$ and symmetry related directions [21]. This is illustrated in Fig. 4.8, where the black dashed lines are the minima along the $\frac{2\pi}{a}(h,0,1)$ direction. In this phase the spin structure factor show distinctive square ring features as shown in Fig. 4.9(b).

Similar to the case of AFM spins on the FCC lattice, one expects order by disorder to select the ordering wavevectors given by $\mathbf{q_{ord}} = \frac{2\pi}{a}(1,0,0)$ and its symmetry related points [21]. This is further strengthened by pseudo-fermion functional renormalization group (PFFRG) calculations [79] which take into consideration both thermal and quantum order by disorder phenomena and show the selection of ordering vectors $\mathbf{q_{ord}} = \frac{2\pi}{a}(1,0,0)$

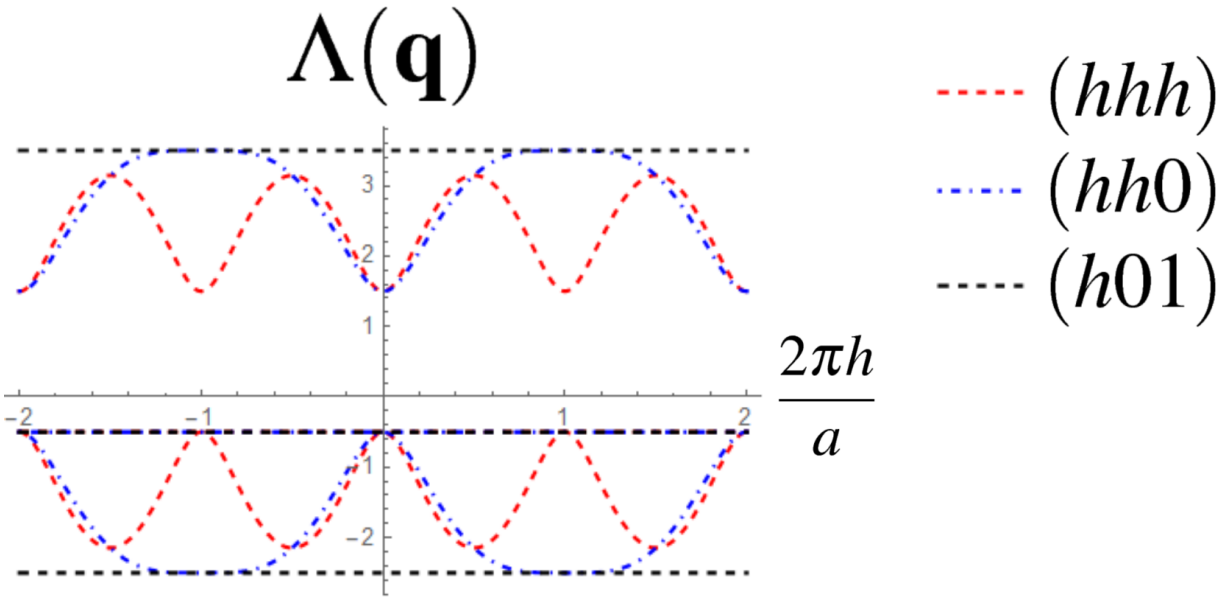

Figure 4.8: Eigenvalues $\Lambda(\mathbf{q})$, as functions of wavevectors $\mathbf{q}$ in units of $\frac{2\pi}{a}$. Here J_a= 1 and J_b= -0.5. Note the degenerate minima at ordering vectors of the form $\frac{2\pi}{a}(q, 0, 1)$ and other symmetry related points.

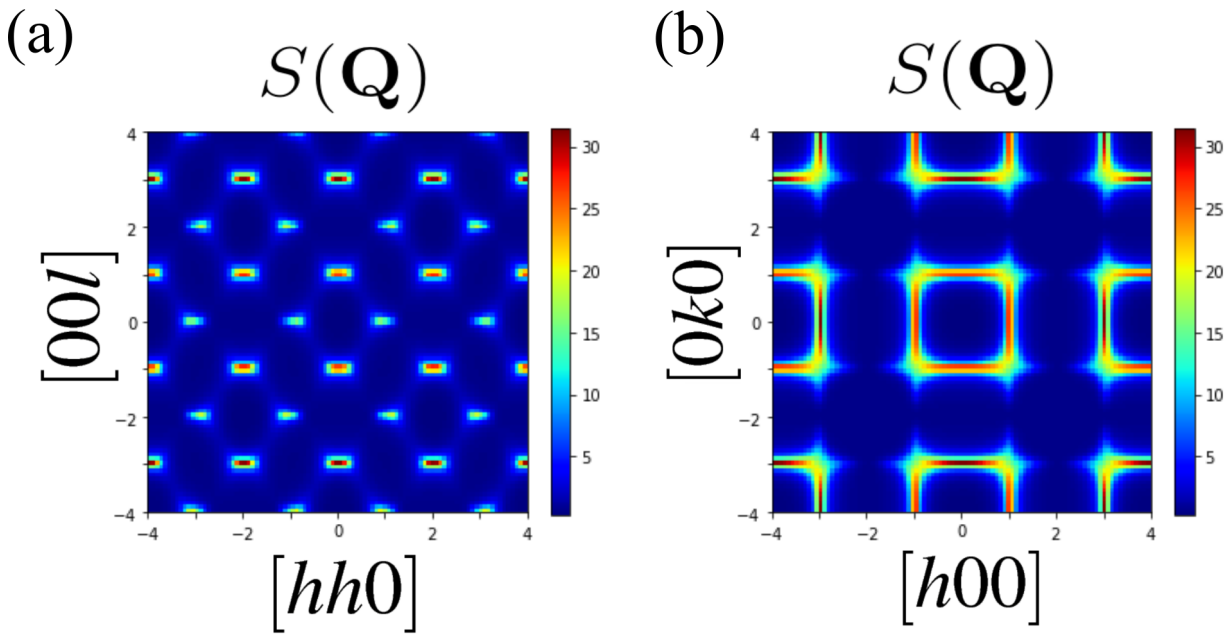

Figure 4.9: Spin susceptibilities $S(\mathbf{Q})$ in the $[hhl]$ and $[hk0]$ planes using large-N approximation. Note the square ring features in the $[hk0]$ plane. Intensity has arbitrary units and the axes are in units of $\frac{2\pi}{a}$. Here $J_a = 1$, J_b = -0.5 and $T/J_a = 0.1$.

in this system.

This subextensive (line degeneracies) classical ground state degeneracy is indicated by the formation of square ring features of $S(\mathbf{Q})$ in the $[hk0]$ plane (see Fig. 4.9(c)) which extend from $\frac{2\pi}{a}(1,0,-1)$ to $\frac{2\pi}{a}(1,0,+1)$. This phase is called the effective AFM-FCC phase in this thesis.

Summarizing, we find:

- **Coulomb phase** when $J_a,\ J_b > 0$.
- **Ferromagnet** when $J_a,\ J_b < 0$.
- **Effective AFM-FCC phase** when $J_a \times J_b < 0$.

In this section, we studied the effect of inequivalent nearest-neighbour exchange $J_a \neq J_b$. This analysis has not considered any further-neighbour exchange. However, the effect of further-neighbour interactions is significant and plays a key role in the physics of such systems [11, 22, 42]. In the next section, we consider the effect of further-neighbour interactions and analyze what happens in the system in the presence of a second nearest-neighbour J_2 interaction.

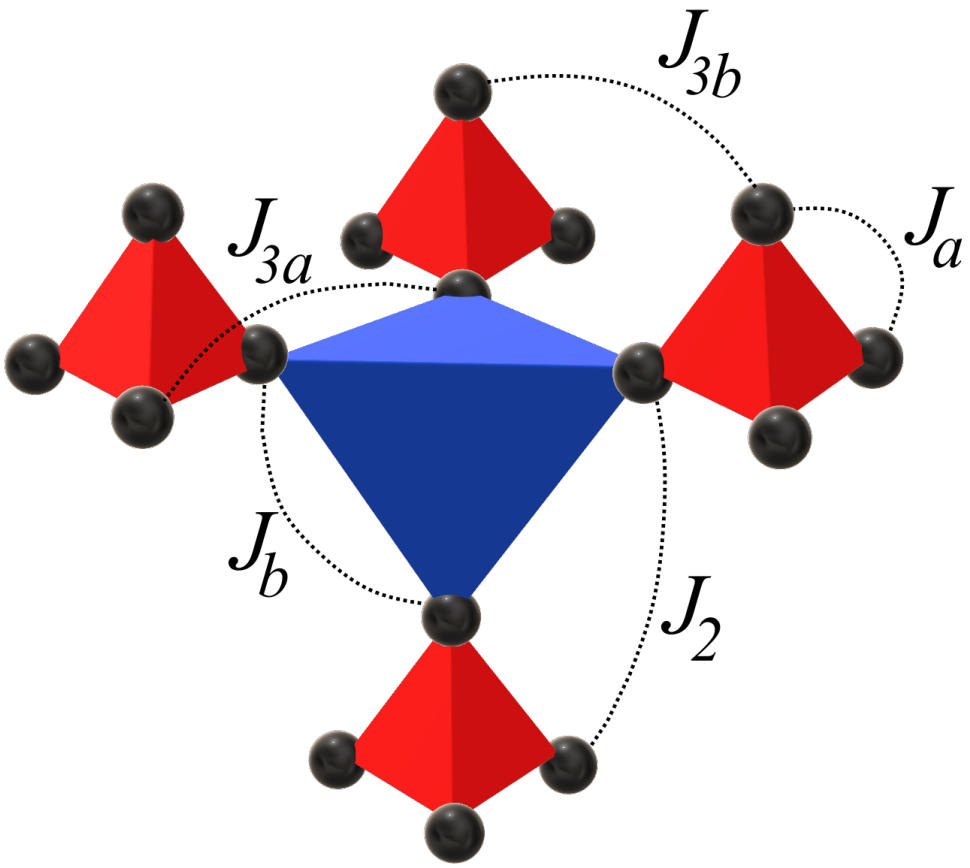

Figure 4.10: Figure showing part of the breathing pyrochlore with nearest-neighbour exchange couplings J_a and J_b. Also included are second nearest-neighbour coupling J_2 and two inequivalent third neighbour coupling J_{3a} and J_{3b} connecting same sublattices in different tetrahedra.

4.2.2 Why study the effect of further-neighbour interactions?

In the pure $J_a - J_b$ model with both ferromagnetic exchange, while one expects ferromagnetic $\mathbf{q} = 0$ order such as in $CuInCr_4Se_8$ [70], two of the studied chromium sulfides, (in Ref. [22]) $LiInCr_4S_8$ and $LiGaCr_4S_8$ were theoretically found to not order ferromagnetically (both have ferromagnetic J_a, J_b). Instead, their spin-structure factors show square ring features indicating that the system is an effective AFM-FCC just like $CuInCr_4S_8$ (where it is expected) [22]. This behaviour is readily explained by considering $J^{\text{eff}}_{\text{FCC}}$, which is the effective coupling between magnetic moments on the FCC lattice given by [22, 83]:

$$J^{\text{eff}}_{\text{FCC}} = (J_{\text{AFM}} + 4J_2 + 2J_{3a} + 2J_{3b})/16. \tag{4.7}$$

Here J_{AFM} is the nearest-neighbour coupling of the anti-ferromagnetically coupled tetrahedra. J_2, J_{3a} and J_{3b} are the second and two inequivalent third neighbour couplings respectively (see Fig. 4.10). $J^{\text{eff}}_{\text{FCC}}$ for $LiInCr_4S_8$, $LiGaCr_4S_8$ and $CuInCr_4S_8$ is positive (effective FCC-AFM) while it is negative (ferromagnetic) for $CuInCr_4Se_8$. Most notably, a recent neutron scattering study on $LiGaCr_4S_8$, found both ferromagnetic nearest-neighbour exchange J_a and J_b, with anti-ferromagnetic further-neighbour exchange [83], qualitatively agreeing with the DFT based estimations in Ref. [22]. This material is understood to stablize in the effective AFM-FCC phase (discussed in previous section) where ferromagnetic tetrahedral clusters reside on an FCC lattice with emergent moments interacting via an anti-ferromagnetic exchange [21, 22, 83].

Since there are no materials in the universe which are modelled exactly with nearest-neighbour exchange and since these magnetic pyrochlore materials are very sensitive to

further-neighbour exchange [11, 42, 79], it is of considerable interest to undertake a systematic study of the effect of further-neighbor interactions in the breathing system to characterize the different ordered phases as well as to uncover interesting phenomena. Such studies would hopefully also encourage experimentalists to grow crystals of candidate materials to study them further.

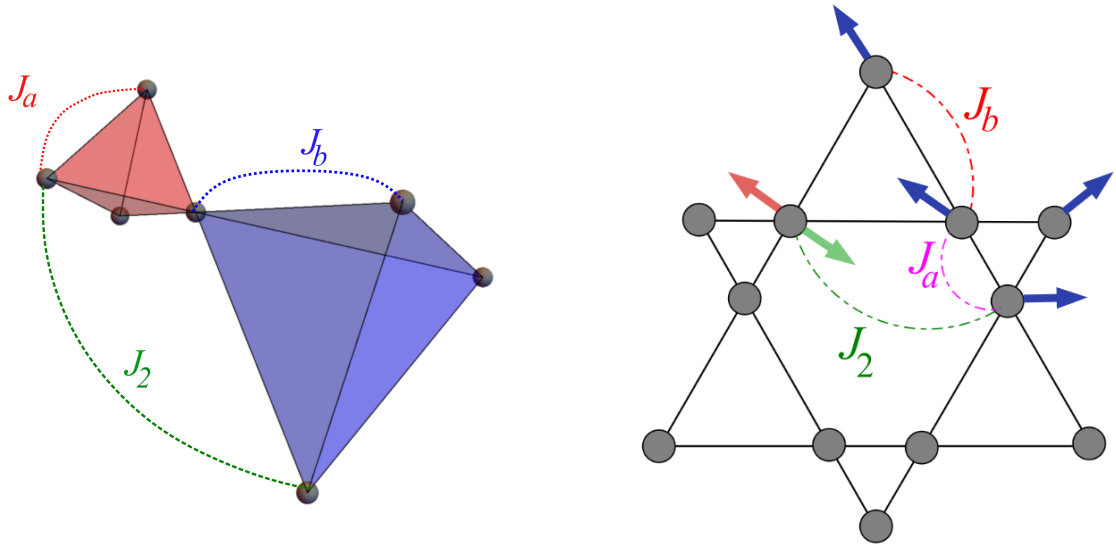

(a) (b)

Figure 4.11: Panel (a) shows the breathing pyrochlore with second nearest neighbour interactions, J_2. (b) shows the kagomé plane perpendicular to the $\langle 111 \rangle$ directions of the breathing pyrochlore (see Fig. A.3). This figure illustrates competing FM J_2 and J_b exchange (of comparable magnitudes) which, if J_2 wins, the spin will point along the "green" arrow while if J_b wins, will point along the "red" arrow.

4.3 Competition between J_2 and J_b

4.3.1 Motivation

The breathing pyrochlore system offers a unique opportunity to study the physics of highly frustrated spins on corner sharing tetrahedra of two different sizes interacting via J_a and J_b. Depending on the material, one may have J_a and J_b of opposite signs as well as differing magnitudes [21]. Most real materials additionally have non-zero further-neighbor interactions (see Fig. 4.10). Such further-neighbour interactions play a key role in lifting the

extensive ground state degeneracy of the pure AFM Heisenberg model on the pyrochlore lattice [11, 42]. For example, in the previous subsection, we discussed how (theoretically) ferromagnetic order is evaded in $LiInCr_4S_8$, $LiGaCr_4S_8$ with ferromagnetic J_a, J_b , due to the action of further-neighbour couplings [22].

In this section, we investigate the effect of adding a second nearest-neighbor coupling J_2 on the breathing pyrochlore. Fig. 4.11 shows the three interactions that are the subject of this study. The plane projected perpendicular to the $\langle 111 \rangle$ directions are alternating kagomé and triangular planes, wherein the interactions are showed in Fig. 4.11(b) (also see Fig. A.3). In Fig. 4.11(b), we illustrate the scenario when the J_a coupling is large and anti-ferromagnetic such that the vector sum of the classical spins on the small tetrahedra is 0, while J_b and J_2 are much smaller (compared to J_a) and of comparable magnitudes. Note how J_b and J_2 conspire to frustrate the system when both the couplings are simultaneously ferromagnetic or anti-ferromagnetic.

In the presence of such competing microscopic interactions, the system is expected to order into a variety of different phases depending on the magnitude and signs of J_b and J_2, analogous to the case of the $J - J_2$ model studied in Ref. [79]. In the following sections, we have undertaken a characterization of these classical ordered states at the mean field level and have investigated the high temperature spin-susceptibility of the different phases using mean field theory.

4.3.2 Methods

We start with the Heisenberg model on the breathing pyrochlore with next-nearest neighbor interactions J_2, given by.

$$\mathcal{H} = \sum_{\langle i,j\rangle_A} J_a\, A_{ij}\ (\mathbf{S}_i \cdot \mathbf{S}_j) + \sum_{\langle i,j\rangle_B} J_b\, B_{ij}\ (\mathbf{S}_i \cdot \mathbf{S}_j) + \sum_{\langle\langle i,j\rangle\rangle} J_2 C_{ij}\ (\mathbf{S}_i \cdot \mathbf{S}_j)\,. \tag{4.8}$$

J_a (J_b) is the coupling strength and A_{ij} (B_{ij}) the adjacency matrix of the small (large) tetrahedra (see Appendix A.4). $\langle i,j\rangle_A$ ($\langle i,j\rangle_B$) denotes pairs of spins in a small (large) tetrahedra[5]. The third sum takes pairs of second nearest neighbour spins (denoted by $\langle\langle i,j\rangle\rangle$) with interaction strength J_2 and C_{ij} is its usual adjacency matrix (see Appendix A.4). The rest of the discussion in this chapter utilizes mean-field theory (MF) developed in Chap. 2. According to the mean-field description [35, 36] (sign convention with positive J as AFM), the temperature below which the system orders is the MF critical temperature T_c, given by:

$$T_c = -\frac{\Lambda_{\min}(\mathbf{q})}{3}, \tag{4.9}$$

where $\Lambda_{\min}(\mathbf{q})$ is the minimum of the eigenvalues for all wavevectors $\mathbf{q}$. The symmetry related set of reciprocal wavevectors $\mathbf{q}$ at which this occurs are termed ordering wavevectors, $\mathbf{q_{ord}}$. We remind the reader that the wavevectors $\mathbf{q}$ are in units of $\frac{2\pi}{a}$ where a is the unit cell dimension. For the remainder of this presentation, we may refer to wavevectors $\frac{2\pi}{a}(pqr)$ as (pqr) (removing the $\frac{2\pi}{a}$ for convenience), especially while characterizing ordered phases but at times will use $\frac{2\pi}{a}(pqr)$ for clarity.

[5]Here i and j are just labelling all the sites in the pyrochlore lattice. In other sections of this thesis, i and j refer to FCC lattce site labels and are specified as such.

At criticality, different phases are expected to have different ordering wavevectors $\mathbf{q_{ord}}$, which characterize them [35]. The configuration of the spins in the system at $T \to T_c$ is completely controlled by these ordering wavevectors[6]. To find these $\mathbf{q_{ord}}$, we Fourier transform the adjacency matrices and diagonalize them to find their global minimum eigenvalues over all wavevectors $\mathbf{q}$ in the FBZ (see Appendix A.2). The Fourier transformed adjacency matrices are given in Appendix A.4 and may be computed via:

$$J^{cd}(\mathbf{q}) = \sum_{k,l} J^{cd}_{kl}\, e^{i\mathbf{q}\cdot(\mathbf{R}^c_k - \mathbf{R}^d_l)}, \tag{4.10}$$

where the sum is over all FCC sites k and l. c and d label the sublattices and $\mathbf{R}^c_k$ is the location of the spin in sublattice c of FCC site k. Here J^{cd}_{kl}, the adjacency matrix is given by:

$$J^{cd}_{kl} = J_a\, A^{cd}_{kl} + J_b\, B^{cd}_{kl} + J_2\, C^{cd}_{kl}. \tag{4.11}$$

We also utilize the spin structure factor formulae using mean field theory, developed in the text (Eq. (2.49)), reproduced here for convenience:

$$S(\mathbf{Q}) = \sum_{c,d,\alpha}^{4} \sum_{x,\mu}^{3} \left(\frac{U^{\alpha x}_{c\mu}(\mathbf{q}) U^{\alpha x}_{d\mu}(\mathbf{q})}{3 + \frac{\lambda^{\alpha}_{x}(\mathbf{q})}{T}} \right) e^{\mathbf{i}\mathbf{G}\cdot(\mathbf{r}_c - \mathbf{r}_d)}. \tag{4.12}$$

We remind the reader that in the above equation, $U(\mathbf{q})$ is the unitary matrix which diagonalizes $J(\mathbf{q})$ to $\lambda(\mathbf{q})$, which is the diagonal matrix with eigenvalue entries. The labels c,

[6] This is irrespective of whether the "strong" spin length constraint ($|\mathbf{S}|^2 = S^2$) utilized in the Luttinger-Tisza method is upheld [84]. The question of the ground state at $T = 0$ (as investigated using Luttinger-Tisza method in Refs. [79, 85, 86]) is complementary but distinct from the question of classical ordered phases at T_c. Our work deals with the latter case.

d refer to the sublattices and $\mathbf{r}_c$ is the position of the c-th sublattice inside the unit cell. μ labels the spin components and α, x index the eigenvectors and the eigenvalues. Here $\mathbf{Q} = \mathbf{q} + \mathbf{G}$ where $\mathbf{G}$ is a reciprocal lattice vector and $\mathbf{q}$ is a reciprocal vector in the FBZ. We rearrange Eq. (4.12) and define the quantity $F_\alpha^{\mu x}(\mathbf{Q})$ in the following way:

$$F_\alpha^{\mu x}(\mathbf{Q}) = \sum_c U_{c\alpha}^{\mu x}(\mathbf{q})\, e^{i\mathbf{G}\cdot\mathbf{r}_c}, \tag{4.13}$$

where $F_\alpha^{\mu x}(\mathbf{Q})$ is referred to as the magnetic unit cell form factor. Substituing the above equation in Eq. (4.12) and summing over μ, the structure factor $S(\mathbf{Q})$ is rewritten in the following way:

$$S(\mathbf{Q}) = \sum_{\alpha,x} \frac{|F_\alpha^x(\mathbf{Q})|^2}{3 + \frac{\lambda_x^\alpha(\mathbf{q})}{T}}. \tag{4.14}$$

At $T \to T_c$, only the critical (soft)[7] modes will contribute significantly. Thus, we present $S(\mathbf{Q})$ plots corresponding to the reduced temperature characterized by $\tau = \frac{T - T_c}{T_c}$. The structure factor at criticality will read:

$$S(\mathbf{Q}) = \sum_\theta \frac{|F^\theta(\mathbf{Q})|^2}{3 + \frac{\lambda^\theta(\mathbf{q})}{T}}, \tag{4.15}$$

where the θ labels the critical modes. Just computing the numerator of the above equation, we obtain the sum of the magnetic unit cell form factor squared for just the critical modes. This quantity at the MF ordering wavevectors $\mathbf{q}_{\text{ord}}$, denoted by f, has been further

[7]Critical or soft modes refer to the eigenmodes of $J(\mathbf{q})$ labelled by x, α here, which correspond to the branches in which the global minimum of the eigenvalues exist. These are the modes which contribute maximally to the structure factor intensity at $T \to T_c$.

computed to differentiate between phases in the following sections. f is given by:

$$f = \sum_{\theta} |F^{\theta}(\mathbf{q}_{\text{ord}})|^2. \tag{4.16}$$

This quantity is just the numerator of Eq. (4.15) and is a number. It characterizes the intensity of the structure factor at the ordering wavevectors $\mathbf{q}_{\text{ord}}$, without considering the modulation of the eigenvalues in the denominator of Eq. (4.15).

4.3.3 Implementation

Thus, the basic implementation scheme is to find the ordering wavevector $\mathbf{q}_{\mathbf{ord}}$ as well as the global minimum eigenvalue, $\Lambda_{\text{min}}(\mathbf{q})$. This implies that one has to mesh over all $\mathbf{q}$ in the Brillouin Zone (see Appendix A.2), find the global minimum of the eigenvalues and obtain $\mathbf{q}_{\mathbf{ord}}$ for each tuple, J_b and J_2. We obtain all symmetry related $\mathbf{q}_{\text{ord}}$ and refer to only one of these for the rest of the presentation. This has been done numerically using Python's numpy module [50] and using Scipy's optimization modules [87]. The modules allow an easy way to implement the following minimization algorithms:

- Global minimization routine by brute force sampling over the BZ
- Nelder-Mead method also known as the downhill simplex method [88, 89, 90].
- Modified Powell algorithm (MP) [91].
- Truncated Newton algorithm (TN) [92].

- Conjugate Gradient (CG) method/Fletcher Reeves algorithm in pp. 120 - 122 of Ref. [92].
- BFGS (Broyden, Fletcher, Goldfarb and Shanno algorithm) pp. 136 in Ref. [92].
- Limited memory BFGS: L-BFGS [93]
- COBYLA (Constrained Optimization by Linear Approximation method) [94].

Further details may be found in Appendix B. The above algorithms are given an initial guess point around which they finds the minima. We implemented all the above algorithms such that they work in a sequence to save processing times[8]. The implementation scheme is briefed below:

1. A mesh of $\mathbf{q}$-vectors in the FBZ is generated.
2. The global minimization scheme outputs wavevectors $\mathbf{q}_{\text{old}}$ corresponding to the global minimum (this is relaxed a bit as explained in the next section).
3. The wavevectors from above $\mathbf{q}_{\text{old}}$, are used as guess points for the Nelder-Mead method. This generates new wavevectors $\mathbf{q}_{\text{new}}$. The eigenvalues (in the minimum branch) corresponding to $\mathbf{q}_{\text{new}}$ is checked against $\mathbf{q}_{\text{old}}$. If the eigenvalues corresponding to $\mathbf{q}_{\text{new}}$ is smaller, $\mathbf{q}_{\text{new}}$ is the output ordering wavevectors at T_c.
4. If the Nelder-Mead method does not work or stagnates for too long, $\mathbf{q}_{\text{old}}$ is then used an input for the modified Powell algorithm.

[8]Trying to simultaneously use all the algorithms and comparing the results is quite time consuming. Instead one algorithm is utilized at a time.

5. If this does not work then the next algorithm in the sequence is used with initial guess point $\mathbf{q}_{\text{old}}$.

In practice, we note that only in very rare cases, the Nelder-Mead method will not work. One has to provide new parameters (called adaptive parameters which modify how the simplex moves) in the Nelder-Mead algorithm for three dimensional problems such as in this work. The use of adaptive parameters [90] makes the method more accurate for 3D systems of interest (for the same number of simplex steps).

In general, we observed that the derivative based methods (TN, CG, BFGS, L-BFGS) fail near points of inflection. The Nelder-Mead method stagnates at local extrema and the modified Powell algorithm may have issues on surfaces with discrete peaks. Moreover, one must be aware of the possibility of stagnation at a local minimum. This indicates that the initial guess point given to these algorithms must be close to the global minima. Thus, in our work we have first implemented a global minimization of $\mathbf{q}$-vectors in the FBZ and these $\mathbf{q}$s then function as our guess points for the above algorithms.

Further, we also implemented a valley-tracking algorithm, which was useful in exposing certain subtleties of the phase diagram such as tracking the minima and $\mathbf{q}_{\text{ord}}$ of the multiply modulated spiral phase (MMS) which stabilizes in only a small region of the phase diagram discussed below. The basic scheme is:

- Find ordering wavevectors $\mathbf{q}_{\text{init}}$ for particular J_2 and J_b.
- Vary the exchange parameters (either J_2, J_b or both) by small number Δ.

- Utilize $\mathbf{q}_{\text{init}}$ as a guess point for the Nelder-Mead method at new J_2 and/or J_b to find ordering wavevectors for the new exchange parameters $\mathbf{q}_{\text{new}}$.

- Vary the exchange parameters again by a small amount and use $\mathbf{q}_{\text{new}}$ as new guess points and repeat.

In this way we may continuously track the global minima valley as it modulates with the exchange parameters, J_2 and J_b. The phase diagrams (Fig. 4.12 and Fig. 4.16) were constructed via multiple samples of parameters, J_2 and J_b, which ranged from 50^2 samples in usual runs to 150^2 samples to investigate subtler features of the phase diagram (using Python's numpy [50] and Scipy [87] modules). Three complementary approaches were used to find the ordering wavevetors for a given set parameters J_2 and J_b, detailed below:

- The first approach being a brute force sampling over $\mathbf{q}$-space in the FBZ with 70^3 points.

- The second approach, which yields better results, consists of sampling over 25^3 points (in the FBZ) and sorting the wavevectors by their corresponding eigenvalues (of $J(\mathbf{q})$). After sorting, we choose the wavevectors corresponding to the global minima E_{min}, as well as the wavevectors corresponding to eigenvalues in the range $E_{\text{min}} \pm \delta$, where δ is set to 10^{-10}. This δ value might seem small but near the phase boundaries, many different eigenmodes are competing which may have local minima very near the global minima. After these wavevectors have been identified, they are sent as initial input to the minimization algorithms developed above and yield better results as compared to the brute force approach.

- The valley-tracking algorithm was used to investigate the $(\frac{1}{2}\frac{1}{2}\frac{1}{2})$, the multiply modulated spiral phase and their boundaries.

In this section, we set out the basic implementation scheme to study the various ordered phases in the J_a-J_b-J_2 model. We also provided details of how the phase diagrams were obtained. In the next section, we introduce the phase diagrams, briefly discuss previous studies and then jump right into the findings from the phase diagrams.

4.4 Mean Field Phase Diagram J_b vs J_2

In this section, we provide details of the two obtained MF phase diagrams. The first phase diagram referred to as PD_1, has J_a set to unity and anti-ferromagnetic (positive sign in our conventions) while varying J_b and J_2 from $[-J_a, J_a]$. In the second phase diagram (PD_2), J_a is set to unity and is ferromagnetic (negative sign in our convention) while J_b and J_2 are varied from $[-J_a, J_a]$. Cuts of PD_1 and PD_2 at certain lines, such as $J_a = +1; J_b = -1$ (in PD_1) and $J_a = -1; J_b = +1$ (in PD_2) with varying J_2, will describe the same physics since swapping the labels a and b do not change the system or its physics (note that the bond length ratio $\gamma = 1$ for both PD_1 and PD_2).

Certain sections of the ground state phase diagrams have been previously studied in the literature, namely the non-breathing limits $J_a = J_b = \pm 1$ vs J_2 [79, 85, 86], where their respective phase diagrams were studied and phases were characterized via Luttinger-Tisza analysis and iterative minimization procedures. The $J - J_2$ with $J_2 < 0$ (FM) model has been studied and found incommensurate ($qq0$) order [95, 96] and multiple-**q**

incommensurate spirals [97]. Studies with further-neighbor (J_{3a}, J_{3b}, etc) interaction were done as early as the year 1991, in the $J_1 - J_2 - J_3 - J_4$ Heisenberg model in Ref. [35] (where they considered $J_{3a} = J_{3b}$) and much much more recently by Conlon *et al.* [42] where they showed the supression of pinch-points on addition of weak further-neighbour interactions. The J_{3a} interaction (see Fig. 4.10) has been noted to result in similar effects as the J_2 interaction with a negative sign [11, 22, 42] and similar phases are expected to stabilize with a J_{3a} interaction, which has to be further investigated.

However, to the best of our knowledge this is the first study of the breathing pyrochlore system with $J_a \neq J_b$ and varying J_2. In particular, the oppositely signed J_a, J_b quadrants (defined below) of the phase diagrams had not yet been investigated before this work. On studying the phase diagrams, we uncover phase competition, a possibly unreported phase with ordering wavevector of the form $(qq0)$ and a phase boundary with line degeneracies along the (qqq) directions.

In the following sections, we discuss the obtained phase diagrams by referring to their quadrants. In both phase diagrams, the first quadrant is J_b, $J_2 > 0$, the second quadrant is $J_b > 0$, $J_2 < 0$, the third quadrant is J_b, $J_2 < 0$ and the fourth quadrant is $J_b < 0$, $J_2 > 0$.

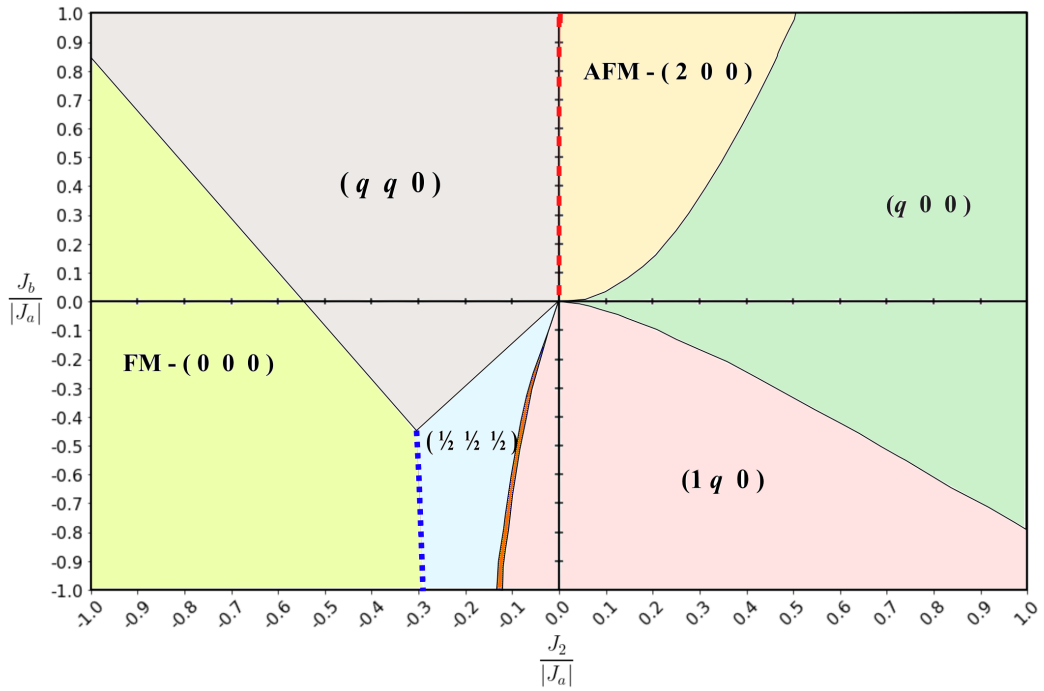

Figure 4.12: Phase diagram PD_1 with $J_a = +1$ (AFM) and variation between J_b (y-axis) and J_2 (x-axis). The phases are characterized by $\mathbf{q}_{\mathbf{ord}}$ as described in the text. The red dashes along $J_b > 0$, $J_2 = 0$ is the Coulomb phase described above. The $(qq0)$ phase along $J_a = J_b = +1$ in the second quadrant with $J_2 < 0$ has been called the Kawamura phase [79, 95, 97]. In the third quadrant with $J_b < 0$ and $J_2 < 0$ the blue dotted line is the phase boundary between the $(\frac{1}{2}\frac{1}{2}\frac{1}{2})$ phase and the FM phase where there are line degeneracies along the (qqq) directions. The orange strip (in the same quadrant) is the heretofore unreported $(qq0)$ phase and is sandwiched between the $(\frac{1}{2}\frac{1}{2}\frac{1}{2})$ phase and the effective AFM-FCC phase and becomes thinner as the magnitude of J_b gets smaller. This strip has been noted to exist upto $J_b = -0.05$, but will require very high resolution in sampling over J_2 and J_b to investigate further. This phase diagram has been constructed using multiple runs of varied resolutions over the parameters J_2 and J_b. Each run consisted of either brute force sampling over the BZ with 70^3 points or sampling over 25^3 points and using the minima of that process as an input for the standard minimization algorithms to find the global minimum eigenvalue.

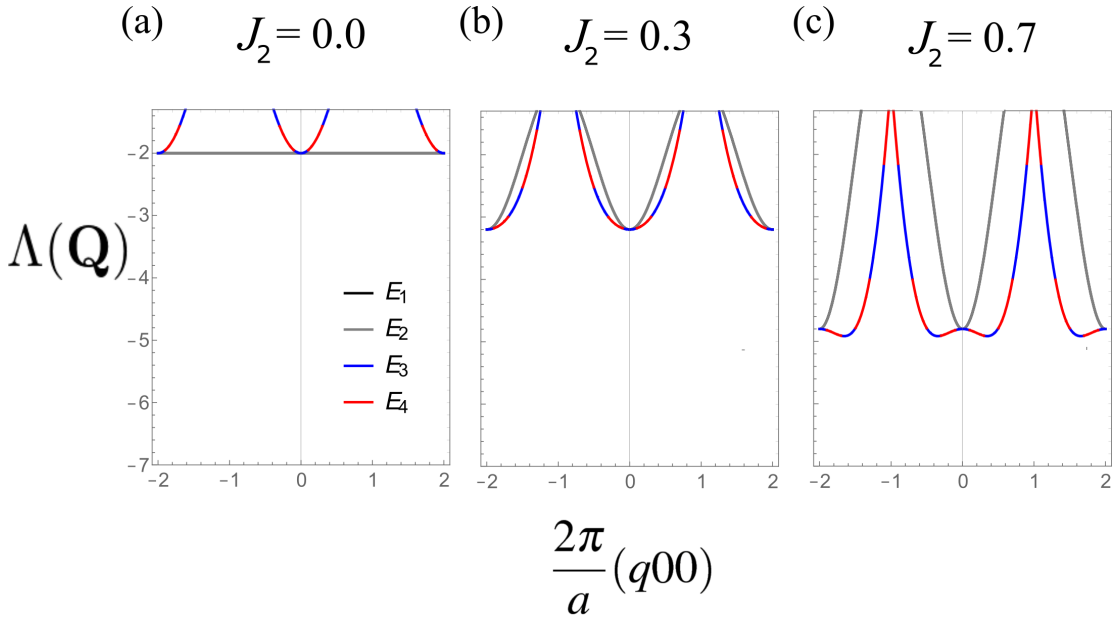

Figure 4.13: Eigenvalues $\Lambda(\mathbf{Q})$ along $\mathbf{Q} = \frac{2\pi}{a}(q00)$ (q along x-axes). Here, $J_a = J_b = 1$ and J_2 is AFM. (a) shows the flat bands in the Coulomb phase. (b) shows minima at $q = 2, 0, -2$ and is in the coplanar $\mathbf{k} = \mathbf{0}$ phase. (c) shows 2nd and 3rd eigenvalues develop deeper minima at ordering wavevectors $\frac{2\pi}{a}(q00)$ centered on $\frac{2\pi}{a}(000)$, signifying the planar spiral phase [79, 85]

4.4.1 $\mathbf{PD_1}$: $\mathbf{J_a = +1}$ (AFM) and $\mathbf{J_b}$ vs $\mathbf{J_2}$

The Heisenberg model on the pyrochlore lattice with AFM interactions J_a and J_b, as mentioned above, has two degenerate flat bands in $\mathbf{q}$-space where the minimum eigenvalue is given by $|J_a + J_b|$. If J_a and J_b are oppositely signed, then the effective AFM-FCC (see Fig. 4.8) phase with line degeneracies along wavevectors of the form $\frac{2\pi}{a}(q, 1, 0)$ ensues. If both J_a and J_b are FM, the FM phase ensues where the minima are in the dispersive bands and the flat bands reside at higher energies (see Fig. 4.5). Addition of J_2 into the mix leads to a variety of new phases with both FM and AFM J_2, causing dispersion in the flat bands

(see Fig. 4.13 and Fig. 4.14). The dispersion results in the selection of (soft) critical modes at the mean field T_c, which results in an ordered state characterized by the form of the ordering wavevectors $\mathbf{q_{ord}}$ for which one or more of the eigenvalues are a global minimum.

In this section, we discuss PD_1 (see Fig. 4.12) with AFM $J_a = +1$. When $J_a = 1$, $J_b > 0$ and $J_2 = 0$, one finds a Coulomb spin liquid [11, 17, 18] phase with extensive groundstate degeneracy which shows up in our mean field analysis in the form of degenerate flat **q**-independent eigenbands in the FBZ.

In the **first quadrant**[9] with AFM J_2 we find a phase with ordering wavevectors of the form $\frac{2\pi}{a}(2,0,0)$ (see Fig. 4.13) extending upto $J_2/J_a = 0.499$ along $J_a = J_b = +1$. This phase has been studied by Lapa *et al.* [85, 86] and more recently by Iqbal *et al.* [79] who find that the spins on each sublattice are ordered ferromagnetically. However, the spins on different sublattices are not parallel and the spins in each tetrahedra vectorially sum up to zero. This phase is dubbed the $\mathbf{k} = \mathbf{0}$ phase. Intuitively, the AFM J_2 coupling may be viewed as having the same effect as in FM J_{3a} which couples the same sublattices ferromagnetically. This may be seen in the $S(\mathbf{Q})$ as subdominant peaks at the $\frac{2\pi}{a}(1,1,1)$ [79] (see panels (a),(b) of Fig. 4.19). This phase extends further into the phase diagram in the first quadrant.

For $J_2/J_a > 0.5$, we find the planar spiral (PS) phase [79, 85, 86] with ordering wavevectors of the form $\frac{2\pi}{a}(q,0,0)$ with incommensurate q (see Fig. 4.13). On the $J_a = J_b$ line, this q evolves from 0 to 0.46. In the first quadrant, this phase extends downwards where the wavevector component q increases with increasing J_2. This phase extends into the fourth

[9] We have used boldface to emphasize the different quadrants and bring the attention of the reader quickly to the sections of interest.

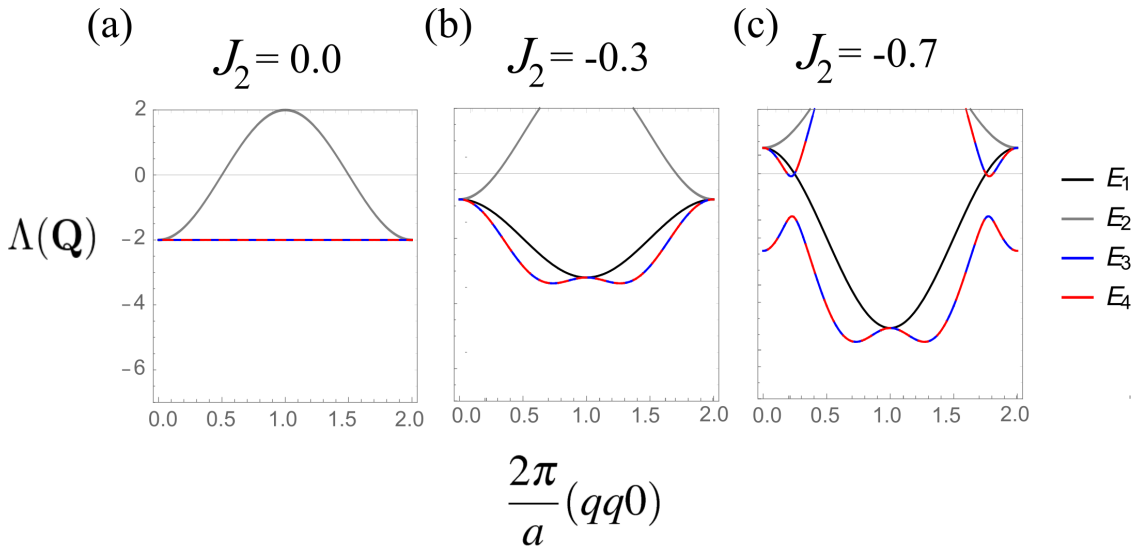

Figure 4.14: Eigenvalues $\Lambda(\mathbf{Q})$ along $\mathbf{Q} = \frac{2\pi}{a}(qq0)$ (q along x-axes). Here $J_a = J_b = 1$ and J_2 is FM. (a) shows the flat bands in the Coulomb phase. (b) and (c) show the development of broad minima centering around $\frac{2\pi}{a}(110)$ and taking incommensurate values near $\frac{2\pi}{a}(0.73*, 0.73*, 0)$. The star denotes that they are real numbers with truncated decimals.

quadrant where the opposite trend takes place where q decreases with increasing J_2. As we move from the $\mathbf{k} = \mathbf{0}$ phase to PS, the peak at (200) separates into two peaks, one of which is inside the FBZ and of the form $(q00)$ (Fig. 4.13(c)). This is observed in $S(\mathbf{Q})$ (see panels (c), (d) of Fig. 4.19) and in Fig. 4.13 where the minimum of the eigenbands at (000) morph into two minima centred on (000) at wavevectors of the form $(\pm q00)$.

In the **second quadrant** of PD_1 (Fig. 4.12) with $J_2 < 0$, we find a $\frac{2\pi}{a}(q, q, 0)$ ordered state which has been extensively studied in the literature [79, 86, 95, 96, 97] and dubbed the Kawamura Phase. It is a superposition of spirals with the ordering wavevectors and approximately fulfils the constraint of spins summing to zero in each tetrahedron [79]. For small FM J_2, a partially ordered metastable collinear phase at finite temperatures was found using Monte Carlo simulations by Chern *et al.* [96]. This phase was found to transi-

tion to the Kawamura phase at low temperatures. In our analysis, we find incommensurate $\frac{2\pi}{a}(q, q, 0)$ which evolves from $q = 0.741$ to $q = 0.727$ along $J_a = J_b = +1$. This phase also extends further in the phase diagram and approximate modulation of q is noted from 0.7 to 0.74. The eigenvalues has further minima at incommensurate peaks/valleys near $\frac{2\pi}{a}(5^*/4, 5^*/4, 0)$ [79]. These so called satellite peaks in Ref. [96] were attributed to finite size effects but are actually present in the eigenspectrum. This may be noted as the twin minima in Fig. 4.14 and peaks at $(qq0)$ in panels (a) and (b) of Fig. 4.20. It would be interesting to consider if the exotic phase described in Ref. [96] extends to the breathing regime and the third quadrant. We also find the ferromagnetic phase (described in previous sections) with ordering wavevectors $\frac{2\pi}{a}(0, 0, 0)$ in the second quadrant of the phase diagram.

In the **third quadrant**, we find five distinct phases including the previously described Kawamura phase, the effective AFM-FCC phase with $\frac{2\pi}{a}(q, 1, 0)$ wavevectors and the ferromagnetic phase. We also find an ordered phase characterized by commensurate[10] ordering wavevectors $\frac{2\pi}{a}(\frac{1}{2}, \frac{1}{2}, \frac{1}{2})$, which has been dubbed the Cubooctahedral stack [79, 85, 86]. However, we note that this name has been given to a $\frac{2\pi}{a}(\frac{1}{2}, \frac{1}{2}, \frac{1}{2})$ ordered state in the $J_a = J_b = -1$ line in PD_2 (see Fig. 4.16) and thus we refer to it primarily with $(\frac{1}{2}, \frac{1}{2}, \frac{1}{2})$. In this phase, spins in the kagomé layer point towards the 12 vertices of the Cuboctahedron and realizes a 12 sublattice magnetic structure [79, 85, 86]. Similar phases have been found [35] and discussed in the literature such as by Fritsch *et al.* [98] where elastic neutron scattering on the non-breathing compound, $Tb_2Ti_2O_7$, noted peaks at $\frac{2\pi}{a}(\frac{1}{2}, \frac{1}{2}, \frac{1}{2})$

[10] In our numerical calculations, we find each wavevector component as numbers which are exactly 1/2, upto machine precision

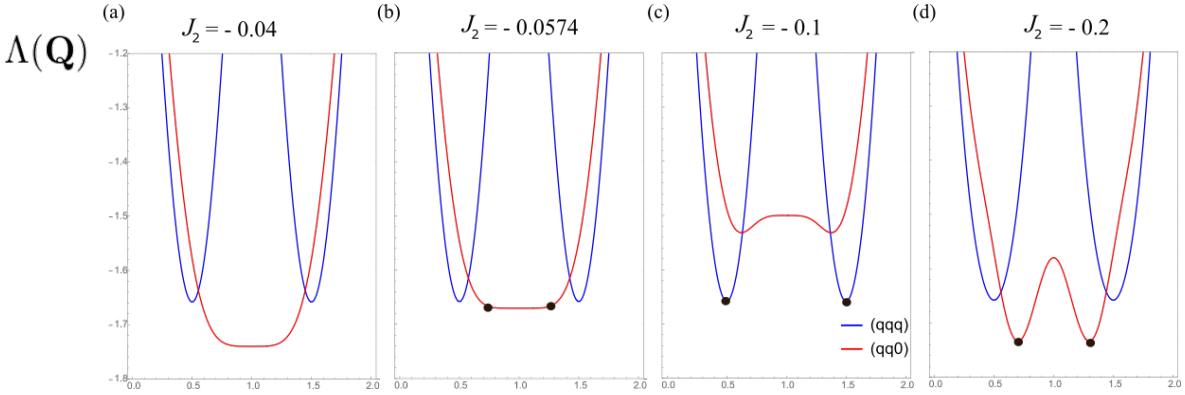

Figure 4.15: Figure shows minimum eigenvalues $\Lambda(\mathbf{Q})$ along $\mathbf{Q} = \frac{2\pi}{a}(qq0)$ and $\mathbf{Q} = \frac{2\pi}{a}(qqq)$. Here $J_a = 1$,$J_b = -0.3$ and J_2 is FM. The x-axis is just the numerical value of q. (a) shows a broad minima from $q = -0.5$ to $+0.5$. This is the $(q10)$ phase. In (b), the blackdots show minima at wavevectors of the form $(qq0)$ which is the unreported phase. Panel (c) shows the sharp minima at ordering wavevectors $\frac{2\pi}{a}(\frac{1}{2}, \frac{1}{2}, \frac{1}{2})$ and then (d) shows the resurgence of the $(qq0)$ peak in the Kawamura phase (compare with Fig. 4.12).

and symmetry related wavevectors. Fig. 4.15(c) illustrates this case and shows minima in the eigenvalues at $(\frac{1}{2}, \frac{1}{2}, \frac{1}{2})$. The peaks at $(\frac{1}{2}, \frac{1}{2}, \frac{1}{2})$ may be noted in the structure factors (see panels (c) and (d) of Fig. 4.20). As the magnitude of FM J_2 increases, the Kawamura phase is stablized (see Fig. 4.15(d)) for moderately ferromagnetic J_b. Further increasing the magnitude of J_2, the FM (000) phase ensues.

Sandwiched between the effective AFM-FCC $(q10)$ phase and the $(\frac{1}{2}, \frac{1}{2}, \frac{1}{2})$ phase, we find a heretofore unreported phase with ordering wavevectors $\frac{2\pi}{a}(q, q, 0)$, where q may approximately take values between 1 and 0.8. This phase has been noted to have vanishingly small width upto $J_b/|J_a| = 0.05$. Interestingly, the same phase extends into PD_2 (see Fig. 4.16) with $J_a = -1$. Here, we see an approximate symmetry in the regions of PD_1 (Fig. 4.12) given by $J_a = +1; J_b < 0; J_2 \in [0, -0.2]$ and PD_2 (Fig. 4.16) parameterized by

$J_a = -1; J_b > 0; J_2 \in [0, -0.2]$ in the second quadrant of PD_2. This symmetry should be investigated more to find out why for this range of values of J_2, only the fact that J_a and J_b are oppositely signed is enough to guarantee this approximate symmetry. The structure factors for this phase is provided in panels (c) and (d) of Fig. 4.21. The **fourth quadrant** hosts the above mentioned $(q00)$ and effective AFM-FCC $(q10)$ phase. At this point we jump into the next phase diagram PD_2.

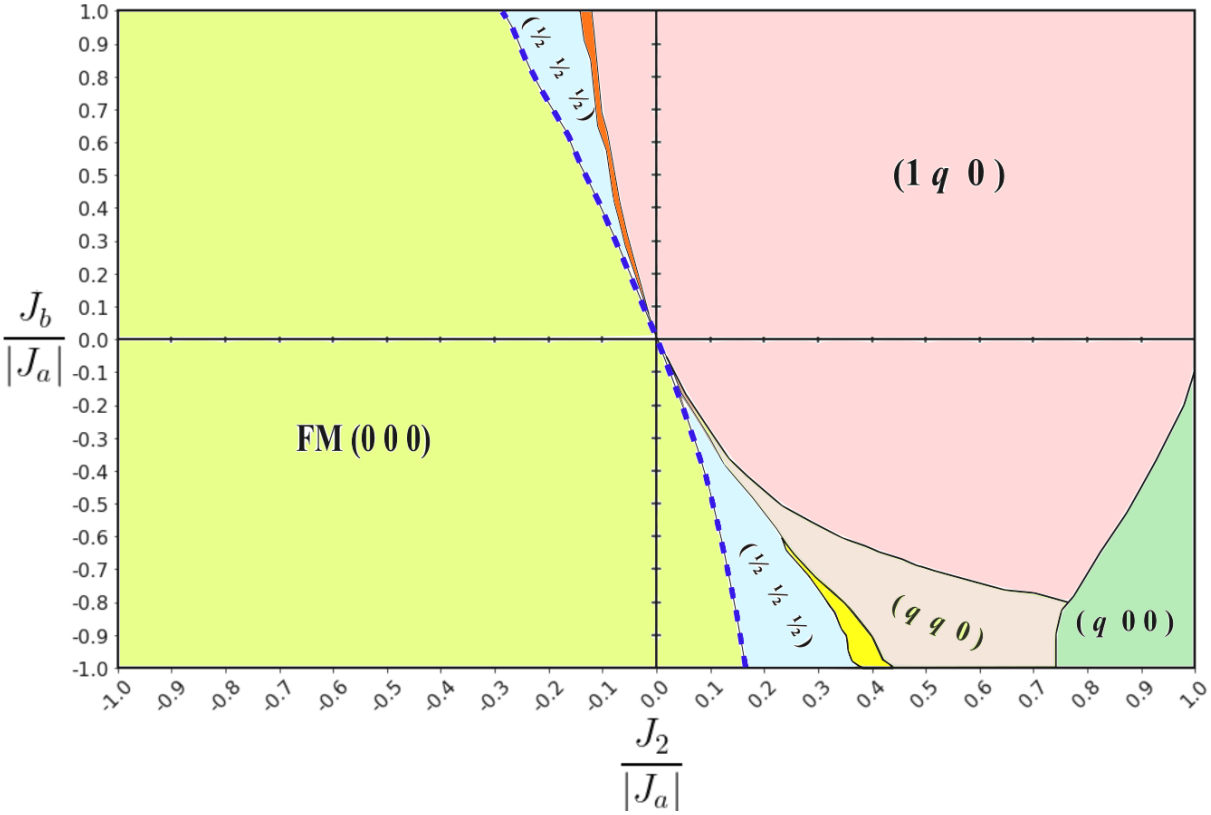

Figure 4.16: Phase diagram with $J_a = -1$ (FM) and variation between J_b (y-axis) and J_2 (x-axis). The first quadrant i.e. J_b, $J_2 > 0$ (AFM) and the third quadrant with J_b, $J_2 < 0$ (FM) is entirely dominated by one phase, the FM $(0, 0, 0)$ phase for the latter and the Effective AFM-FCC phase with $(q10)$ ordering wavevectors for the former. In the second quadrant ($J_2 > 0$, $J_b < 0$), the orange strip is the unreported $(qq0)$ phase described in the text which is observed to be sandwiched between the $(\frac{1}{2}\frac{1}{2}\frac{1}{2})$ phase and the $(q10)$ phase and becomes thinner as the magnitude of J_b becomes smaller. This strip has been noted to exist upto $J_b = 0.05$ but will require higher resolution in sampling over J_2 and J_b to investigate further. In the fourth quadrant with $J_b < 0$ and $J_2 > 0$, we find the double twist (DT) phase with $(qq0)$ type wavevectors [79, 85] and the $(\frac{1}{2}\frac{1}{2}\frac{1}{2})$ phase. Sandwiched between the two is the multiply modulated spiral (MMS) phase with (qqp) type ordering wavevectors, which is shown here in bright yellow. The DT phase has been observed to extend upto $J_b = -0.05$ while the MMS phase straddles along the DT phase but becomes vanishingly thin upto $J_b = -0.5$, at the resolution studied. This phase diagram has been constructed using multiple runs of varied resolutions over the parameters J_2 and J_b. Each run consisted of either brute force sampling over the BZ with 70^3 points or sampling over 25^3 points and using the minima of that as an input for the standard python minimization algorithms to find the global minimum eigenvalue.

4.4.2 PD_2: $J_a = -1$ (FM) and J_b vs J_2

Whilst in the previous phase diagram, we held the J_a interactions as dominant and AFM, here we investigate the opposite case. J_a is set to unity and is ferromagnetic which results in a large part of the phase diagram (Fig. 4.16) being covered with the FM (000) phase. This includes entirety of the **third quadrant**, which is expected since all the interactions are ferromagnetic. The majority of the **second quadrant** is also dominated by the FM phase. The subtler details of the second quadrant are discussed below.

The **first quadrant** of PD_2 is entirely the effective AFM-FCC phase with line degeneracies along $(q10)$. This is expected since this phase is a consequence of oppositely signed interactions in J_a and J_b which happens in the first quadrant ($J_a = -1,\ J_b > 0; J_2 > 0$). The anti-ferromagnetic J_2 and J_b coupling here can be intuitively seen to connect the emergent tetrahedral clusters (due to large FM J_a) and stablizes effective moments on the ferromagnetic tetrahedra (residing on a FCC lattice) interacting with each other via AFM exchange. This has been illustrated in Fig. 4.17(b)

A very small FM J_2 approximately around -1.3 is enough to destablize the degenerate modes along $(q10)$ in the effective AFM-FCC phase. Intuitively, once J_a is large and FM, emergent clusters form in the ferromagnetically interacting tetrahedra. J_b and J_2 then control how the emergent clusters interact. When J_2 is ferromagnetic and J_b is anti-ferromagnetic, there is frustration and a small $J_2 \approx -1.35$ suffices to stablize ferromagnetic order. This is illustrated in Fig. 4.17(a).

In between the $(q10)$ and the FM phase we find and categorize three distinct regions in the **second quadrant** (see Fig. 4.16). In particular, increasing the magnitude of ferro-

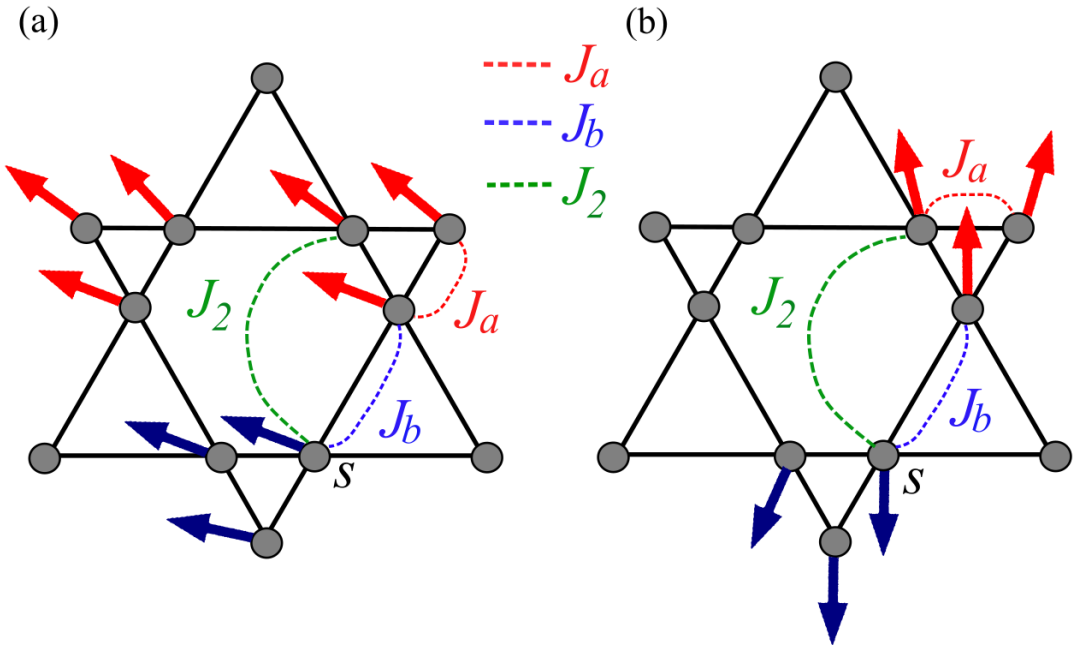

Figure 4.17: In both these figures, J_a is large and ferromagnetic resulting in the clustering of effective moments at the ferromagnetically interacting tetrahedra (small ones in this case). Both these figures illustrate how J_b and J_2 serve as interactions between the effective clusters. On the left panel (a), we see FM J_2 and J_b will lead to the FM ordered state being stablized where the moments point in the same direction. On the right panel (b), we illustrate how a AFM J_2 coupling serves to enhance the effective AFM interaction between the clusters especially in the presence of AFM J_b and stablizes the $(q10)$ phase. Spins are slightly canted to show the existence of fluctuations at temperatures T below the overall energy scale of the problem but above the transition at T_c i.e. $J_a > T > T_c$.

magnetic J_2, we enter the (q^*q^*0) phase at approximately $J_2 = -0.129$ ($J_a = -1$, $J_b = +1$) where $q^* \approx 0.8869$ and evolves to $q^* \approx 0.8318$ at $J_2 \approx -0.134$ wherein the $(\frac{1}{2}\frac{1}{2}\frac{1}{2})$ phase is realized. This is the same hitherto unreported $(qq0)$ phase as found above, in Fig. 4.12, since it continuously connects the second quadrant of Fig. 4.16 to the third quadrant of Fig. 4.12 via a common line along $J_a * J_b = -1$ where the labels may be flipped without changing the physics.

In the **second quadrant**, we observe that this $(qq0)$ phase extends all the way upto $J_b \approx 0.05$ and this strip becomes vanishingly thin as we follow it towards the origin. The $(\frac{1}{2}\frac{1}{2}\frac{1}{2})$ phase also extends towards the origin and the width becomes quite small and we noted (while investigating the phases near the origin with more resolved $\mathbf{q}_{\text{ord}}$ searches) that the $(\frac{1}{2}\frac{1}{2}\frac{1}{2})$ extend atleast upto $J_b \approx \pm 0.005$ in the **second and fourth quadrants**.

In the **fourth quadrant** of Fig. 4.16, we find six distinct regions. Following the x-axis i.e. $J_a = -1$, $J_b = -1$ and varying $J_2 > 0$ we find a ferromagnetic phase extending upto $J_2 \approx 0.171$. This FM phase extends further up all the way to the origin as magnitude of J_b becomes smaller. For $J_2 > 0.171$, a $(\frac{1}{2}\frac{1}{2}\frac{1}{2})$ phase is stablized and extends towards the origin. We noted that this phase exists all the way upto $J_b \approx \pm 0.005$ near the origin but the width of the strip becomes quite thin. The $(\frac{1}{2}\frac{1}{2}\frac{1}{2})$ phase extends all the way upto $J_2 \approx 0.375$, where in, the multiply modulated spiral (MMS) phase begins. Lapa *et al.* [85, 86] found that this transition takes place at $J_2 \approx 0.4$ and Iqbal *et al.* [79] finds it at $J_2 \approx 0.3965$. This difference is attributed to much higher resolution in sampling of J_2 and J_a. Further, Iqbal [79] finds ordering wavevectors of the form $\frac{2\pi}{a}(\frac{3}{4}, \frac{1}{4}, \frac{1}{2})$ and Lapa [86] in their less resolved analysis find wavevectors of the form $\frac{2\pi}{a}(\frac{3^*}{4}, \frac{1^*}{4}, \frac{1}{2})$ and $\frac{2\pi}{a}(\frac{3}{4}, \frac{3}{4}, 0)$. Iqbal's work utilized 32^3 and Lapa's work utilized 8^3 sample points in $\mathbf{q}$-space. Our analysis with

upto 70^3 points and 25^3 points with the standard minimization algorithms (see Appendix B) and valley-tracking[11] reveals that the ordering wavevector in the MMS phase has the form, (ppq). As J_2 increases, the ordering wavevectors in the $(\frac{1}{2}\frac{1}{2}\frac{1}{2})$ phase change in a characteristic way while entering the (ppq) regime. Two of the components in $(\frac{1}{2}\frac{1}{2}\frac{1}{2})$ start increasing towards 0.7 while the other one starts decreasing. Typical ordering wavevectors evolve in the fashion $(\frac{1}{2}\frac{1}{2}\frac{1}{2})$ to $(0.6^*\,0.6^*\,0.3^*)$ to $(0.7^*\,0.7^*\,0)$. We note, for a few cases, the eigenvalues corresponding to (ppq) wavevectors and the ones proposed in previous works [79, 86] have a difference of less than 0.15% with the minima being the eigenvalues corresponding to wavevectors that we found. This phase is observed to extend atleast upto $J_b \approx -0.6$ and becomes vanishingly small beyond that. The structure factor for MMS may be found in Fig. 4.22. On the $J_a = J_b = -1$ line one finds the MMS ordering wavevectors $(0.7^*, 0.7^*, 0)$ at $J_2 \approx 0.4307$ increasing which, we find the double twist phase (DT).

This transition from the MMS to the DT phase has been found in Ref. [79] as $J_2 = 0.475$, and in Ref. [86] as $J_2 = 0.43$. The DT phase has been studied in the literature [79, 86] and is understood to be a composite of two spirals with the same form of the ordering wavevector $(qq0)$. We also find ordering wavevectors of the form $(qq0)$ in this regime where $q \approx [0.7, 0.8]$. We noted that the DT phase extends into the phase diagram (towards the origin) and exists upto $J_b = -0.005$ and has relatively more width that the $(qq0)$ phase in the **second quadrant** of PD_2. Further increasing J_2 upto $J_2 = 0.7677$, the planar spiral phase with wavevectors of the form $(q00)$ is stabilized for the remainder of the phase

[11]The valley-tracking algorithm is good for tracking the minimum eigenvalues and the corresponding ordering wavevectors as J_b and J_2 are varied. However, if minima develop (on varying J_b and J_2) away from the wavevectors being tracked, the algorithm will not pick this up. Thus, we rechecked the ordering wavevectors found via valley-tracking with those found via global searches and by utilizing the standard minimization algorithms described in the text.

diagram. Here q varies approximately from 1.11 to 0.839 as J_2 is increased to +1. The planar spiral phase extends into the phase diagram and vanishes when the magnitude of J_b is small while J_2 is large and AFM (see Fig. 4.16).

This is a first study on the **third** and **fourth quadrants** of PD_1 (Fig. 4.12) and the **first** and **second quadrants** of PD_2 (Fig. 4.16). Since we found three disconnected regions with ordering wavevectors of the form $(qq0)$, we hypothesize that the previously unreported $(qq0)$ phase that we found, is distinct from both the Kawamura and the double twist phase. However, at the MF level, this distinction is not very apparent. Whereas the Kawamura phase has ordering wavevectors of the form $(qq0)$ with $q \in [0.7, 0.74]$, the DT phase has $(qq0)$ with approximate $q \in [0.7, 0.8]$ and the unreported $(qq0)$ phase with $q \in [0.8, 1.0]$.

Computing the value of the magnetic form factor squared f (see Eq. (4.16)) at criticality, and at the ordering wavevector $\mathbf{q_{ord}}$, lends approximate but ultimately inconclusive support to the above claim. f takes the form:

$$f \propto \sum_{\alpha} |F^{\alpha}(\mathbf{q_{ord}})|^2. \tag{4.17}$$

Here α runs over the critical modes and $F(\mathbf{q}_{\text{ord}})$ is the "critical" magnetic unit cell form factor. The square of this number denoted by f, takes an exact value of 12.0 for the ferromagnetic phase. For the other phases, we find:

- $f \in [2.1 - 2.3]$ for the Kawamura Phase,
- $f \in [6 - 9]$ for the DT phase,

- $f \in [4.2 - 4.6]$ in the new $(qq0)$,
- $f \in [5.3 - 5.6]$ for the $(\frac{1}{2}\frac{1}{2}\frac{1}{2})$ phase.

This is not conclusive enough to claim that the unreported $(qq0)$ phase is distinct from the DT and Kawamura phase and has to be further investigated.

4.4.3 (hhh) degenerate state

In both PD_1 and PD_2 (Fig. 4.12 and Fig. 4.16), at the boundary of the $(\frac{1}{2}\frac{1}{2}\frac{1}{2})$ phase and the ferromagnetic phase, we find a state with accidental line degeneracies in the eigenspectrum along the $\langle 111 \rangle$ directions (in cubic coordinates) in the FBZ i.e. the line joining the $\mathbf{\Gamma}$ point to the $\mathbf{L}$ point in the FBZ (see Appendix A.2 and Fig. A.2). This state, shown as a blue dashed line in the phase diagrams (PD_1 and PD_2), exists only in the **third quadrant** of PD_1 but extends throughout the **second and fourth quadrants** of PD_2 (Fig. 4.16). The specifics of its existence near the origin has to be refined since the extent of the $(\frac{1}{2}\frac{1}{2}\frac{1}{2})$ phase gets thinner near the origin.

Plotting the minimum eigenvalues across the boundary shows a flat band at a higher energy than the ferromagnetic phase (see panels (a) and (b) of Fig. 4.18). Plotting the ordering wavevectors corresponding to the minimum eigenvalues at this boundary reveals a line degeneracy along (hhh) directions (see Fig. 4.18(d)). In Fig. 4.18(c), we plot all wavevectors corresponding to the minimum eigenvalue as well as eigenvalues close to the global minima. The wavevectors corresponding to eigenvalues close to the global minimum are the competing modes right above the MF transition temperature, T_c. Since this state

Location (by quadrant)	**Parametric equation**	**Extent of J_2**
PD_1 Fig. 4.12: III $J_a = +1$	$J_b = \frac{-4(J_2+3J_2^2)}{(1+4J_2)}$	$[-0.3^*, \frac{1}{2\sqrt{3}}]$
PD_2 Fig. 4.16: II and IV $J_a = -1$	$J_b = \frac{-4(-J_2+3J_2^2)}{-1+4J_2}$	$[-\frac{1}{2\sqrt{3}}, \frac{1}{6}]$

Table 4.2: Parametric equations of J_b and J_2 along which the (hhh) degenerate state may be found in the above mentioned phase diagrams.The star * denotes an estimation.

exists on just a line, it is interesting to study the competing modes from the ordered phases on either side of the boundary, above criticality. This is exposed by a tolerance parameter, Δ, given by:

$$\Delta = \frac{E_g - E}{E_g} \times 100. \tag{4.18}$$

Here E_g is the global minimum eigenvalue, E is the eigenvalue being considered. Specifying Δ, we can sort the ordering wavevectors with eigenvalues close to E_g. At $\Delta = 1\%$ this is effectively sampling over the competing modes above the transition temperature T_c in the cooperative-paramagnetic regime where these higher energy modes can be accessed. In Fig. 4.18(c) we find a sphere with cylindrical arms extending outwards along the $\langle 111 \rangle$ directions. The spherical structure near $\mathbf{q} = 0$ signifies proximity to the ferromagnetic regime and accessibility of these modes at $T > T_c$.

The question of how certain modes, from this degenerate line, will be selected either via thermal or by quantum fuctuations is an open question beyond the scope of this thesis. Material realization in this state is slim since this state can be found only along a line in

the phase diagram. However, if there is a material candidate near this line, ordering at T_c will seem a trivial FM $(0,0,0)$ phase. However, above T_c, the degenerate (hhh) modes, in close competition with the (000) modes, become accessible and may lead to interesting physics when $J_a > T > T_c$ (cooperative paramagnetic regime).

In the offchance one does find a candidate exactly on the line, one naively expects ferromagnet like scattering at high temperatures but possibly exotic physics at very low temperatures, such as novel order by disorder phenomena [81, 99, 100, 101, 102]. A tensor spin liquid was also recently proposed in Ref. [103] with singularities in the structure factors along $\langle 111 \rangle$ (which means the eigenvalues are minimum and degenerate along (hhh) as in our case), found in a related but different (and anisotropic) model for a specific point in the parameter space where three different ordered phases meet.

We have further computed the equation of the line along which this (hhh) degenerate state exists which was found by analytical inspection of eigenvalues. In particular, the dispersive eigenvalues are of the form, $E = X + Y(\mathbf{q}) \pm \sqrt{Z(\mathbf{q})}$. In this state, the eigenvalues accidentally become flat, so the $\mathbf{q}$-dependent part outside the square-root must negate exactly the $\mathbf{q}$-dependent part coming from within the square-root. Analyzing $Z(\mathbf{q})$, we parameterized the boundary which is summarized in Tab. 4.2. The spin structure factors for this state, showing crossed lines along (hhh), is displayed in Fig. 4.22.

4.4.4 Summary

We analyzed the phase diagrams J_b vs J_2, corresponding to constant AFM J_a (PD_1) and FM J_a (PD_2). For the sections of PD_1 and PD_2 studied in the literature, we find agreement of

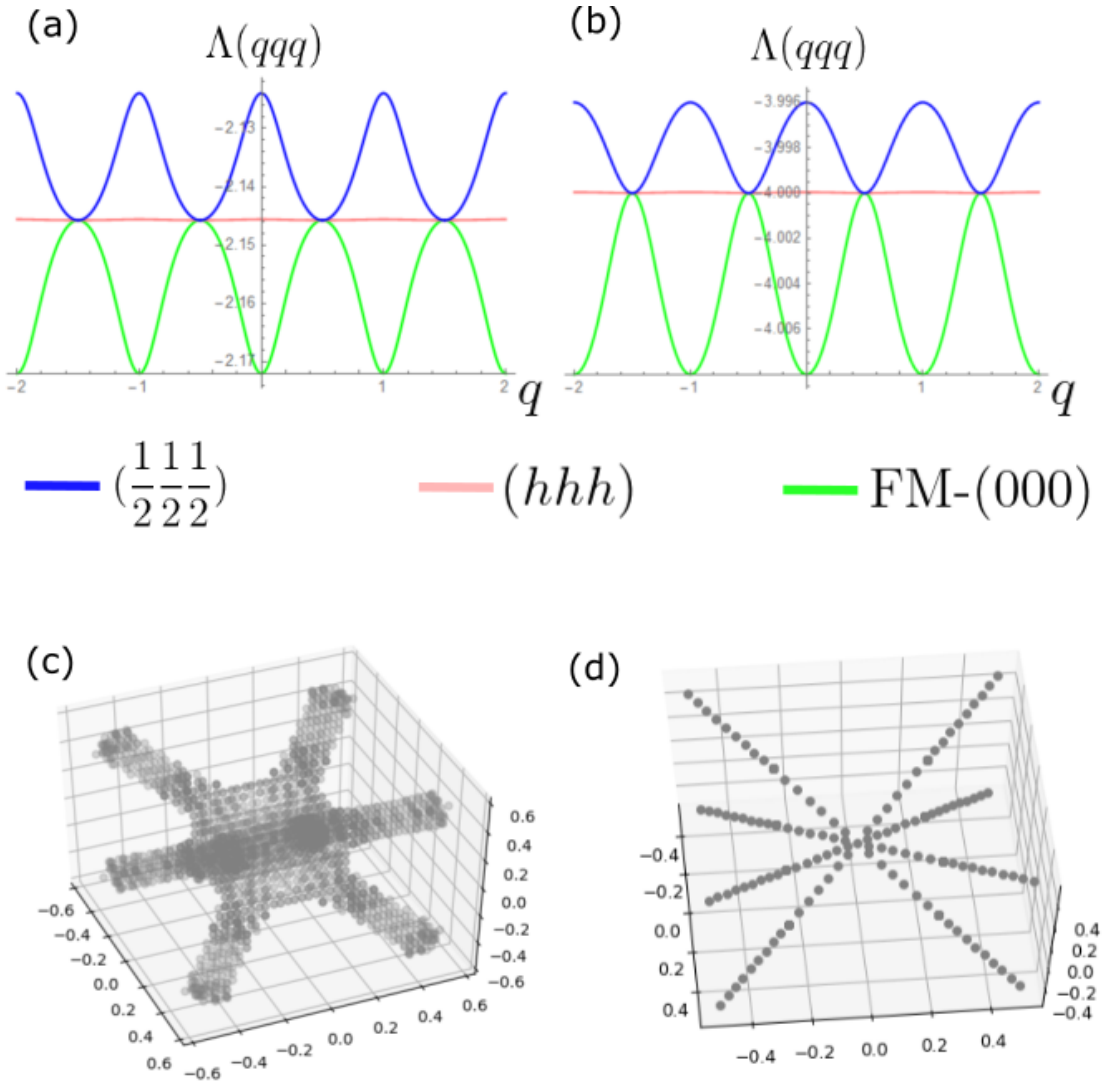

Figure 4.18: Phase boundaries of the $(\frac{1}{2}\frac{1}{2}\frac{1}{2})$ phase and the ferromagnetic phase host a peculiar state where the minimum eigenvalues $\Lambda(\mathbf{q})$ show an accidental degeneracy along the $\langle 111\rangle$ directions in the BZ. Panels (a) and (b) both show the minimum eigenvalue $\Lambda(\mathbf{q})$ along the (qqq) directions. The x-axes are wavevectors $\mathbf{q}$ in units of $\frac{2\pi}{a}$. The blue and the green are the aforementioned phase at the boundary of which one finds a flat band as J_2 is varied. (c) and (d) are three dimensional sections inside the FBZ of the FCC lattice plotting the wavevectors corresponding to energies including and above the global minima characterized by Δ (see Eq. (4.18)). The axes are in units of $\frac{2\pi}{a}$ and extend to half the FBZ in each direction. (c) $\Delta = 1\%$ and shows the modes which will be excited above the transition in the correlated-paramagnetic regime. (d) is close to criticality with $\Delta = 10^{-6}\%$ which show the soft $\mathbf{q}$-modes along the $[hhh]$ and symmetry related directions. Parameters provided in the form $[J_a,J_b,J_2]$: (a) In the first PD 3rd quadrant. Blue: [1,-0.5,-0.302] ; Green: [1,-0.5,-0.306]; Pink: [1,-0.5,-0.3038]. (b) In the second PD 4th quadrant. Blue: [-1,-1,0.167] ; Green: [-1,-1,0.166]; Pink: [-1,-1,0.16667]. (c),(d): any generic point on this boundary, uses parameters from (b).

the $\mathbf{q}_{\text{ord}}$ found in our work [79, 85, 86], except for the case of MMS where finer resolution of the $\mathbf{q}$-mesh (of the FBZ) reveals $\mathbf{q}_{\text{ord}} \equiv (ppq)$. For the hitherto unexplored regions (namely, J_a and J_b of opposite sign) we find (all phases summarized in Tab. 4.3):

- A $(\frac{1}{2}, \frac{1}{2}, \frac{1}{2})$ phase.
- An unreported $(qq0)$ phase.
- The effective AFM-FCC $(q10)$ phase with degenerate q.
- The planar spiral $(q00)$ phase.
- The Kawamura phase (only in PD_1).
- A state with line degeneracies along (hhh).
- A ferromagnetic phase

State	**Ordering Wavevectors in units of $\frac{2\pi}{a}$**	**Location (by quadrant)**
Coulomb Spin Liquid	All $\mathbf{q} \in BZ$	PD_1: I
Planar spiral	$(k00)$	PD_1: I and IV PD_2: IV
$\mathbf{k} = 0$	(200)	PD_1: I
Ferromagnet	(000)	PD_1: II and III PD_2 : II, III and IV
Cuboctahedral stack	$(\frac{1}{2}\frac{1}{2}\frac{1}{2})$	PD_1 : III PD_2: II and IV
Effective FCC-AFM	$(k10)$	PD_1 : III and IV PD_2: I, II and IV
Multiply modulated spiral	(ppq)	PD_2: IV
(kk0) type I "Kawamura"	$(kk0)$; $k^* \in [0.7, 0.74]$	PD_1: II and III
(kk0) type II "Double twist"	$(kk0)$; $k^* \in [0.7, 0.8]$	PD_2: IV
(kk0) type III	$(kk0)$; $k^* \in [0.8, 1]$	PD_1: III PD_2: II
Degenerate (hhh) line	(hhh)	PD_1: III PD_2: II and IV

Table 4.3: Summary of the phase diagrams and ordered phases obtained. The * represent the fact that these are incommensurate and are approximate since we have used a finite mesh and numerical schemes. The domains provided are also estimations and finer, more resolved searches especially near the phase boundaries might ammend these.

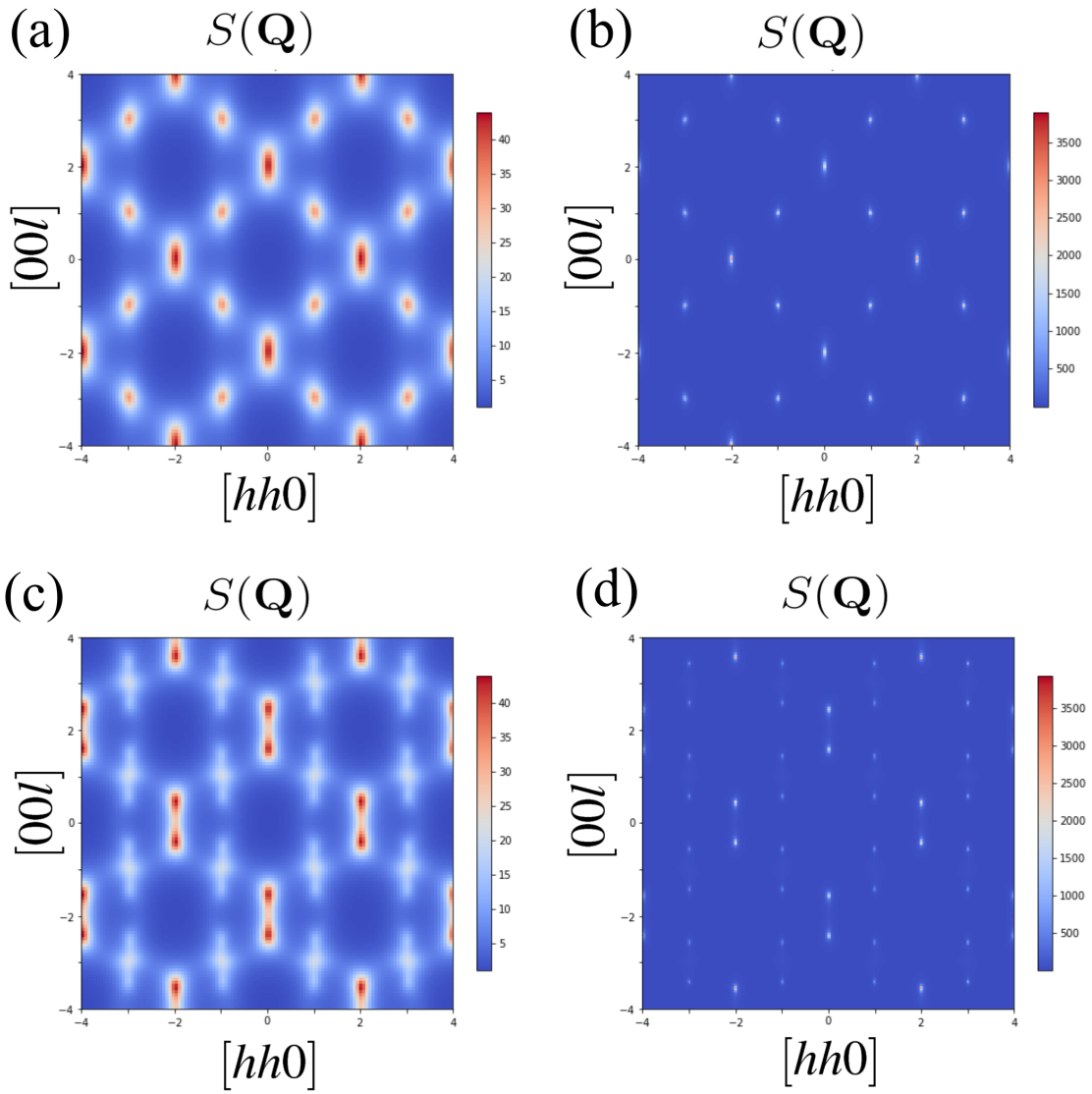

Figure 4.19: Figures show the spin structure factors $S(\mathbf{Q})$ (using MFT) for various parameter sets in the $[hhl]$ plane for high temperature ($\tau = 10^{-1}$ for (a) and (c)) and low temperature ($\tau = 10^{-3}$ for (b) and (d)). The x and y axes are in units of $\frac{2\pi}{a}$. (a) and (b) illustrate the $\mathbf{k} = 0$ state showing peaks at (200) with parameters: $J_a = 1$, $J_b = 0.7$, $J_2 = 0.3$. (c) and (d) show the planar spiral phase (PS) with peaks at $(q00)$. (c), (d) obtained using parameters: $J_a = 1$, $J_b = 0.8$, $J_2 = 0.8$

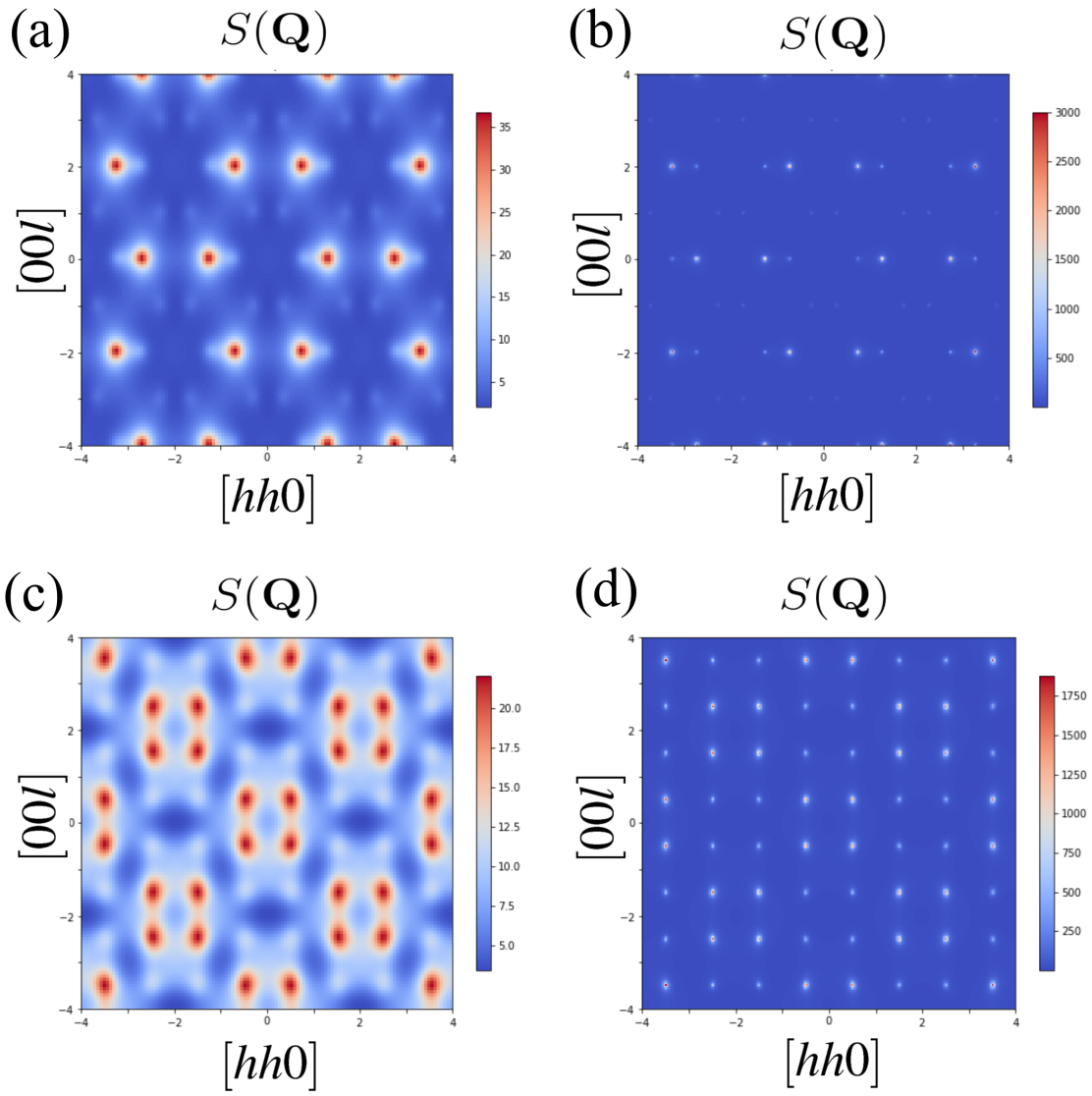

Figure 4.20: Figures show the spin structure factors $S(\mathbf{Q})$ (using MFT) for various parameter sets in the $[hhl]$ plane for high temperature ($\tau = 10^{-1}$ for (a) and (c)) and low temperature ($\tau = 10^{-3}$ for (b) and (d)). The x and y axes are in units of $\frac{2\pi}{a}$. (a) and (b) show the Kawamura phase with parameters $J_a = 1$, $J_b = 0.7$, $J_2 = -0.3$. (c) and (d) shows the $(\frac{1}{2}\frac{1}{2}\frac{1}{2})$ phase with parameters $J_a = 1$, $J_b = -0.7$, $J_2 = -0.2$.

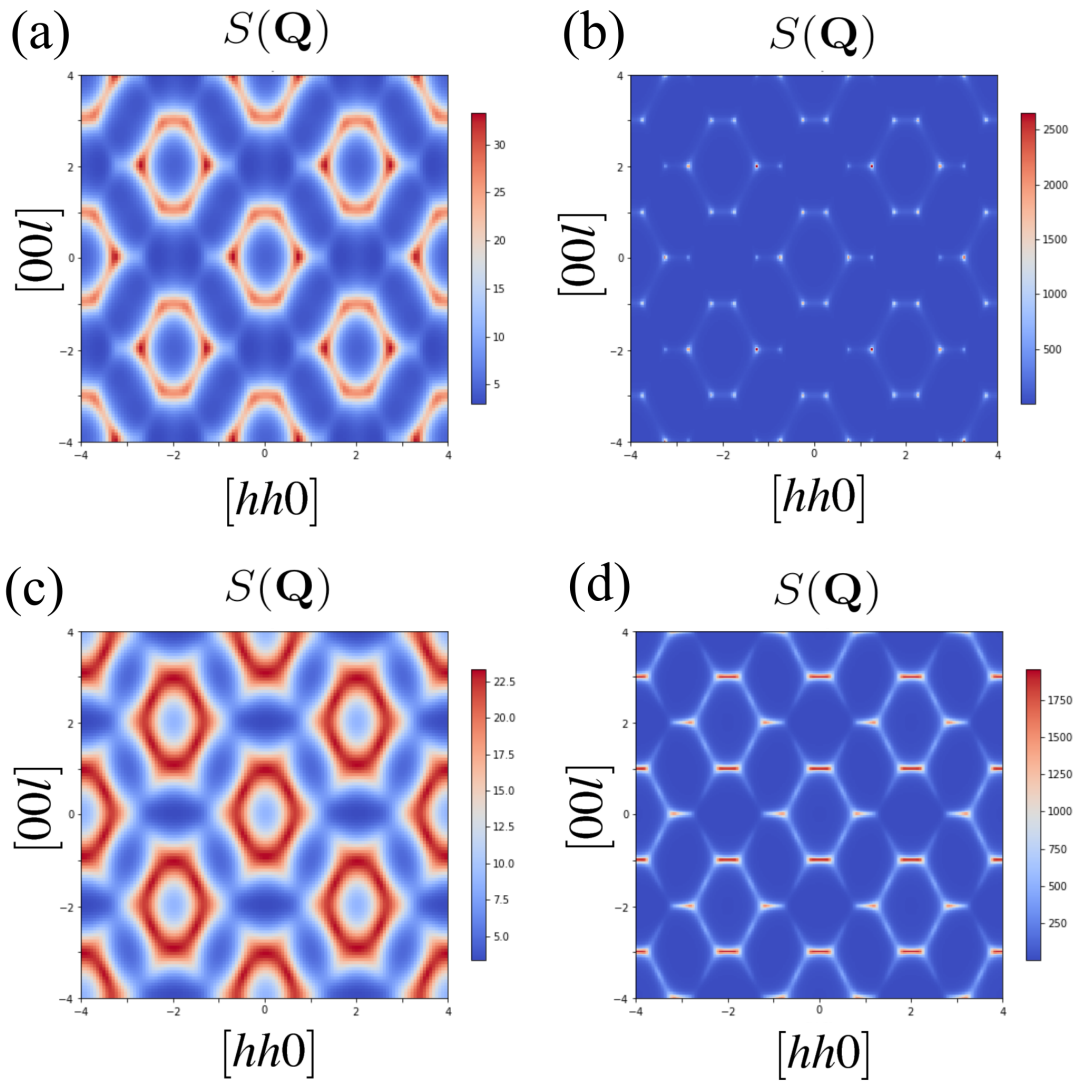

Figure 4.21: Figures show the spin structure factors $S(\mathbf{Q})$ (using MFT) for various parameter sets in the $[hhl]$ plane for high temperature ($\tau = 10^{-1}$ for (a) and (c)) and low temperature ($\tau = 10^{-3}$ for (b) and (d)). The x and y axes are in units of $\frac{2\pi}{a}$. (a) and (b) illustrates the double twist (DT) phase with parameters: $J_a = -1$, $J_b = -0.8$, $J_2 = 0.4$. (c) and (d) shows the heretofore unreported ($qq0$) phase with parameters: $J_a = -1$, $J_b = 0.8$, $J_2 = -0.116$.

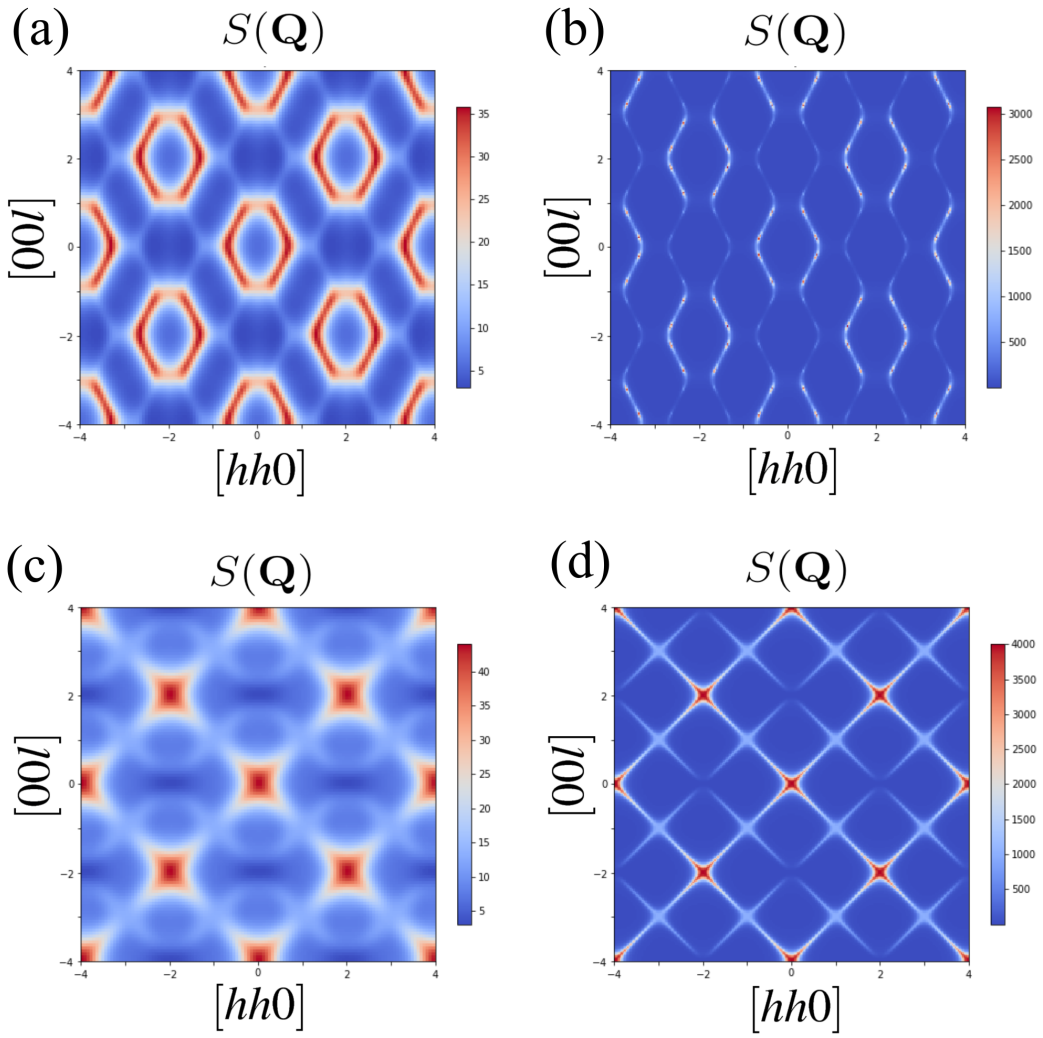

Figure 4.22: Figures show the spin structure factors $S(\mathbf{Q})$ (using MFT) for various parameter sets in the $[hhl]$ plane for high temperature ($\tau = 10^{-1}$ for (a) and (c)) and low temperature ($\tau = 10^{-3}$ for (b) and (d)). The x and y axes are in units of $\frac{2\pi}{a}$. (a) and (b) show the MMS phase with parameters $J_a = -1$, $J_b = -0.9$, $J_2 = 0.375$. (c) and (d) show the (hhh) degenerate state with parameters: $J_a = 1$, $J_b = -0.9425$, $J_2 = -0.29$.

Chapter 5

Discussions, Conclusions and Future Directions

In this thesis, we discussed spin models on a pyrochlore and breathing pyrochlore lattice (see Appendix A and Appendix A.3). We introduce key methods and formulae in Chap. 2 including the expressions for neutron scattering where the important quantity of interest is a spin-spin correlation function. We then obtained the expressions for the spin-spin correlation functions using mean-field theory and the large-N analysis. We discuss and summarize the next chapters below.

Chapter 3

In Chap. 3, we studied the case of Ising spins on a pyrochlore lattice where the spins are constrained to point along the local $\langle 111 \rangle$ directions. We found:

- **q**-independent flat bands of the Fourier transformed adjacency matrix (see Appendix A.4) corresponding to eigenvector $|P\rangle$ (Eq. (3.22)) in the $[hhl]$ plane.
- The neutron scattering probes only spins in an α-chain (see Fig. 3.5).
- The neutron scattering is written as $\langle P|\mathcal{M}^{-1}|P\rangle$ (see Eq. (3.48)). Here $|P\rangle$ is the neutron polarization projector (for non-spin flip scattering) proportional to the eigenvectors for the flat bands, in the $[hhl]$ plane. This yields Eq. (3.53), i.e. $\frac{d\sigma(\mathbf{Q})}{d\Omega}|_{\text{NSF}} = \frac{4}{3\lambda}$.
- The non-spin flip channel is also **q**-independent for extended spin ice[1] as well as Ising spins (constrained along $\langle 111\rangle$ directions) on a breathing pyrochlore lattice.
- The non-spin flip channel of polarized neutron scattering probes the stiffness of the emergent fields and neutron scattering probes the correlations between the emergent fluxes.
- One may obtain λ from the neutron scattering by using Eq. (3.70) and the identities provided in Eq. (3.69).

There are further unexplored and compelling avenues of research captured briefly through the follwoing questions:

- What are the geometrical reasons for the flat bands of the interaction matrix $J(\mathbf{q})$?
- Why is a constant shift (Eq. (3.17)) required to interpret λ as the flux stiffness? What happens when a different constant shift (such as the ground state energy as used in Ref. [21]) is utilized?

[1] See Ref. [63] for details on extended spin ice

- How can one reinterpret models with further-neighbour interactions into the flux/charge picture? Does it always make sense? What is the interpretation of λ in this case?
- Depending on the constant shift, why does λ either drop to 0 or diverge?
- What does it mean that the linecuts for the spin flip and non-spin flip channel (in spin ice and extended spin ice) are maximally correlated (has maximum and equal intensity) along the directions provided in Eq. (3.69)? Why are the intensities maximum and equal for both the spin flip and non-spin flip channels?
- Can actual highly calibrated neutron scattering experiments be done wherein one may obtain the stiffness of the emergent fields, λ?

Chapter 4

In Chap. 4, we studied Heisenberg spins on a breathing pyrochlore lattice in the abscence as well as the presence of further-neighbour interaction J_2. We characterized the phases by their ordering wavevectors $\mathbf{q}_{\text{ord}}$ at which the eigenvalues of the adjacency matrix is a global minimum in all the first Brillouin zone. We obtained two phase diagrams where nearest neighbour coupling J_a is either anti-ferromagnetic (PD_1) or ferromagnetic (PD_2). We found a variety of phases stabilized (shown in Fig. 4.12 and Fig. 4.16) which are summarized in Tab. 4.3.

In particular, we found that in the interface of two phases, namely the $(\frac{1}{2}\frac{1}{2}\frac{1}{2})$ and the ferromagnetic (000) phase, there exists a state with line degeneracies along the (hhh) directions (in the Fourier transformed eigenspectra, in the first Brillouin zone). We also

found a $(qq0)$ ordered phase sandwiched between the $(\frac{1}{2}\frac{1}{2}\frac{1}{2})$ and the effective AFM-FCC $(q10)$ phase. We believe this $(qq0)$ phase is unreported and may be distinct from the double twist and Kawamura phase with similar ordering wavevectors. Further analysis is required to confirm this. Future avenues of investigation and some interesting comments and questions regarding Heisenberg spins on breathing pyrochlores are briefed below:

- The effect of bond length ratios γ is outside the scope of this thesis and needs to be investigated to study the phase diagram for $\gamma \neq 1$.
- How do thermal and quantum fluctuations play out in the (hhh) degenerate state?
- Does the (hhh) degenerate line acquire a finite width when taking into account quantum mechanical effects? (For example the Coulomb spin liquid exists only on a line in the phase diagram. PFFRG analysis suggests that this line widens out for the quantum case and the Coulomb phase is stablized for small values of J_2. See Fig. 16 in Ref. [79])
- Does this (hhh) line and the new $(qq0)$ exist in the phase diagram with J_{3a} and J_{3b}?
- What is the difference between the new $(qq0)$, the Kawamura and the double twist phases? Why is there an approximate symmetry in PD_1 (Fig. 4.12) given by $J_a = +1$; $J_b < 0$; $J_2 \in [0, -0.2]$ and PD_2 (Fig. 4.16) parameterized by $J_a = -1$; $J_b > 0$; $J_2 \in [0, -0.2]$ in the second quadrant of PD_2?
- Does the partially ordered metastable phase described in Ref. [96] extend to Kawamura phase in the breathing regimes of PD_1 (see Fig. 4.12) ?

- What are the extents of the multiply modulated spiral, the double twist, the $(\frac{1}{2}\frac{1}{2}\frac{1}{2})$ and the new $(qq0)$ phase towards the origins of their respective phase diagrams? (see Fig. 4.12 and Fig. 4.16)

Conclusions

In this thesis, we saw how in the magnetic ground state, AFM Ising spins on a pyrochlore lattice, result in a Coulomb phase with emergent fluxes following a local divergence free constraint. We saw how polarized neutron scattering picks up a measure (specifically the stiffness) of this Coulomb phase. Next, we studied Heisenberg spins on a breathing pyrochlore lattice where further-neighbour interactions perturb the ground-state degeneracy and result in a plethora of ordered phases. We verified our findings with previous works and amended the ordering wavevectors for the multiply modulated spiral phase. One of the ordered phases consists of emergent clusters which interact with each other (the effective AFM-FCC phase) anti-ferromagnetically. We also found a previously unreported ordered phase and the (hhh) degenerate state where further studies (both theoretical and experimental) are required to answer the aforementioned questions.

References

[1] P. W. Anderson, "More is different," *Science*, vol. 177, pp. 393–396, Aug. 1972.

[2] A. P. Ramirez, "Strongly geometrically frustrated magnets," *Annual Review of Materials Science*, vol. 24, no. 1, pp. 453–480, 1994.

[3] J. T. Chalker, "Spin liquids and frustrated magnetism," pp. 123–164, Jan. 2017.

[4] L. Balents, "Spin liquids in frustrated magnets," *Nature*, vol. 464, pp. 199–208, Mar. 2010.

[5] J. Knolle and R. Moessner, "A field guide to spin liquids," *Annual Review of Condensed Matter Physics*, vol. 10, pp. 451–472, 2018.

[6] J. Villain, "Insulating spin glasses," *Zeitschrift für Physik B Condensed Matter and Quanta*, vol. 33, pp. 31–42, Mar. 1979.

[7] L. Savary and L. Balents, "Quantum spin liquids: a review," *Reports on Progress in Physics*, vol. 80, p. 016502, Nov. 2016.

[8] C. Broholm, R. J. Cava, S. A. Kivelson, D. G. Nocera, M. R. Norman, and T. Senthil, "Quantum spin liquids," *Science*, vol. 367, p. eaay0668, Jan. 2020.

[9] P. W. Anderson, "Ordering and antiferromagnetism in ferrites," *Phys. Rev.*, vol. 102, pp. 1008–1013, May 1956.

[10] J. S. Gardner, S. R. Dunsiger, B. D. Gaulin, M. J. P. Gingras, J. E. Greedan, R. F. Kiefl, M. D. Lumsden, W. A. MacFarlane, N. P. Raju, J. E. Sonier, I. Swainson, and Z. Tun, "Cooperative paramagnetism in the geometrically frustrated pyrochlore antiferromagnet $Tb_2Ti_2O_7$," *Phys. Rev. Lett.*, vol. 82, Feb 1999.

[11] P. H. Conlon, "Aspects of Frustrated Magnetism". PhD dissertation, Univ. Oxford, 2010.

[12] J. Jensen and A. R. Mackintosh, "Rare earth magnetism : structures and excitations," 1991.

[13] N. Niggemann, M. Hering, and J. Reuther, "Classical spiral spin liquids as a possible route to quantum spin liquids," *Journal of Physics: Condensed Matter*, vol. 32, p. 024001, Oct 2019.

[14] D. A. Garanin and B. Canals, "Classical spin liquid: Exact solution for the infinite-component antiferromagnetic model on the Kagomé lattice," *Phys. Rev. B*, vol. 59, pp. 443–456, Jan 1999.

[15] B. Canals and D. A. Garanin, "Spin-liquid phase in the pyrochlore anti-ferromagnet," *Canadian Journal of Physics*, vol. 79, pp. 1323–1331, Dec 2001.

[16] M. J. P. Gingras, B. C. den Hertog, M. Faucher, J. S. Gardner, S. R. Dunsiger, L. J. Chang, B. D. Gaulin, N. P. Raju, and J. Greedan, "Thermodynamic and single-ion properties of Tb^{3+} within the collective paramagnetic-spin liquid state of the frustrated pyrochlore antiferromagnet $Tb_2Ti_2O_7$," *Phys. Rev. B*, vol. 62, pp. 6496–6511, Sept. 2000.

[17] C. L. Henley, "The "Coulomb phase" in frustrated systems," *Annual Review of Condensed Matter Physics*, vol. 1, no. 1, pp. 179–210, 2010.

[18] C. L. Henley, "Power-law spin correlations in pyrochlore antiferromagnets," *Phys. Rev. B*, vol. 71, p. 014424, Jan 2005.

[19] T. Fennell, P. P. Deen, A. R. Wildes, K. Schmalzl, D. Prabhakaran, A. T. Boothroyd, R. J. Aldus, D. F. McMorrow, and S. T. Bramwell, "Magnetic Coulomb phase in the spin ice $Ho_2Ti_2O_7$," *Science*, vol. 326, pp. 415–417, Sep 2009.

[20] M. J. P. Gingras, "Spin ice," in *Introduction to Frustrated Magnetism*, pp. 293–329, Springer Berlin Heidelberg, Sept. 2010.

[21] O. Benton and N. Shannon, "Ground state selection and spin-liquid behaviour in the classical heisenberg model on the breathing pyrochlore lattice," *Journal of the Physical Society of Japan*, vol. 84, p. 12, June 2015.

[22] P. Ghosh, Y. Iqbal, T. Müller, R. T. Ponnaganti, R. Thomale, R. Narayanan, J. Reuther, M. J. P. Gingras, and H. O. Jeschke, "Breathing chromium spinels: a showcase for a variety of pyrochlore Heisenberg hamiltonians," *NPJ. Quantum Materials*, vol. 4, no. 1, p. 63, 2019.

[23] J. G. Rau, L. S. Wu, A. F. May, A. E. Taylor, I.-L. Liu, J. Higgins, N. P. Butch, K. A. Ross, H. S. Nair, M. D. Lumsden, M. J. P. Gingras, and A. D. Christianson, "Behavior of the breathing pyrochlore lattice $Ba_3Yb_2Zn_5O_{11}$ in applied magnetic field," *Journal of Physics: Condensed Matter*, vol. 30, p. 455801, Oct 2018.

[24] A. Furrer, J. Mesot, and T. Strässle, "Neutron scattering in condensed Matter physics". *World Scientific*, 2009.

[25] J. S. Nico and W. M. Snow, "Fundamental neutron physics," *Annual Review of Nuclear and Particle Science*, vol. 55, no. 1, pp. 27–69, 2005.

[26] S. Lovesey, "Thermal neutron scattering from condensed matter, vol. 2". *Oxford University Press*, 1984.

[27] Y. Izyumov and R. Ozerov, "Magnetic neutron diffraction". *New York*: *Plenum Press Press*, 1970.

[28] T. Chatterji, "*Chap. 1 - Magnetic Neutron Scattering*," in "Neutron Scattering from Magnetic Materials" (T. Chatterji, ed.), pp. 1 – 24, *Elsevier Science*, 2006.

[29] G. L. Squires, "Thermal neutron scattering". *Cambridge University Press*, 1978.

[30] W. Marshall and S. Lovesey, "Theory of Thermal Neutron Scattering". *Oxford University Press*, 1971.

[31] I. Obodovskiy, "Neutron sources," in *Radiation*, pp. 289–292, Elsevier, 2019.

[32] J. Greensite, "Scattering theory," in *An Introduction to Quantum Theory*, 2053-2563, pp. 22–1 to 22–32, IOP Publishing, 2017.

[33] P. Debye, "Interferenz von röntgenstrahlen und wärmebewegung," *Annalen der Physik*, vol. 348, no. 1, pp. 49–92, 1913.

[34] I. Waller, "Zür frage der einwirkung der warmebewegung auf die interferenz von rontgenstrahlen," *Zeitschrift für Physik*, vol. 17, pp. 398–408, Dec 1923.

[35] J. N. Reimers, A. J. Berlinsky, and A.-C. Shi, "Mean-field approach to magnetic ordering in highly frustrated pyrochlores," *Phys. Rev. B*, vol. 43, pp. 865–878, Jan. 1991.

[36] M. Enjalran and M. J. P. Gingras, "Theory of paramagnetic scattering in highly frustrated magnets with long-range dipole-dipole interactions: The case of the $Tb_2Ti_2O_7$ pyrochlore antiferromagnet," *Phys. Rev. B*, vol. 70, p. 174426, Nov 2004.

[37] R. Brout and H. Thomas, "Molecular field theory, the Onsager reaction field and the spherical model," *Physics Physique Fizika*, vol. 3, pp. 317–329, Dec 1967.

[38] T. H. Berlin and M. Kac, "The spherical model of a ferromagnet," *Phys. Rev.*, vol. 86, pp. 821–835, Jun 1952.

[39] H. E. Stanley, "Spherical model as the limit of infinite spin dimensionality," *Phys. Rev.*, vol. 176, pp. 718–722, Dec 1968.

[40] L. Onsager, "Electric moments of molecules in liquids," *Journal of the American Chemical Society*, vol. 58, pp. 1486–1493, Aug 1936.

[41] V. H. Santos and C. Scherer, "A new approximation for the dynamics of the transverse Ising model," *Zeitschrift für Physik B Condensed Matter*, vol. 40, pp. 95–97, Mar 1980.

[42] P. H. Conlon and J. T. Chalker, "Absent pinch points and emergent clusters: Further neighbor interactions in the pyrochlore Heisenberg antiferromagnet," *Phys. Rev. B*, vol. 81, p. 224413, Jun 2010.

[43] S. V. Isakov, "Correlations in frustrated magnets : classical and quantum aspects". PhD dissertation, *Stockholm University*, 2004.

[44] M. Moshe and J. Zinn-Justin, "Quantum field theory in the large N limit: a review," *Physics Reports*, vol. 385, pp. 69–228, Oct 2003.

[45] S. V. Isakov, K. Gregor, R. Moessner, and S. L. Sondhi, "Dipolar spin correlations in classical pyrochlore magnets," *Phys. Rev. Lett.*, vol. 93, Oct 2004.

[46] T. Mizoguchi, L. D. C. Jaubert, R. Moessner, and M. Udagawa, "Magnetic clustering, half-moons, and shadow pinch points as signals of a proximate Coulomb phase in frustrated Heisenberg magnets," *Phys. Rev. B*, vol. 98, p. 144446, Oct 2018.

[47] E. Lantagne-Hurtubise, J. G. Rau, and M. J. P. Gingras, "Spin-ice thin films: Large-N theory and Monte Carlo simulations," *Phys. Rev. X*, vol. 8, p. 021053, May 2018.

[48] Z. Dun, X. Bai, J. A. M. Paddison, N. P. Butch, C. R. D. Cruz, M. B. Stone, T. Hong, M. Mourigal, and H. Zhou, "Quantum spin fragmentation in Kagomé ice $Ho_3Mg_2Sb_3O_{14}$," *arXiv: Strongly Correlated Electrons*, 2018.

[49] C. Kittel, *Introduction to Solid State Physics*. Wiley, 8 ed., 2004.

[50] "Python numpy documentation." https://numpy.org/doc/.

[51] S. T. Bramwell and M. J. P. Gingras, "Spin ice state in frustrated magnetic pyrochlore materials," *Science*, vol. 294, pp. 1495–1501, Nov. 2001.

[52] S. T. Bramwell, M. J. Harris, B. C. den Hertog, M. J. P. Gingras, J. S. Gardner, D. F. McMorrow, A. R. Wildes, A. L. Cornelius, J. D. M. Champion, R. G. Melko, and T. Fennell, "Spin correlations in $Ho_2Ti_2O_7$: A dipolar spin ice system," *Phys. Rev. Lett*, vol. 87, p. 047205, Jul 2001.

[53] M. J. Harris, S. T. Bramwell, D. F. McMorrow, T. Zeiske, and K. W. Godfrey, "Geometrical frustration in the ferromagnetic pyrochlore $Ho_2Ti_2O_7$," *Phys. Rev. Lett*, vol. 79, pp. 2554–2557, Sep 1997.

[54] A. P. Ramirez, A. Hayashi, R. J. Cava, R. Siddharthan, and B. S. Shastry, "Zero-point entropy in 'spin ice'," *Nature*, vol. 399, pp. 333–335, May 1999.

[55] J. G. Rau and M. J. P. Gingras, "Magnitude of quantum effects in classical spin ices," *Phys. Rev. B*, vol. 92, p. 144417, Oct 2015.

[56] R. Moessner, "Relief and generation of frustration in pyrochlore magnets by single-ion anisotropy," *Phys. Rev. B*, vol. 57, pp. R5587–R5589, Mar. 1998.

[57] J. D. Bernal and R. H. Fowler, "A theory of water and ionic solution, with particular reference to hydrogen and hydroxyl ions," *The Journal of Chemical Physics*, vol. 1, pp. 515–548, Aug. 1933.

[58] S. V. Isakov, R. Moessner, and S. L. Sondhi, "Why spin ice obeys the ice rules," *Phys. Rev. Lett*, vol. 95, p. 217201, Nov 2005.

[59] T. Fennell, O. A. Petrenko, B. Fåk, J. S. Gardner, S. T. Bramwell, and B. Ouladdiaf, "Neutron scattering studies of the spin ices $Ho_2Ti_2O_7$ and $Dy_2Ti_2O_7$ in applied magnetic field," *Phys. Rev. B*, vol. 72, p. 224411, Dec 2005.

[60] O. Benton, L. D. C. Jaubert, H. Yan, and N. Shannon, "A spin-liquid with pinch-line singularities on the pyrochlore lattice," *Nature Communications*, vol. 7, May 2016.

[61] M. Taillefumier, O. Benton, H. Yan, L. D. C. Jaubert, and N. Shannon, "Competing spin liquids and hidden spin-nematic order in spin ice with frustrated transverse exchange," *Phys. Rev. X*, vol. 7, p. 041057, Dec 2017.

[62] Y. Kato and S. Onoda, "Numerical evidence of quantum melting of spin ice: quantum-to-classical crossover," *Phys. Rev. Lett*, vol. 115, p. 077202, Aug 2015.

[63] J. G. Rau and M. J. P. Gingras, "Spin slush in an extended spin ice model," *Nature Communications*, vol. 7, Jul 2016.

[64] C. Castelnovo, R. Moessner, and S. L. Sondhi, "Magnetic monopoles in spin ice," *Nature*, vol. 451, pp. 42–45, Jan 2008.

[65] R. W. Youngblood and J. D. Axe, "Polarization fluctuations in ferroelectric models," *Phys. Rev. B*, vol. 23, pp. 232–238, Jan 1981.

[66] M. Udagawa, L. D. C. Jaubert, C. Castelnovo, and R. Moessner, "Out-of-equilibrium dynamics and extended textures of topological defects in spin ice," *Phys. Rev. B*, vol. 94, p. 104416, Sep 2016.

[67] J. G. Rau, L. S. Wu, A. F. May, L. Poudel, B. Winn, V. O. Garlea, A. Huq, P. Whitfield, A. E. Taylor, M. D. Lumsden, M. J. P. Gingras, and A. D. Christianson, "Anisotropic exchange within decoupled tetrahedra in the quantum breathing pyrochlore $Ba_3Yb_2Zn_5O_{11}$," *Phys. Rev. Lett*, vol. 116, p. 257204, Jun 2016.

[68] S.-Y. Park, S.-H. Do, K.-Y. Choi, J.-H. Kang, D. Jang, B. Schmidt, M. Brando, B.-H. Kim, D.-H. Kim, N. P. Butch, S. Lee, J.-H. Park, and S. Ji, "Spin–orbit coupled molecular quantum magnetism realized in inorganic solid," *Nature Communications*, vol. 7, Sep 2016.

[69] T. Haku, K. Kimura, Y. Matsumoto, M. Soda, M. Sera, D. Yu, R. A. Mole, T. Takeuchi, S. Nakatsuji, Y. Kono, T. Sakakibara, L.-J. Chang, and T. Masuda, "Low-energy excitations and ground-state selection in the quantum breathing pyrochlore antiferromagnet $Ba_3Yb_2Zn_5O_{11}$," *Phys. Rev. B*, vol. 93, p. 220407, Jun 2016.

[70] H. Pinch, M. Woods, and E. Lopatin, "Some new mixed a-site chromium chalcogenide spinels," *Materials Research Bulletin*, vol. 5, no. 6, pp. 425 – 429, 1970.

[71] H. Haeuseler and H. Lutz, "Gitterschwingungsspektren XVIII. mitteilung: Chromthio- und chromselenospinelle mit 1:1-ordnung auf den tetraederplätzen," *Journal of Solid State Chemistry*, vol. 22, no. 2, pp. 201 – 204, 1977.

[72] S. Lee, S.-H. Do, W. Lee, Y. Choi, M. Lee, E. Choi, A. Reyes, P. Kuhns, A. Ozarowski, and K. Choi, "Multistage symmetry breaking in the breathing pyrochlore lattice Li(Ga,In)Cr_4O_8," *Phys. Rev. B*, vol. 93, May 2016.

[73] S. A. Tolba, K. M. Gameel, B. A. Ali, H. A. Almossalami, and N. K. Allam, "The DFT+U: Approaches, accuracy, and applications," in *Density Functional Calculations - Recent Progresses of Theory and Application*, InTech, May 2018.

[74] Y. Iqbal, R. Thomale, F. Parisen Toldin, S. Rachel, and J. Reuther, "Functional renormalization group for three-dimensional quantum magnetism," *Phys. Rev. B*, vol. 94, p. 140408, Oct 2016.

[75] P. Ghosh, T. Müller, F. P. Toldin, J. Richter, R. Narayanan, R. Thomale, J. Reuther, and Y. Iqbal, "Quantum paramagnetism and helimagnetic orders in the Heisenberg model on the body centered cubic lattice," *Phys. Rev. B*, vol. 100, p. 014420, Jul 2019.

[76] M. L. Baez and J. Reuther, "Numerical treatment of spin systems with unrestricted spin length S: A functional renormalization group study," *Phys. Rev. B*, vol. 96, p. 045144, Jul 2017.

[77] A. Durif-Varambon and J.-C. Joubert, "Étude de quelques composés spinelles nouveaux possédant un ordre des cations du type 1/1 sur les sites tétraédriques," *Bulletin de la Société française de Minéralogie et de Cristallographie, volume 89, 1*, 1966.

[78] Y. Okamoto, G. J. Nilsen, J. P. Attfield, and Z. Hiroi, "Breathing pyrochlore lattice realized in *A*-site ordered spinel oxides $LiGaCr_4O_8$ and $LiInCr_4O_8$," *Phys. Rev. Lett*, vol. 110, p. 097203, Feb 2013.

[79] Y. Iqbal, T. Müller, P. Ghosh, M. J. P. Gingras, H. O. Jeschke, S. Rachel, J. Reuther, and R. Thomale, "Quantum and classical phases of the pyrochlore Heisenberg model with competing interactions," *Phys. Rev. X*, vol. 9, p. 011005, Jan 2019.

[80] N. N. Sun and H.-Y. Wang, "The $J_1 - J_2$ model on the face-centered-cubic lattices," *Journal of Magnetism and Magnetic Materials*, vol. 454, pp. 176–184, May 2018.

[81] C. L. Henley, "Ordering by disorder: ground-state selection in FCC vector antiferromagnets," *Journal of Applied Physics*, vol. 61, no. 8, pp. 3962–3964, 1987.

[82] M. V. Gvozdikova and M. E. Zhitomirsky, "A Monte Carlo study of the first-order transition in a Heisenberg FCC antiferromagnet," *Journal of Experimental and Theoretical Physics Letters*, vol. 81, no. 5, pp. 236–240, 2005.

[83] G. Pokharel, H. S. Arachchige, T. J. Williams, A. F. May, R. S. Fishman, G. Sala, S. Calder, G. Ehlers, D. S. Parker, T. Hong, A. Wildes, D. Mandrus, J. A. M. Paddison, and A. D. Christianson, "Cluster frustration in the breathing pyrochlore magnet $LiGaCr_4S_8$," *ArXiv eprint 2002.09749*, 2020.

[84] H. E. Viertiö and A. S. Oja, "Interplay of three antiferromagnetic modulations in the nuclear-spin system of copper," *Phys. Rev. B*, vol. 48, pp. 1062–1076, Jul 1993.

[85] M. F. Lapa and C. L. Henley, "Ground states of the classical antiferromagnet on the pyrochlore lattice," *arXiv e-prints*, p. arXiv:1210.6810, Oct. 2012.

[86] M. F. Lapa, "BSc thesis on ground states of the classical antiferromagnet on the pyrochlore lattice," *Cornell Thesis archives*, 2012.

[87] "Scipy documentation." https://docs.scipy.org/doc/scipy/reference/tutorial/optimize.html.

[88] J. A. Nelder and R. Mead, "A simplex method for function minimization," *Comput. J.*, vol. 7, pp. 308–313, 1965.

[89] M. Wright, *Direct search methods: Once scorned, now respectable*, pp. 191–208. Addison-Wesley, 1996.

[90] F. Gao and L. Han, "Implementing the Nelder-Mead simplex algorithm with adaptive parameters," *Computational Optimization and Applications*, vol. 51, pp. 259–277, May 2010.

[91] M. J. D. Powell, "An efficient method for finding the minimum of a function of several variables without calculating derivatives," *The Computer Journal*, vol. 7, no. 2, p. 155, 1964.

[92] *Numerical Optimization*. Springer New York, 2006.

[93] R. Byrd, P. Lu, J. Nocedal, and C. Zhu, "A limited memory algorithm for bound constrained optimization," *SIAM Journal on Scientific Computing*, vol. 16, Feb. 2003.

[94] J. Larson, M. Menickelly, and S. M. Wild, "Derivative-free optimization methods," *Acta Numerica*, vol. 28, p. 287–404, 2019.

[95] D. Tsuneishi, M. Ioki, and H. Kawamura, "Novel ordering of the pyrochlore heisenberg antiferromagnet with the ferromagnetic next-nearest-neighbour interaction," *Journal of Physics: Condensed Matter*, vol. 19, p. 145273, Mar 2007.

[96] G.-W. Chern, R. Moessner, and O. Tchernyshyov, "Partial order from disorder in a classical pyrochlore antiferromagnet," *Phys. Rev. B*, vol. 78, p. 144418, Oct 2008.

[97] T. Okubo, T. H. Nguyen, and H. Kawamura, "Cubic and noncubic multiple-q states in the Heisenberg antiferromagnet on the pyrochlore lattice," *Phys. Rev. B*, vol. 84, p. 144432, Oct 2011.

[98] K. Fritsch, K. A. Ross, Y. Qiu, J. R. D. Copley, T. Guidi, R. I. Bewley, H. A. Dabkowska, and B. D. Gaulin, "Antiferromagnetic spin ice correlations at $(\frac{1}{2},\frac{1}{2},\frac{1}{2})$ in the ground state of the pyrochlore magnet $Tb_2Ti_2O_7$," *Phys. Rev. B*, vol. 87, p. 094410, Mar. 2013.

[99] J. Villain, R. Bidaux, J. P. Carton, and R. M. Conte, "Order as an effect of disorder," *Journal de Physique*, vol. 41, pp. 1263–1272, 1980.

[100] M. Millonas, ed., *Fluctuations and Order*. Springer US, 1996.

[101] D. Bergman, J. Alicea, E. Gull, S. Trebst, and L. Balents, "Order-by-disorder and spiral spin-liquid in frustrated diamond-lattice antiferromagnets," *Nature Physics*, vol. 3, pp. 487–491, May 2007.

[102] C. L. Henley, "Ordering due to disorder in a frustrated vector antiferromagnet.," *Phys. Rev. Lett.*, vol. 62 17, pp. 2056–2059, 1989.

[103] O. Benton, L. Jaubert, H. Yan, and N. Shannon, "A spin-liquid with pinch-line singularities on the pyrochlore lattice," *Nature Communications*, vol. 7, May 2016.

[104] J. G. Rau and M. J. Gingras, "Frustrated quantum rare-earth pyrochlores," *Annual Review of Condensed Matter Physics*, vol. 10, no. 1, pp. 357–386, 2019.

[105] P. A. M. Dirac, "Quantised singularities in the electromagnetic field," *Proceedings of the Royal Society of London. Series A, Containing Papers of a Mathematical and Physical Character*, vol. 133, pp. 60–72, Sep 1931.

[106] M. J. P. Gingras and B. C. Den Hertog, "Origin of spin ice behavior in Ising pyrochlore magnets with long range dipole interactions: an insight from mean-field theory," *Can. J. Phys.*, vol. 79, no. cond-mat/0012275, p. 1339, 2001.

[107] B. Javanparast, Z. Hao, M. Enjalran, and M. J. P. Gingras, "Fluctuation-driven selection at criticality in a frustrated magnetic system: The case of multiple-**k** partial order on the pyrochlore lattice," *Phys. Rev. Lett*, vol. 114, p. 130601, Apr 2015.

[108] J. N. Reimers, "Diffuse-magnetic-scattering calculations for frustrated antiferromagnets," *Phys. Rev. B*, vol. 46, pp. 193–202, July 1992.

[109] B. Wilts, K. Michielsen, H. Raedt, and D. Stavenga, "Hemispherical brillouin zone imaging of a diamond-type biological photonic crystal," *Journal of the Royal Society, Interface / the Royal Society*, vol. 9, pp. 1609–14, Dec. 2011.

APPENDICES

Appendix A

Lattices and Conventions

A.1 Pyrochlore lattice

We have used global Cartesian (cubic) axes in this thesis. The pyrochlore lattice is a lattice of corner sharing tetrahedra where each tetrahedron of one type (up or down) reside on a Face Centred Cubic (FCC) lattice (see Fig. A.1). The FCC lattice and reciprocal lattice vectors are given below in Tab. A.1. Further information may be obtained from Ref. [49]. This choice of unit cell contains four tetrahedra and sixteen spins. If one sublattice of the terahedron is at the origin, the other sublattices reside at half the distance of the FCC basis vectors (denoted by $\mathbf{R}$ here). The sublattice positions are denoted by $\mathbf{r}$ here and the FCC reciprocal lattice vectors are given by $\mathbf{G}$. We have also provided the directions of the easy axis for spins constrained to lie along the local $\langle 111 \rangle$ axes in the pyrochlore lattice. Real space quantities have units of conventional unit cell length a. Reciprocal space quantities

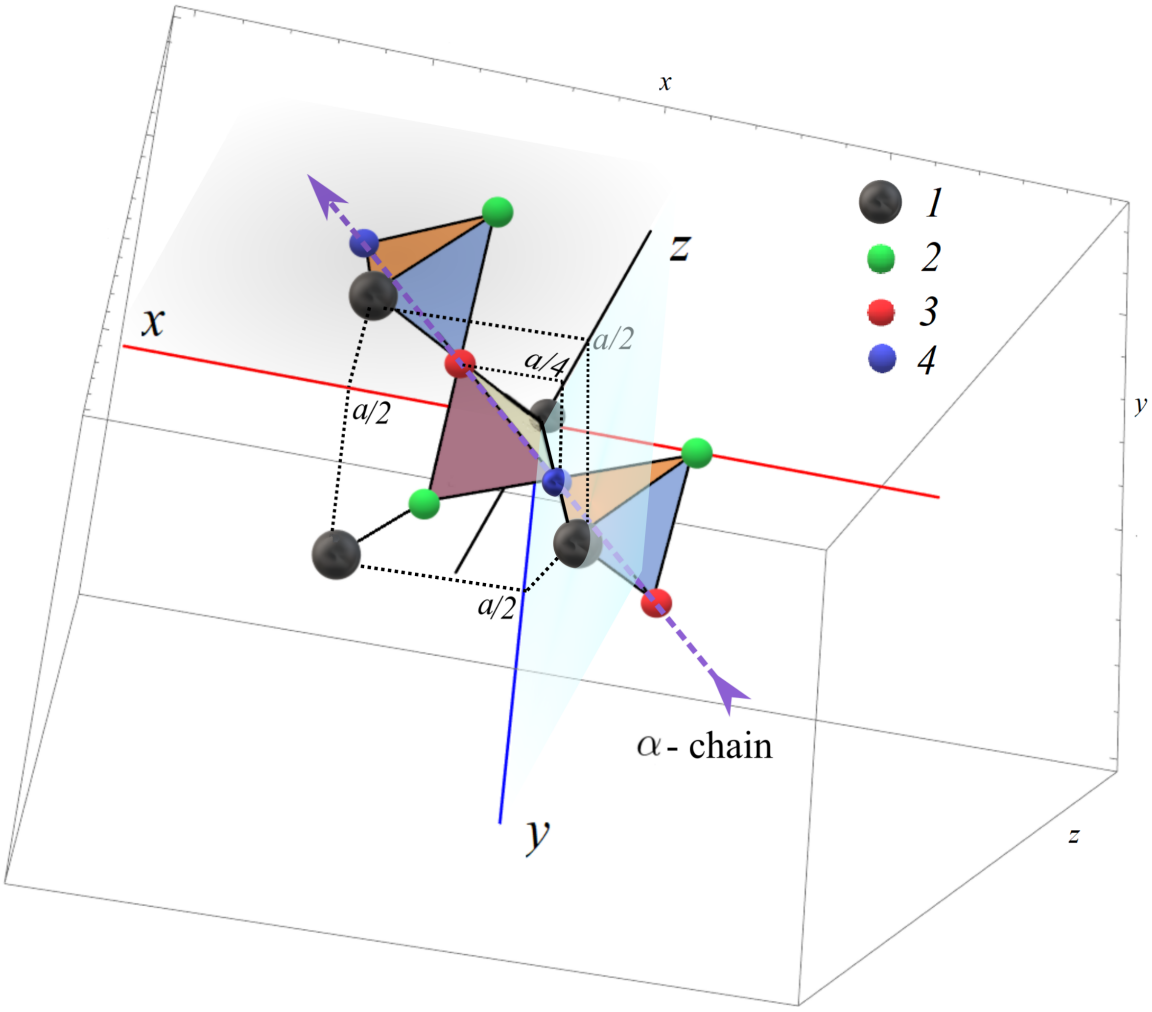

Figure A.1: Figure shows three tetrahedra in the pyrochlore lattice. The sublattice conventions used in this thesis are given in the legend above with the dark grey spheres showing sublattice 1. Sublattice 1 of each tetrahedron are the FCC centres (shown here of greater radius) at $(\frac{a}{2},\frac{a}{2},0)$ and symmetry related points (see Tab. A.1). The red and blue spheres are sublattices 3 and 4 composing the α-chain (see Fig. 3.5 and Chap. 3) which is denoted by a purple arrow. a is the conventional unit cell length.

Index	FCC basis vectors $\mathbf{R}$	Sublattice positions $\mathbf{r}$	Reciprocal lattice vectors $\mathbf{G}$	Local $\hat{\mathbf{z}}$
1	$[000]$	$[000]$	$[000]$	$\frac{1}{\sqrt{3}}[111]$
2	$\frac{1}{2}[110]$	$\frac{1}{4}[110]$	$[11\bar{1}]$	$\frac{1}{\sqrt{3}}[\bar{1}\bar{1}1]$
3	$\frac{1}{2}[101]$	$\frac{1}{4}[101]$	$[1\bar{1}1]$	$\frac{1}{\sqrt{3}}[\bar{1}1\bar{1}]$
4	$\frac{1}{2}[011]$	$\frac{1}{4}[011]$	$[\bar{1}11]$	$\frac{1}{\sqrt{3}}[1\bar{1}\bar{1}]$

Table A.1: Lattice conventions for the pyrochlore used in this report

are in units of $\frac{2\pi}{a}$. We summarize the conventions utilized in this thesis in Tab. A.1.

A.2 First Brillouin zone of the FCC lattice

The First Brillouin Zone (FBZ) of the FCC lattice is the Wigner Seitz cell of the Body Centred Cubic (BCC) lattice [49]. The conditions are:

$$0 \leq |q_x| + |q_y| + |q_z| \leq \frac{3\pi}{a}, \tag{A.1}$$

$$0 \leq |q_x| \leq \frac{2\pi}{a}, \tag{A.2}$$

$$0 \leq |q_y| \leq \frac{2\pi}{a}, \tag{A.3}$$

$$0 \leq |q_z| \leq \frac{2\pi}{a}. \tag{A.4}$$

$$\tag{A.5}$$

Here, the individual components of $\mathbf{q}$-space vectors are denoted by $q_x/q_y/q_z$ and using these formulae, one can efficiently sample over the FBZ. The extended Brillouin zone is sometimes referred to in the literature, which is obtained by doubling the right hand side

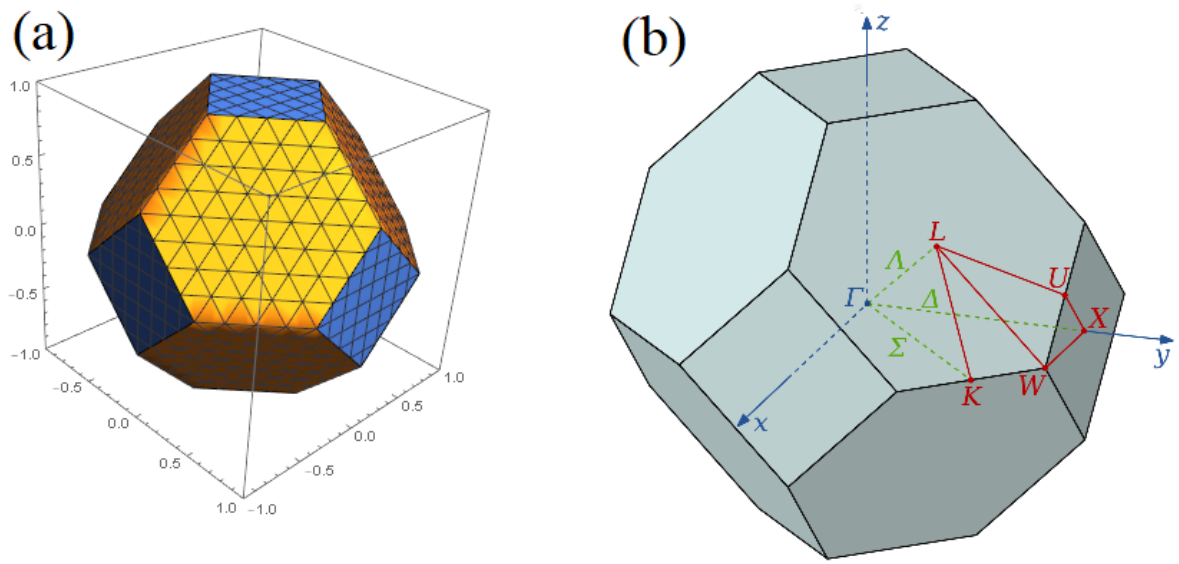

Figure A.2: Panels (a) and (b) showing the First Brillouin Zone (FBZ) of FCC Lattice. Figure (a) is made using Wolfram Mathematica. Figure (b) is sourced from Wikipedia and is a Google stock image.

of the above equations (2π to 4π, 3π to 6π).

A.3 Breathing Pyrochlore lattice

The breathing pyrochlore is similar to the pyrochlore in that it is constructed with corner sharing tetrahedra of different sizes (see Fig. 4.1, Fig. A.3, Fig. 4.11, Fig. A.4). We consider the up/bigger tetrahedra to be on the positive side of the origin. If the bond distance of the smaller tetrahedra is d, let the bond lengths of the larger tetrahedra be γd. This yields a relationship between the conventional unit cell length a to d given by:

$$a = \sqrt{2}d(\gamma + 1). \tag{A.6}$$

Index	FCC basis vectors $\mathbf{R}$	Sublattice positions $\mathbf{r}$	Recip. lattice vectors $\mathbf{G}$
1	$[000]$	$[000]$	$[000]$
2	$\frac{a}{2}[110]$	$\frac{\gamma d}{\sqrt{2}}[110]$	$\frac{2\pi}{a}[11\bar{1}]$
3	$\frac{a}{2}[101]$	$\frac{\gamma d}{\sqrt{2}}[101]$	$\frac{2\pi}{a}[1\bar{1}1]$
4	$\frac{a}{2}[011]$	$\frac{\gamma d}{\sqrt{2}}[011]$	$\frac{2\pi}{a}[\bar{1}11]$

Table A.2: Lattice conventions for the breathing pyrochlore. If $\gamma = 1$ (non breathing) and $d = 1/\sqrt{8}$ we get back $a = 1$ and the same sublattice positions as the (non-breathing) pyrochlore lattice. Otherwise, Eq. (A.6) may be used to keep a at unity.

Using this formula one may vary the bond length ratios γ and smaller bond distance d to keep a at unity. Otherwise, using a non-unity magnitude a, one may construct the FBZ using the above provided formulae in Eq. (A.1-A.5). The conventions are summarized in Tab. A.2. The breathing lattice is shown in Fig. A.3, Fig. A.4 and Fig. 4.1.

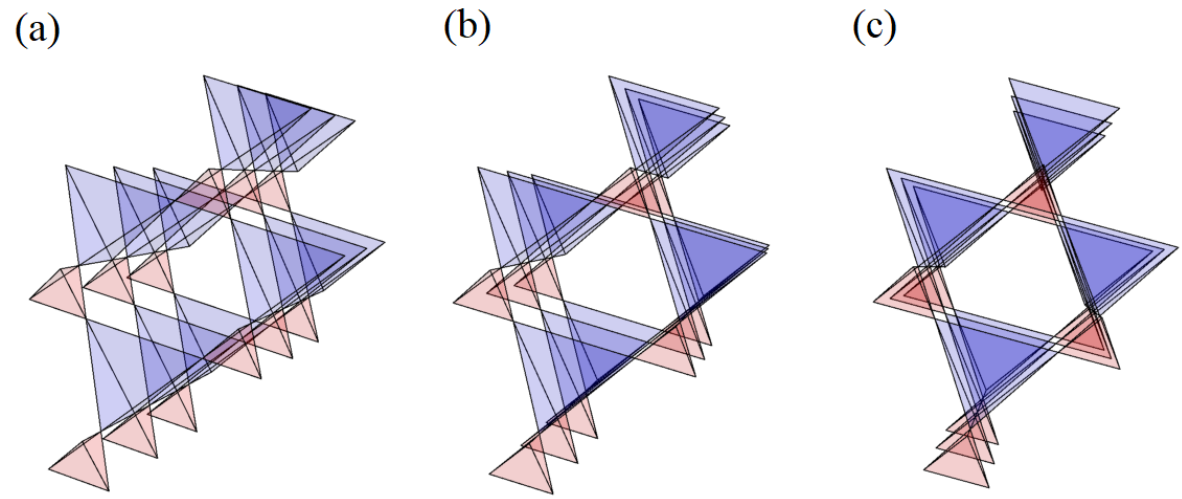

Figure A.3: Figure showing the rotation of the breathing pyrochlore lattice. Panel (c) shows the lattice when the ⟨111⟩ directions are perpendicular to the page, wherein the kagomé layer is seen in perspective.

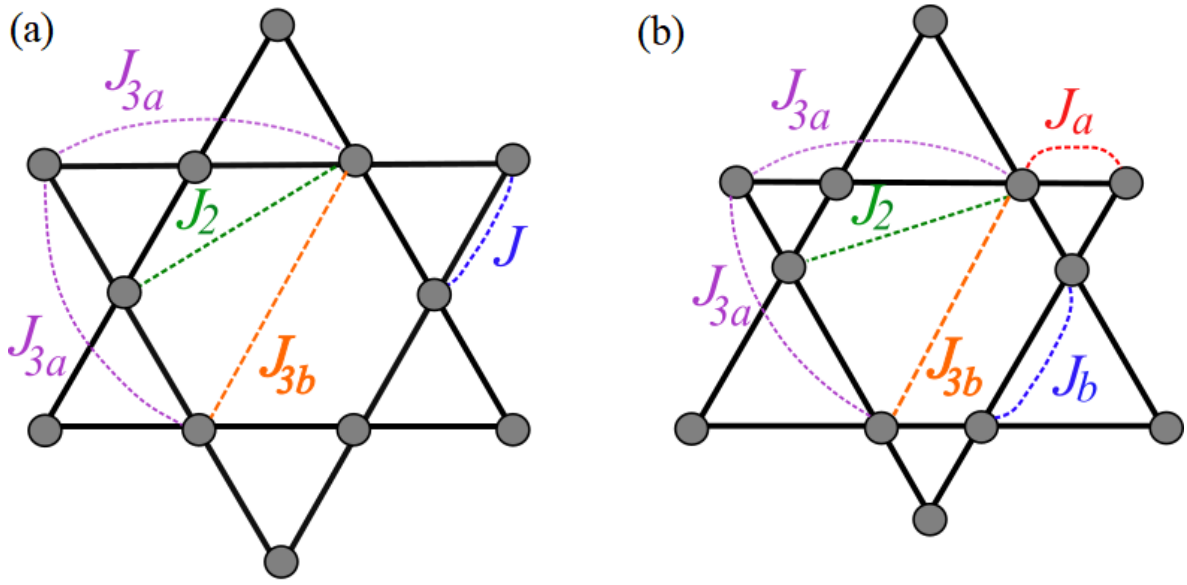

Figure A.4: Figures show further-neighbour couplings in (a) pyrochlore lattice, (b) breathing pyrochlore lattice. Panels show perspective of the lattices, perpendicular to the ⟨111⟩ direction wherein the pryochlore lattice is seen as alternating layers of kagomé and triangular lattices.

A.4 Further-Neighbour Interactions and Adjacency Matrices

Here, we describe the adjacency matrices used in this thesis to work with a breathing or non-breathing pyrochlore lattice and further-neighbour interactions. We have utilized at-most three further-neighbour interactions in this thesis, given by second nearest neighbour interaction J_2 and two inequivalent third neighbour interactions J_{3a} and J_{3b} (see Fig. A.4). The adjacency matrix in real space is given by elements 1 if the sites are connected or 0 if the sites are not connected. The Fourier transform convention used is given by:

$$J^{ab}(\mathbf{q}) = \sum_{i,j} J_{ij}^{ab} e^{i\mathbf{q}\cdot(\mathbf{R}_i^a - \mathbf{R}_j^b)}. \tag{A.7}$$

Here $\mathbf{R}_i^a$ is the location of a site with indices a, b representing sublattice labels and i, j labelling the Bravais lattice sites. $\mathbf{q}$ is a wavevector in reciprocal space. The nearest neighbour adjacency is given by:

$$J_{\mathrm{NN}}(\mathbf{q}) = \begin{pmatrix} 0 & 2\cos\left(\frac{q_x+q_y}{4}\right) & 2\cos\left(\frac{q_x+q_z}{4}\right) & 2\cos\left(\frac{q_y+q_z}{4}\right) \\ 2\cos\left(\frac{q_x+q_y}{4}\right) & 0 & 2\cos\left(\frac{q_y-q_z}{4}\right) & 2\cos\left(\frac{q_x-q_z}{4}\right) \\ 2\cos\left(\frac{q_x+q_z}{4}\right) & 2\cos\left(\frac{q_y-q_z}{4}\right) & 0 & 2\cos\left(\frac{q_x-q_y}{4}\right) \\ 2\cos\left(\frac{q_y+q_z}{4}\right) & 2\cos\left(\frac{q_x-q_z}{4}\right) & 2\cos\left(\frac{q_x-q_y}{4}\right) & 0 \end{pmatrix}.$$

For the case of the breathing pyrochlore, J_{NN}[1] breaks up into two parts, one for J_a and

[1]If the lattice is not breathing then this matrix is referred to simply as $A(\mathbf{q})$. If the lattice is a breathing pyrochlore, the two inequivalent nearest-neighbour adjacency matrices is reffered to as $A(\mathbf{q})$ and $B(\mathbf{q})$. For a non-breathing pyrochlore lattice with $J_a = J_b$, $J_{\mathrm{NN}}(\mathbf{q}) = A(\mathbf{q}) + B(\mathbf{q})$.

another for J_b. The bond length ratio is given by γ. The adjacency matrices are then given by:

$$A(\mathbf{q}) = \begin{pmatrix} 0 & e^{-\frac{1}{4}i(x+y)} & e^{-\frac{1}{4}i(x+z)} & e^{-\frac{1}{4}i(y+z)} \\ e^{\frac{1}{4}i(x+y)} & 0 & e^{\frac{1}{4}i(y-z)} & e^{\frac{1}{4}i(x-z)} \\ e^{\frac{1}{4}i(x+z)} & e^{-\frac{1}{4}i(y-z)} & 0 & e^{\frac{1}{4}i(x-y)} \\ e^{\frac{1}{4}i(y+z)} & e^{-\frac{1}{4}i(x-z)} & e^{-\frac{1}{4}i(x-y)} & 0 \end{pmatrix}. \tag{A.8}$$

Here and in further equations x, y, z refer to q_x, q_y, and q_z (to conserve space). The adjacency matrix for J_b corresponding to the 'larger' tetrahedra is given by (only differernce being extra factor of γ in the exponent):

$$B(\mathbf{q}) = \begin{pmatrix} 0 & e^{\frac{1}{4}i\gamma(x+y)} & e^{\frac{1}{4}i\gamma(x+z)} & e^{\frac{1}{4}i\gamma(y+z)} \\ e^{-\frac{1}{4}i\gamma(x+y)} & 0 & e^{-\frac{1}{4}i\gamma(y-z)} & e^{-\frac{1}{4}i\gamma(x-z)} \\ e^{-\frac{1}{4}i\gamma(x+z)} & e^{\frac{1}{4}i\gamma(y-z)} & 0 & e^{-\frac{1}{4}i\gamma(x-y)} \\ e^{-\frac{1}{4}i\gamma(y+z)} & e^{\frac{1}{4}i\gamma(x-z)} & e^{\frac{1}{4}i\gamma(x-y)} & 0 \end{pmatrix}. \tag{A.9}$$

The second nearest-neighbour interaction, J_2, connects sites of different sublattices and hops over two bonds $\nparallel$ to each other (see Fig. A.4). The Fourier transformed adjacency matrices for J_2 is given by:

$$C(\mathbf{q}) = \begin{pmatrix} 0 & 4\cos\left(\frac{z}{2}\right)\cos\left(\frac{x-y}{4}\right) & 4\cos\left(\frac{y}{2}\right)\cos\left(\frac{x-z}{4}\right) & 4\cos\left(\frac{x}{2}\right)\cos\left(\frac{y-z}{4}\right) \\ 4\cos\left(\frac{z}{2}\right)\cos\left(\frac{x-y}{4}\right) & 0 & 4\cos\left(\frac{x}{2}\right)\cos\left(\frac{y+z}{4}\right) & 4\cos\left(\frac{y}{2}\right)\cos\left(\frac{x+z}{4}\right) \\ 4\cos\left(\frac{y}{2}\right)\cos\left(\frac{x-z}{4}\right) & 4\cos\left(\frac{x}{2}\right)\cos\left(\frac{y+z}{4}\right) & 0 & 4\cos\left(\frac{z}{2}\right)\cos\left(\frac{x+y}{4}\right) \\ 4\cos\left(\frac{x}{2}\right)\cos\left(\frac{y-z}{4}\right) & 4\cos\left(\frac{y}{2}\right)\cos\left(\frac{x+z}{4}\right) & 4\cos\left(\frac{z}{2}\right)\cos\left(\frac{x+y}{4}\right) & 0 \end{pmatrix}.$$

There are two inequivalent third farthest neighbour interactions J_{3a} and J_{3b} which connect the same sublattices. J_{3a} connects sites reached by hopping over two bonds parallel to each other and J_{3b} connects sites at opposite ends of the hexagon in the kagomé layer (see Fig. A.4). The Fourier transformed Adjacency matrices are diagonal since only the same sublattices are connected. They are given by:

$$\begin{aligned} D(\mathbf{q}) = diag[&2\left(C\left(\frac{x+y}{2}\right)+C\left(\frac{x+z}{2}\right)+C\left(\frac{y+z}{2}\right)\right), \\ &2\left(C\left(\frac{x+y}{2}\right)+C\left(\frac{x-z}{2}\right)+C\left(\frac{y-z}{2}\right)\right), \\ &2\left(C\left(\frac{x-y}{2}\right)+C\left(\frac{x+z}{2}\right)+C\left(\frac{y-z}{2}\right)\right), \\ &2\left(C\left(\frac{x-y}{2}\right)+C\left(\frac{x-z}{2}\right)+C\left(\frac{y+z}{2}\right)\right)]. \end{aligned}$$

These are just diagonal entries of the matrix, the rest of the elements are 0. C here refers to a cosine function. J_{3b} is also a diagonal matrix given by:

$$\begin{aligned} E(\mathbf{q}) = diag[&2\left(C\left(\frac{x-y}{2}\right)+C\left(\frac{x-z}{2}\right)+C\left(\frac{y-z}{2}\right)\right), \\ &2\left(C\left(\frac{x-y}{2}\right)+C\left(\frac{x+z}{2}\right)+C\left(\frac{y+z}{2}\right)\right), \\ &2\left(C\left(\frac{x+y}{2}\right)+C\left(\frac{x-z}{2}\right)+C\left(\frac{y+z}{2}\right)\right), \\ &2\left(C\left(\frac{x+y}{2}\right)+C\left(\frac{x+z}{2}\right)+C\left(\frac{y-z}{2}\right)\right)]. \end{aligned}$$

These are the usual adjacency matrices found in the literature [11, 42, 43] for the Pyrochlore lattice.

Appendix B

Minimization Implementation Discussions

In Chap. 4, we utilized the standard algorithms in Scipy's optimization modules (Ref. [87]) and a brute force global minimization routine. The global minimization found the approximate minima of the adjacency matrix ($J(\mathbf{q})$) and used these as initial guess points for the optimization algorithms. The optimization algorithms are easily implemented and we refer the reader to the documentation (Ref. [87] and Ref. [50]). Some key observations are briefed below.

The Nelder-Mead method also known as the downhill simplex method constructs a simplex in the parameter space centred at the guess points and moves the simplex according to certain rules. These are given in Refs. [88, 89]. This method may stagnate at local minima and a proper guess point has to be provided for efficient use. For dimen-

sions greater than 2, adaptive parameters have to be utilized which modify the way that the simplex moves. Adaptive parameters may be used in Scipy by using an extra command: options=‘adaptive’: True. Further details on adaptive parameters may be found in Ref. [90].

The Modified Powell algorithm (MP) takes a guess point and draws 3 arbitary axes. The algorithm searches along these lines for a minimum and on finding it, displaces the axes to this point. It then reorients the axes and repeats the above process till the global minimum is found. We found that the minima found using MP are not as precise as the Nelder Mead method but the stagnation at local extrema is much rarer. This method may develop problems on flat surfaces with peaks or valleys. In general, this method is useful to find approximate guess points after which the Nelder Mead method may find more precise minima. Further details may be obtained from Ref. [91]. The rest of the methods are used only sparingly for cases where the above algorithms do not work. They are enumerated as:

- Truncated Newton Algorithm (TN) [92],
- Conjugate Gradient (CG) method in pp. 120 - 122 of Ref. [92],
- BFGS (Broyden, Fletcher, Goldfarb and Shanno Algorithm) pp. 136 in Ref. [92],
- Limited memory- L-BFGS [93],
- COBYLA (Constrained Optimization by Linear Approximation method) [94].

These are derivative based (except COBYLA) methods and in general, do not perform as well as the Nelder Mead or the Modified Powell algorithms. They fail at points of inflection

and commonly stagnate at local minima (except the COBYLA algorithm which was noted to perform surprisingly well, compared to the other algorithms).